

Localizing genuine multipartite entanglement in noisy stabilizer statesHarikrishnan K. J.  and Amit Kumar Pal *Department of Physics, Indian Institute of Technology Palakkad, Palakkad 678 623, India*

(Received 12 January 2023; accepted 26 July 2023; published 5 September 2023)

Characterizing large noisy multipartite quantum states using genuine multipartite entanglement is a challenging task. In this paper, we calculate lower bounds of genuine multipartite entanglement localized over a chosen multipartite subsystem of multiqubit stabilizer states in the noiseless and noisy scenarios. In the absence of noise, adopting a graph-based technique, we perform the calculation for arbitrary graph states as representatives of the stabilizer states and show that the graph operations required for the calculation have a polynomial scaling with the system size. As demonstrations, we compute the localized genuine multipartite entanglement over subsystems of large graphs having linear, ladder, and square structures. We also extend the calculation for graph states subjected to single-qubit Markovian or non-Markovian Pauli noise on all qubits and demonstrate, for a specific lower bound of the localizable genuine multipartite entanglement corresponding to a specific Pauli measurement setup, the existence of a critical noise strength beyond which all of the postmeasured states are biseparable. The calculation is also useful for arbitrary large stabilizer states under noise due to the local unitary connection between stabilizer states and graph states. We demonstrate this by considering a toric code defined on a square lattice and computing a lower bound of localizable genuine multipartite entanglement over a nontrivial loop of the code. Similar to the graph states, we show the existence of the critical noise strength in this case also and discuss its interesting features.

DOI: [10.1103/PhysRevA.108.032404](https://doi.org/10.1103/PhysRevA.108.032404)**I. INTRODUCTION**

In the last three decades, characterizing multipartite quantum states using multipartite entanglement [1,2] as figure of merit has been established as one of the most important and yet challenging problems. These quantum states are used as resources in quantum information processing tasks, such as measurement-based quantum computation [3–5], quantum cryptography [6–10], and quantum dense coding [11–13] involving multiple senders and receivers [14–17]. Additionally, multipartite entanglement has also been proved a crucial ingredient in problems related to quantum many-body systems [18,19], photosynthetic complexes [20–22], and even anti-de Sitter/conformal field theory (AdS/CFT) correspondence in quantum gravity [23–28]. These observations have driven the world-wide effort to create multipartite-entangled quantum states in laboratory using trapped ions [29,30], cold atoms and optical lattices [31–34], photons [35–38], nuclear magnetic resonance [39], and superconducting qubits [40].

Among the multipartite quantum states of interest, stabilizer states [41,42] form an extremely important class of states containing genuinely multipartite entanglement (GME) [1], i.e., these states are not separable in any bipartition. Stabilizer states are used widely in several areas of quantum information theory. Arguably, the most prominent examples of these states are the graph states [43], encompassing (1) the multiqubit GHZ states [44] having immense applications in quantum communication [45,46] and quantum metrology [47], and (2) the cluster states [48] used as resource in one-way quantum computation and in building quantum networks [49]. Stabilizer states are also used in fault-tolerant quantum error corrections [50,51] and in establishing secure quantum

communication [52,53]. Experimental realization and manipulation of stabilizer states have also been possible [54–60], thereby highlighting the potential for testing theoretical results in the laboratory.

Stabilizer states with a large number of qubits are required to perform quantum error correction where error occurs on multiple physical qubits. Therefore, it is natural to look for methodologies to characterize large stabilizer states as well as its subsystems under different types of noise using GME. In this respect, graph states have received a great deal of the attention due to the fact that all stabilizer states can be connected to graph states via local unitary transformations [61], leading to translation of the results on GME obtained for the graph states [43,48] to the case of arbitrary stabilizer states. However, while a few studies exist on characterizing noisy graph states using bipartite [62,63] and genuine multipartite entanglement [64–66], in general, calculation for mixed states in the presence of noise becomes difficult due to the scarcity of computable GME measures for mixed states [1]. Therefore, a full understanding of the behavior of GME in noisy stabilizer states and its different multipartite subsystems is far from complete. This brings us to the investigation of the GME over chosen subsystems of a multiqubit system described by a stabilizer state with and without noise, which is the focus of this paper.

Towards this, we adopt a measurement-based protocol [67–69] for quantifying entanglement in subsystems of stabilizer states, which has been established as an appropriate approach [43,70,71] over the partial-trace-based methods [1]. This leads to *localizable entanglement* (LE)—the maximum average entanglement over the chosen subsystem, maximized over all possible single-qubit projection measurements over

all qubits in the rest of the system [68,69]—defined in the same vein as the *entanglement of assistance* [67]. Apart from being crucial in quantifying two-qubit entanglement in pure [43] as well as noisy stabilizer states [70,71], LE and related ideas have also been proven a key element in studying the entanglement length [68,69,72,73] and quantum phase transitions [74–77] in quantum spin models, and in defining entanglement percolation [78] in quantum networks. Extensive investigations into the features of LE in generic multiqubit quantum states in the presence of noise have also been performed [79–82].

The studies on the role of LE in characterizing noiseless and noisy quantum states have mostly considered a bipartite split of the chosen subsystem, often a two-qubit subsystem [43,68–78]. The exponential growth of the Hilbert space with the number of qubits has also confined these studies to systems of small number of qubits. While exploration of the behavior of the localizable GME (LGME) on multiparty subsystems of paradigmatic pure states has been attempted [83], LGME on subsystems of noisy multipartite quantum states of arbitrary size, to the best of our knowledge, remains unexplored.

In this paper we focus specifically on arbitrary stabilizer states [41,42] in noiseless scenarios as well as under noise corresponding to specific noise models and compute LGME along with its lower bounds to investigate its features. Selecting *graph states* [43] as a candidate stabilizer state, we calculate the LGME and its lower bounds over a selected subsystem using a graphical approach for single-qubit measurements [84,85] and demonstrate the results in typical graphs having linear, ladder, and square graph structures. We also extend the calculation in situations where the graph states (or the stabilizer states) are subjected to single-qubit local Pauli noises [41,86] of Markovian [87] and non-Markovian [88–90] variants and investigate at which noise strength the localized *genuine* multipartite entanglement ceases to exist. The calculations can also be extended for arbitrary stabilizer states due to their connection to graph states by local unitary operations [61,91]. We demonstrate this by considering a toric code [92,93] defined on a square lattice. A more detailed yet nontechnical overview of the main results, discussed in Secs. III–V, can be found in Sec. II. Section VI contains the concluding remarks and an overview of possible future directions.

II. OVERVIEW OF THE MAIN RESULTS

In this section we present an overview of the subsequent sections containing the technical details and different results. In Sec. III we consider the noiseless scenario and provide a description of the graph states and their important features in Sec. III A. The formal definition of LE is given in Sec. III B, and the LGME on a chosen subsystem corresponding to single-qubit Pauli measurements on arbitrary graph states is discussed. Since the measurements are restricted to single-qubit Pauli measurements on all qubits outside the chosen subsystem, our calculation provides a lower bound of the LGME. Specifically, we show that

(a) For a fixed Pauli measurement setup, the resulting graphs corresponding to the postmeasured states are independent of the measurement outcomes and

(b) The postmeasured graph states differ from each other only by local unitary operations, thereby having identical entanglement properties.

These results lead to the lower bound of the LGME on an arbitrary subsystem of a graph to be *the maximum of the GME over the set of connected subgraphs on the chosen subsystem, obtained from the postmeasured graphs once the Pauli measurements are incorporated*. In these calculations, we employ graph operations to implement the Pauli measurements and show that *the graph operations involved in this process has a polynomial scaling with the system size*. By virtue of the local unitary connection between an arbitrary stabilizer state and the graph states, the above results hold for arbitrary stabilizer states also.

We further show that depending on the structure of the graph, the set of all possible single-qubit Pauli measurement can be divided into two classes: (1) one, where all measurement outcomes are equally probable, and (2) another, where only a subset of outcomes having equal probability of occurrence are *allowed*, and the rest are *forbidden*. These classifications do not affect the calculation in the case of pure states (see Sec. III B 2). However, in situations where the qubits in the system are subjected to Pauli noise of Markovian and non-Markovian types, which we discuss in Sec. IV,

(a) The postmeasured states corresponding to only the first category of Pauli measurement setups are equally probable and are local unitarily connected to each other.

(b) On the other hand, if the Pauli measurement setup belongs to the second category, transitions may happen between the allowed and forbidden sets of measurement outcomes, and the postmeasured states are not, in general, connected by local unitary operators, thereby losing the advantages in calculation.

A brief description of the specific noise channels used in this paper can be found in Sec. IV A, while the interesting features of the Pauli measurements on noisy graph states and the subsequent calculation of the lower bound of LGME are discussed in Sec. IV B.

In Sec. IV C we construct specific Pauli measurement setups belonging to the first category for typical graph states, such as the linear graph, ladder graph, and square graph, under Markovian and non-Markovian Pauli noise, and determine a lower bound for LGME. The main results summarized in this section are as follows:

(a) There exists a critical noise strength for all four types of Pauli noise considered in this paper, beyond which all the postmeasured states corresponding to the chosen Pauli measurement setup become biseparable.

(b) From the numerical data, we estimate the dependence of this critical noise strength on the degree of non-Markovianity, quantified by the non-Markovianity parameter

(c) We further infer that the critical noise strength is independent of the system size.

The methodology to compute lower bounds of LGME, as adopted in this paper, holds for arbitrary stabilizer states due to their local unitary connection to the graph states. To

demonstrate this, in Sec. V we consider the toric code defined on a square lattice and compute a lower bound of the LGME on a nontrivial loop representing a logical operator in both noisy and noiseless scenario by constructing an appropriate Pauli measurement setup. We show that

(a) It is always possible to localize GME over a nontrivial loop of the toric code in the absence of noise and

(b) Similar to the noisy graphs, a critical noise strength exists for each type of Pauli noise such that all of the postmeasured states corresponding to the chosen Pauli measurement setup become biseparable beyond it.

In the case of the bit-flip noise, we determine the form of the critical noise strength analytically as a function of the non-Markovianity parameter and prove its system-size independence. In the case of other Pauli noise, our data suggest a decrease in the value of the critical noise strength with increasing system size and increasing non-Markovianity parameter. We also construct an appropriate Pauli measurement setup that can provide a lower bound of localizable bipartite entanglement between two nontrivial loops of the toric code.

III. LGME IN GRAPH STATES

In this section we discuss salient features of graph states and present the definition of LE. We also calculate LE and one of its lower bounds corresponding to localization maximized for Pauli measurements.

A. Graph states

A graph [94,95] $G(V, L)$ is a collection of N nodes $V \equiv \{1, 2, \dots, N\}$, and a set of links $L \equiv \{(i, j)\}, i \neq j, i, j \in V$. We are interested in graphs that are *simple*, i.e., have only one edge between two nodes, *connected*, i.e., each node is connected to at least another node in the graph, and *undirected*, i.e., both nodes corresponding to a link are equivalent. Assuming that a qubit is situated on every node of such a graph G , a graph state $|G\rangle$ is defined with respect to G as [43]

$$|G\rangle = \left[\otimes_{(i,j) \in G} C_{(i,j)}^Z \right] |+\rangle^{\otimes N}. \quad (1)$$

Here $|+\rangle = (|0\rangle + |1\rangle)/\sqrt{2}$ is the eigenstate of σ^1 corresponding to the eigenvalue +1, and

$$C_{(i,j)}^Z = \frac{1}{2} [(\sigma_i^0 + \sigma_i^3)\sigma_j^0 + (\sigma_i^0 - \sigma_i^3)\sigma_j^3], \quad (2)$$

with σ^α , $\alpha = 0, 1, 2, 3$, being the 2×2 identity matrix and the x, y , and z components of the Pauli matrices, respectively. Graph states can also be considered as multiqubit stabilizer states [41,43,50] defined by a set of stabilizer generators $\{g_i\} \subset \mathcal{P}^N$ with

$$g_i = \sigma_i^1 \otimes_{j \in \mathcal{N}_i} \sigma_j^3, \quad (3)$$

where \mathcal{P}^N is the N -qubit Pauli group, and \mathcal{N}_i is the neighborhood of the node i constituted of nodes having a direct link with the node i . Here $\text{supp}(g_i) = i \cup \mathcal{N}_i$, called the *support* of g_i , are the qubits on which g_i acts nontrivially, i.e., $\sigma_j \neq I_j \forall j \in i \cup \mathcal{N}_i$, with σ_j being the contribution in g_i corresponding to the node j . The generators are mutually commuting and therefore share a common eigenspace,

given by

$$|G_\alpha\rangle = Z_\alpha |G\rangle = \otimes_{i \in V} (\sigma_i^3)^{\alpha_i} |G\rangle, \quad (4)$$

where $\alpha_i = 0, 1 \forall i \in V$, $Z_\alpha = \otimes_{i \in V} (\sigma_i^3)^{\alpha_i}$, and $\alpha \equiv \alpha_1 \alpha_2 \dots \alpha_N$ is a multi-index. Note that $|G\rangle$ is given $|G_0\rangle$, corresponding to $\alpha_i = 0 \forall i \in V$, which is the eigenstate having eigenvalue +1 for all g_i :

$$g_i |G\rangle = (+1) |G\rangle \quad \forall i \in V. \quad (5)$$

The states $\{|G_\alpha\rangle; \alpha = 0, 1, 2, \dots, 2^N - 1\}$ form a complete basis of the Hilbert space of the N -qubit system and any state, ρ , of the system that is diagonal in this basis, having the form

$$\rho = \sum_{\alpha=0}^{2^N-1} p_\alpha |G_\alpha\rangle \langle G_\alpha|, \quad (6)$$

is called the graph-diagonal (GD) state for an arbitrary probability distribution $\{p_\alpha\}$, with $\sum_\alpha p_\alpha = 1$.

B. Localizable entanglement in graph states

Let us now assume that the subsystem S contains n ($2 \leq n \leq N - 1$) qubits labeled by $1, 2, \dots, n$, while the rest of the qubits $\{n + 1, n + 2, \dots, N\}$ constitute the rest of the system S' . Let us also assume that the state of the system is ρ . Localizable entanglement [68,69,72] over the subsystem S is the maximum average entanglement that can be localized over S by performing single-qubit projection measurements on all the qubits in S' . Here the maximization is performed over the complete set of single-qubit projection measurements. We denote the LE by E_S , given by

$$E_S = \max_{\{M_k\}} \sum_k p_k E(\varrho_S^k), \quad (7)$$

where E is a chosen bipartite or multipartite entanglement measure [1,2] computed over the unmeasured qubits after measurement. The set $\{M_k\}$ is the complete set of single-qubit projection measurements M_k on qubits in S' , p_k is the probability of obtaining the measurement outcome k , given by

$$p_k = \text{Tr}[(I \otimes M_k) \rho (I \otimes M_k)^\dagger], \quad (8)$$

ϱ_S^k denotes the postmeasured state on S corresponding to the measurement outcome k , given by

$$\varrho_S^k = \text{Tr}_{S'}[\varrho_k] \quad (9)$$

with

$$\varrho_k = \frac{1}{p_k} [(I \otimes M_k) \rho (I \otimes M_k)^\dagger], \quad (10)$$

and I is the identity operator on the Hilbert space of S . For brevity, we write

$$\varrho_k = \frac{1}{p_k} [M_k \rho M_k^\dagger]. \quad (11)$$

We consider rank-1 single qubit projective measurements on the qubits in S' , such that the measurement operator M_k takes the form

$$M_k = \otimes_{i \in S'} P_{k_i}, \quad (12)$$

where $P_{k_i} = |k_i\rangle\langle k_i|$ are projectors corresponding to $|k_i\rangle \in \{|0_i\rangle, |1_i\rangle\}$, with

$$\begin{aligned} |0_i\rangle &= \cos \frac{\theta_i}{2} |0_i\rangle + e^{i\phi_i} \sin \frac{\theta_i}{2} |1_i\rangle, \\ |1_i\rangle &= \sin \frac{\theta_i}{2} |0_i\rangle - e^{i\phi_i} \cos \frac{\theta_i}{2} |1_i\rangle, \end{aligned} \quad (13)$$

$\{|0_i\rangle, |1_i\rangle\}$ being the computational basis in the Hilbert space of qubit i . The measurement outcome index k can be identified as a multi-index $k \equiv k_{n+1}k_{n+2} \dots k_N$. Therefore, the optimization involved in Eq. (7) reduces to a $2(N-n)$ -parameter optimization problem over real parameters (θ_i, ϕ_i) , $i \in S'$, with $0 \leq \theta_i \leq \pi$, $0 \leq \phi_i \leq 2\pi$.

Note that for systems with large N , computation of E_S can, in general, be computationally demanding. In this paper we focus on the LE over a subsystem S of a graph state $|G\rangle$ via only single-qubit Pauli measurements. A Pauli measurement setup (PMS) in S' is defined by a configuration $\sigma_{n+1}^{\alpha_{n+1}} \sigma_{n+2}^{\alpha_{n+2}} \dots \sigma_N^{\alpha_N}$ of single-qubit Pauli measurements on the qubits in S' , which is denoted by the label $\alpha \equiv \alpha_{n+1} \alpha_{n+2} \dots \alpha_N$. There can be a total of 3^{N-n} such setups, since $\alpha_i = 1, 2, 3$, $i = n+1, n+2, \dots, N$.¹ Let us denote the maximum LE obtained from all possible PMSs (i.e., all possible α) by $E_S^{\mathcal{P}}$, where [70,71,80,81]

$$E_S^{\mathcal{P}} = \max_{\alpha} \sum_{k_{\alpha}=0}^{2^{N-n-1}} p_{k_{\alpha}} E(\varrho_S^{k_{\alpha}}), \quad (14)$$

k_{α} being the label for the measurement outcomes corresponding to the PMS α . We further discard the subscript α from the measurement outcome k to keep the text uncluttered. Due to the restriction on the set of measurements, $E_S^{\mathcal{P}}$ is referred to as the restricted LE (RLE) [70,71,80,81], and the corresponding LGME the *restricted* LGME (RLGME). Note that by definition of LE,

$$0 \leq E_S^{\mathcal{P}} \leq E_S. \quad (15)$$

While it is known that the Pauli measurements optimize E_S localized for subsystems S constituted of only two qubits [43,96], to the best of our knowledge, a similar result for subsystems constituted of multiple qubits is yet to be proved. In our numerical investigation, for an arbitrary graph state (also for an arbitrary stabilizer state; see Sec. V) in the noiseless scenario (i.e., for pure states), we always find $E_S = E_S^{\mathcal{P}}$. Motivated by this, in the following, we discuss the computation of $E_S^{\mathcal{P}}$ in arbitrary graph states.

1. Localization via Pauli measurements

To analytically compute $E_S^{\mathcal{P}}$ for an arbitrary graph state $\rho = |G\rangle\langle G|$ corresponding to a graph G , for ease of calculation, let us first reindex the qubits in S' as $j = i - n$, where $j = 1, 2, 3, \dots, N - n$. We denote the projectors $P_{k_j}^{\alpha_j}$ corresponding to a Pauli measurement on the qubit $j \in S'$ as

$$P_{k_j}^{\alpha_j} = \frac{1}{2} [\sigma_j^0 + (-1)^{k_j} \sigma_j^{\alpha_j}], \quad (16)$$

with $k_j = \pm 1$ being the measurement outcomes, and $|k_j\rangle$ is the eigenstate of $\sigma_j^{\alpha_j}$ corresponding to the eigenvalue k_j . Note that a single-qubit $\sigma_j^{\alpha_j}$ ($\alpha_j = 1, 2$) measurement on a given graph state $|G\rangle$ is equivalent to a σ_j^3 measurement on the graph state $U_j^{\alpha_j \dagger} \rho_G U_j^{\alpha_j}$, where $U_j^{\alpha_j}$ is a Clifford unitary operator from the set $\{\sigma_j^3, H_j, R_j\}$, H_j being the Hadamard operator, and $R_j = \sqrt{\sigma_j^3}$. Explicitly,

$$U_j^1 = H_j, \quad U_j^2 = R_j H_j, \quad (17)$$

such that

$$\begin{aligned} \sigma_j^1 &= H_j \sigma_j^3 H_j, \\ \sigma_j^2 &= R_j H_j \sigma_j^3 H_j R_j^{\dagger}. \end{aligned} \quad (18)$$

Therefore, for a specific PMS α , the measurement operator on S' having the form

$$M_k^{\alpha} = \otimes_{j \in S'} P_{k_j}^{\alpha_j} \quad (19)$$

would result in an overall Clifford unitary operator of the form

$$\mathbf{U}_{\alpha} = \otimes_{j \in S'} U_j^{\alpha_j}, \quad \alpha_j = 1, 2, \quad (20)$$

on the subsystem S' (see Fig. 1), such that $\mathbf{U}_{\alpha}^{\dagger} M_k^{\alpha} \mathbf{U}_{\alpha} \rightarrow M_k^{\alpha}$ with $\alpha_j = 3 \forall j \in S'$ after the transformation. Note that \mathbf{U}_{α} is specific to the chosen PMS α . This further implies [from Eq. (11)]

$$\varrho_k = \mathbf{U}_{\alpha} M_k^{\alpha} \rho_{\alpha} M_k^{\alpha \dagger} \mathbf{U}_{\alpha}^{\dagger} \quad (21)$$

with

$$\rho_{\alpha} = \mathbf{U}_{\alpha}^{\dagger} \rho \mathbf{U}_{\alpha} \quad (22)$$

being specific to the original choice of α . Figure 1(a) depicts an eight-qubit graph state for demonstration, four of which are measured in Pauli basis, and the corresponding $U_i^{\alpha_i}$ for transforming all Pauli measurements to σ^3 measurements are shown in Fig. 1(b).

To further simplify, note that the state $\mathbf{U}_{\alpha}|G\rangle$ can be written as [84,85]

$$\mathbf{U}_{\alpha}^{\dagger}|G\rangle = e^{\pm i\phi} \mathbf{V}_{\alpha}|G'_{\alpha}\rangle, \quad (23)$$

where $e^{\pm i\phi}$ is an irrelevant global phase, and G'_{α} is a *reduced graph* with modified connectivity that depends explicitly on α and is defined on the nodes of the graph G . Here

$$\mathbf{V}_{\alpha} = \otimes_{i \in G'_{\alpha}} V_i \quad (24)$$

is a unitary operator such that V_i are local Clifford unitaries, and

$$V_j^{\dagger} P_{k_j}^3 V_j = P_{k_j}^3 \forall j \in S'_1, \quad (25)$$

where $k_j = \pm 1$ and S'_1 are the collection of qubits that construct the neighborhood of the qubits belonging to S . We denote the set of the rest of the qubits in S' by S'_2 , where $S' = S'_1 \cup S'_2$ and $S'_1 \cap S'_2 = \emptyset$. The transformation

$$\rho_{\alpha} \rightarrow \rho'_{\alpha} = \mathbf{V}_{\alpha}|G'_{\alpha}\rangle\langle G'_{\alpha}| \mathbf{V}_{\alpha}^{\dagger}, \quad (26)$$

corresponding to Eq. (23), can be performed via a series of local transformations on the underlying graph G using a graphical representation of the states ρ_{α} and ρ'_{α} [84,85], from

¹Note here that we discard $\alpha_i = 0$ in order to ensure measurement on all qubits in S' .

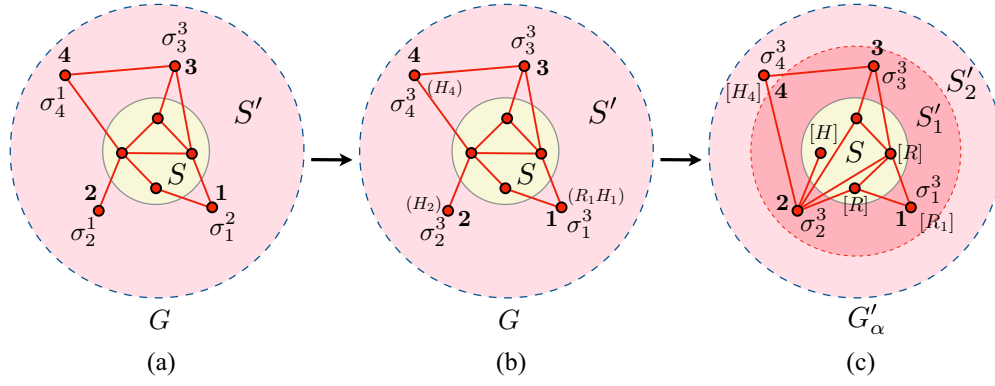


FIG. 1. (a) Subsystems S and S' of an arbitrary graph G . The nodes in S' are labeled as $j = 1, 2, 3, 4$ (see Sec. III B 1), and a Pauli measurement setup $\sigma_1^2 \sigma_2^1 \sigma_3^3 \sigma_4^1$, denoted by $\alpha \equiv \alpha_1 \alpha_2 \alpha_3 \alpha_4 = 2131$ is assumed for demonstration. (b) The Pauli measurement setup $\sigma_1^2 \sigma_2^1 \sigma_3^4 \sigma_4^1$ ($\alpha = 2131$) can be transformed to $\sigma_1^3 \sigma_2^3 \sigma_3^3 \sigma_4^3$ corresponding to $\alpha = \beta = 3333$ via the application of the unitary operators U_1^2, U_2^1 , and U_4^1 (definitions given in Eq. (17)), which are denoted within parentheses. The connectivity of the graph remains unchanged. (c) The graph state ρ_α [depicted in (b)] can be transformed to ρ'_α [see Eq. (23)], where G'_α is a graph on the same nodes with different connectivity, as shown in (c). The unitary operators V_j , defined through the Eqs. (24) and (25), are shown within square brackets. The subsystem S'_1 is constituted of the nodes that belong to the (combined) neighborhood of all the nodes in S , while S'_2 is the set of the rest of the nodes in S' ($S'_1 \cup S'_2 = S'$, and $S'_1 \cap S'_2 = \emptyset$). Note that the unitary operators V_j for $j \in S'_1$ are either identity, or R_j , which keeps σ_j^3 invariant. However, for qubit $j = 4$ in S'_2 , $V_4 = H_4$, which results in $H_4 \sigma_4^3 H_4^\dagger = \sigma_4^1$. Therefore, after the reduction of the graph according to Eq. (23), the measurement setup in S'_2 is not necessarily all σ^3 .

which the graph G'_α can also be extracted. This transformation is a rather technical one that involves (1) redefining the attributes of the nodes of the graphs according to the single-qubit unitary operators U_j^\dagger and V_j applied to them and (2) transforming the underlying graph along with the local unitary operators using a specific set of local graph operations. It ensures that

P1. V_j corresponding to $j \in S'_2$ are from the set $\{I_j, \sigma_j^3, H_j, H_j \sigma_j^3, R_j, R_j \sigma_j^3\}$

P2. V_i corresponding to a node i that either is (a) in the neighborhood of a node $j \in S'_2$ with $V_j \in \{H_j, H_j \sigma_j^3\}$ or (b) in S'_1 , are from the set $\{I_i, \sigma_i^3, R_i, R_i \sigma_i^3\}$ and

P3. Any two nodes j and $j' \in S'_2$ having $V_j = H_j$ or $V_{j'} = H_{j'} \sigma_{j'}^3$ do not have a link connecting them,

thereby satisfying Eq. (25). For interested readers, details on this graph transformation can be found in Appendix A, while readers not interested in technical details can continue with this section. The transformation $\rho_\alpha \rightarrow \rho'_\alpha$, according to Eq. (23), is depicted in Fig. 1(c), along with the sets S'_1 and S'_2 , and the unitary operators V_i . The same transformation has also been depicted using the graph transformation notation in Fig. 21 in Appendix A. The overall protocol for obtaining the reduced graph G'_α scales polynomially with the number of measured nodes, as discussed in Appendix A 2.

Given a successful reduction of the graph $G \rightarrow G'_\alpha$ for a specific PMS α , the subgraph G'_α on the chosen subsystem S in G'_α can be obtained by deleting all links between the nodes in S and all other nodes in S' . Using the above protocol, the following proposition can be proved for $E(\rho_S^k)$ and the state $|\rho_S^\alpha\rangle$ (see Appendix B for the proof).

Proposition 1. For a given Pauli measurement setup on a subsystem S' of an arbitrary graph state, the average entanglement postmeasurement on the subsystem S , where $S \cup S'$ constitutes the entire system, is (a) independent of the measurement outcomes, (b) depends only on the chosen Pauli

measurement setup, and (c) is given by

$$E(\rho_S^k) = E(|G'_\alpha\rangle\langle G'_\alpha|), \quad (27)$$

where E is the chosen entanglement measure. ■

Consequently, using the definition of $E_S^{\mathcal{P}}$ (see Eq. (14)), the following corollary can also be written.

Corollary 1.1. The value of $E_S^{\mathcal{P}}$ on the subsystem S can be determined by performing an optimization over all the reduced graphs obtained from all possible Pauli measurement setups on S' and is given by

$$E_S^{\mathcal{P}} = \max_\alpha [E(|G'_\alpha\rangle\langle G'_\alpha|)]. \quad (28)$$

■

2. Allowed and forbidden sets of outcomes

A discussion on the different measurement outcomes k corresponding to the measurement operators M_k^α is in order here. By design of the graph transformation (see Appendix A) ensuring P1–P3, σ_i^3 measurements over the set of nodes \mathcal{Z} that form the combined neighborhood of the nodes in S'_2 with $V_j = H_j, H_j \sigma_j^3$ and the nodes in S'_1 remain unchanged due to the unitary transformations V_α .² Therefore, following Sec. III B 1, for a specific α , we write the transformed M_k^α as M_{lm}^α , where we now relabel the measurement outcomes corresponding to $j \in \mathcal{Z}$ as l , and the same corresponding to nodes outside \mathcal{Z} as m . Note that now the index m corresponds to the nodes $j \in S'_2$, for which $V_j = H_j, H_j \sigma_j^3$, i.e., for which a projection in the basis of σ_j^1 has to be applied as part of M_{lm}^α . The projections on the nodes in \mathcal{Z} leave each of these node completely decoupled from the rest of the graph (since $\alpha_j = 3 \forall j \in \mathcal{Z}$), and apply either I or σ^3 unitaries on

²Clearly, $L \leq |\mathcal{Z}| \leq N - n$, $|\mathcal{Z}|$ being the size of \mathcal{Z} , and L being the size of S'_1 .

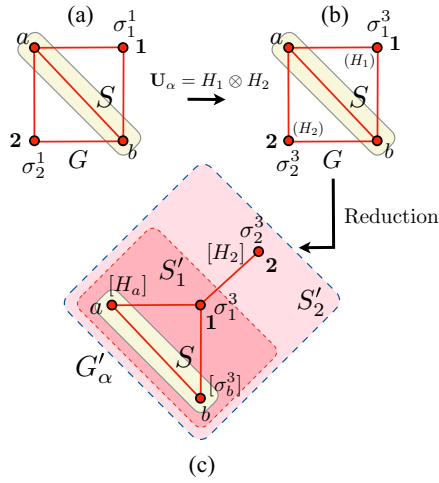


FIG. 2. (a) A four-qubit graph state constituted of the qubits a , b , 1, and 2, where $\{1, 2\}$ constitute the measured subsystems A' . (b) A PMS given by $\alpha = 11$ ($\alpha_1 = 1, \alpha_2 = 1$) can be converted to a setup of σ^3 measurements on both qubits 1 and 2 via unitary operation $U_\alpha = H_1 \otimes H_2$, where H_1 and H_2 are shown in parentheses. (c) The state ρ_α can be converted to ρ'_α with the unitary operators $V_\alpha = H_a \otimes \sigma_b^3 \otimes I_3 \otimes H_2$, where these unitary operators are depicted in square brackets on the reduced graph G'_α . On G'_α , qubit 1 (2) constitutes the region S'_1 (S'_2).

the node depending on the outcomes l corresponding to its neighborhood.³ An isolated node j in a graph is in the state $|+_j\rangle$ and is product with the rest of the graph (see Sec. III A). However, depending on the outcome l on its neighborhood, after projecting all nodes in Z , the isolated node $j \in S'_2$ with $V_j = H_j, H_j \sigma_j^3$ either (a) remains in the state $|+_j\rangle$ (if I applies to node j) or (b) changes to the state $|-_j\rangle$ (if σ^3 operator applies on j). Therefore, further projection on such nodes in σ^1 basis may result in $\langle m_j |+_j\rangle = 0$, or $\langle m_j |-_j\rangle = 0$, which leads to a set of outcomes lm , and consequently $lm \equiv k$ being *forbidden*⁴ for a given Pauli measurement setup α .

We demonstrate the occurrence of the forbidden and allowed set of measurement outcomes with an example of a single four-qubit connected graph depicted in Fig. 2(a). The region S is constituted of the qubits a and b , while the measured subsystem $S' \equiv \{1, 2\}$. For demonstration, we choose the PMS given by $\alpha \equiv 11$ ($\alpha_1 = 1, \alpha_2 = 1$). The four possible measurement outcomes corresponding to these measurements would be $k \equiv k_1 k_2 = (+1)(+1), (+1)(-1), (-1)(+1)$, and $(-1)(-1)$. The PMS can be converted to a σ^3 measurement setup on qubits 1 and 2 by the unitary operator $U_\alpha = H_1 \otimes H_2$, which changes the measurement basis ($\alpha_1: 1 \rightarrow 3, \alpha_2: 1 \rightarrow 3$) but not the measurement outcomes [see Fig. 2(b)]. Following the discussion in Sec. III B 1, we now label the outcomes corresponding to qubit 1 (2) as l_1 (m_2). The state ρ_α can now be transformed as ρ'_α with $V_\alpha = H_a \otimes \sigma_b^3 \otimes I_1 \otimes H_2$ and a transformed graph G'_α [see Fig. 2(c)]. Clearly, the σ^3 measurement on qubit 2 is now transformed to a σ^1 measure-

ment, implying $\alpha_2 = 3 \rightarrow \alpha_2 = 1$, while $\alpha_1 = 3$ on qubit 1 remains unchanged, and $l_1 = \pm 1, m_2 = \pm 1$. Application of $M_{l_1=+1}^{\alpha_1=3}$ ($M_{l_1=-1}^{\alpha_1=3}$) on qubit 1 decouples qubits 1 and 2 from the rest of the graph and applies I (σ^3) on qubit 2, leaving it in the state $|+_j\rangle$ ($|-_j\rangle$). Therefore, further application of $M_{m_2=-1}^{\alpha_2=1}$ ($M_{m_2=+1}^{\alpha_2=1}$) on qubit 2 yields 0, implying that the $k_1 k_2 \equiv l_1 m_2 = (+1)(-1), (-1)(+1)$ outcomes will never occur. A similar situation arises in the case of the example shown in Fig. 1, where due to $V_{j=4}$ being a Hadamard operator, half of the set of 16 possible outcomes $k \equiv k_1 k_2 k_3 k_4$ are forbidden, given by the set

$$\begin{aligned} & (+1)(+1)(-1)(+1), & (+1)(+1)(+1)(-1) \\ & (+1)(-1)(+1)(+1), & (+1)(-1)(-1)(-1) \\ & (-1)(+1)(-1)(+1), & (-1)(+1)(+1)(-1) \\ & (-1)(-1)(+1)(+1), & (-1)(-1)(-1)(-1) \end{aligned}$$

We point out here that the occurrence of such forbidden sets of measurement outcomes depends completely on the choice of the specific PMS α . Therefore, one can divide the PMSs into two categories: (1) the ones forming the set Γ , for which all the measurement outcomes are allowed and (2) the ones constituting the set $\bar{\Gamma}$, for which occurrence of such forbidden set is possible. For instance, in the example presented in Fig. 2, $\alpha \equiv 33$, i.e., $\alpha_1 = 3, \alpha_2 = 3$ represents a PMS belonging to Γ . Note also that the subgraph G'_S after the application of $M_{l_1=\pm 1}^{\alpha_1=3}$ (in Fig. 2, this corresponds to the nodes a and b and the link connecting these two nodes), being fully decoupled from the nodes in S'_2 , is not affected by the application of $M_{m_2=1}^{\alpha_2=1}$ on the nodes in S'_2 . Therefore, in the case of pure graph states, this does not change the value of $E(\rho_S^k)$, and hence E_S^P .

C. Examples

By virtue of Proposition 1 and Corollary 1.1, it is now possible to localize entanglement over a subsystem S of a multiqubit system, via an optimization over 3^{N-n} reduced graph states $\{|G'_\alpha\rangle\}$, resulting from all possible PMSs, labeled by α , where $N - n$ is the size of S' . The localized entanglement over S is *genuinely multipartite* in nature if the subgraph G'_S , corresponding to the state $|G'_S\rangle$, in G'_α is a connected one. Therefore, to obtain RLGME, one can perform the optimization in Eq. (28) over only those G'_α for which G'_S is connected. While this restriction over the optimization may still yield a large number of connected graphs over S making the optimization difficult, in the case of *typical* regular graphs, e.g., the linear graph, the graph with a ladder structure, and the square graph, the number of G'_α resulting in a connected subgraph G'_S is considerably low and therefore advantageous. Moreover, the connected subgraphs G'_S can be further classified into different *orbits* such that the members of individual orbits are connected to each other via local complementation operations and graph isomorphism [43,48,64], thereby having identical GME. Therefore, the number of connected subgraphs that one needs to consider for performing the optimization in Eq. (28) can be reduced to the number of orbits, as we demonstrate in the following examples. Note also that in order to *quantify* the LGME, one needs to compute a GME measure over

³See discussions related to Eqs. (B4) and (B8)–(B9) in Appendix B for clarity.

⁴The probabilities for finding these outcomes vanish.

G_S^α , which can still be a nontrivial task due to the possible optimizations involved in the calculation. In this paper we use the *Schmidt measure* [43,48] and the *generalized geometric measure* (GGM) [83,97,98] for this purpose in the noiseless scenario, the definition of which can be found in Appendix C.

1. Two-qubit subsystems in arbitrary graph

We first revisit the extensively investigated case of the two-qubit subsystem on an arbitrary graph. It is well known [43] that the optimal PMS corresponding to localizing maximum entanglement on the chosen two-qubit subsystem S in an arbitrary graph G is given by either (1) σ^3 measurement on all qubits except the chosen subsystem if a direct link exists between the chosen qubits in the graph or (2) σ^1 measurements on all qubits on a chosen path between the two qubits belonging to S , and σ^3 measurements everywhere else. The former involves a decoupling of S from the rest of the qubits in G , thereby leaving only a connected pair of qubits in S . On the other hand, in the latter prescription, the σ^1 measurements create a direct link between the two chosen qubits, while the σ^3 measurement decouples S from the rest of the qubits. The purpose of maximizing the localizable entanglement is fulfilled due to the fact that a connected graph of two qubits is equivalent to a maximally entangled Bell state, or its local unitary equivalents, which are also maximally genuinely multipartly entangled. It is straightforward to see that for an arbitrary graph G , the PMS described in prescription 2, via the graph transformations introduced in Sec. III B 1, leads to a reduced graph where the selected nodes are connected by a direct link, thereby leading to maximal entanglement over S . See Fig. 3 for a demonstration. It is worthwhile to note that there may be a number of paths between the chosen qubits in G , each of which results in a specific optimal PMS for the LE, and subsequently a specific reduced graph with a link between the qubits in S . However, each such PMS guarantees the creation of a Bell pair or its local unitary equivalent on S .

2. Connected subsystems in linear graphs

We next consider a subsystem of qubits, S , in a linear graph. Here S forms a *connected patch*, such that each of the qubits in this patch is connected via a link with at least one other qubit in the same patch (see Fig. 4). We further assume that S contains more than two qubits. As discussed above, we are interested only in the PMSs that provide a connected G_S^α on S . We find that the application of the protocol discussed in Sec. III B 1 leads to only *linear connected graphs* on S [see Fig. 4(b)], irrespective of whether S is situated in the *bulk*, or at the *boundary* of the linear graph [see Fig. 4(a)], for all PMSs that lead to a connected G_S^α . Therefore, RLGME over a connected subsystem S on a linear graph equals the GME in a linear graph of size $|S| = n$, which is known to be $\lfloor n/2 \rfloor$ [48] when the Schmidt measure is used for quantification.

3. Connected subsystems in square graph

We next consider a square graph and take one of the plaquettes as the chosen subsystem S . The plaquette can be located in the bulk, or at the corner, or at one of the boundaries of the graph [see Fig. 5(a)]. In the situations where it is located in the bulk, or at the boundary, application of the methodology

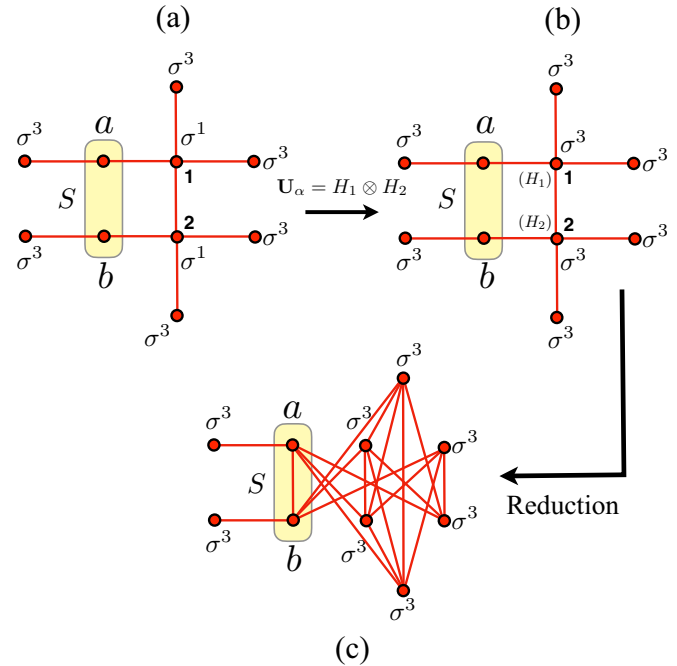


FIG. 3. Transformation of a graph as per the discussion in Sec. III B 1 and Appendix A when σ^1 measurements are performed on qubits 1 and 2 situated on the path connecting the qubits a and b in subsystem S (denoted by the shaded region). In the reduced graph, a link exists between the qubits a and b , such that decoupling of S from the rest of the qubits leads to a connected qubit pair on S , resulting in a maximally entangled Bell pair. The components of the local unitary transformations U_α (V_α is identity here) are shown in parentheses.

described in Sec. III B 1 and Appendix A leads to a total of 38 possible connected G_S^α [see Fig. 5(b)] in the reduced graphs $\{G'_\alpha\}$, obtained from all possible PMSs, labeled by α . The 38 connected subgraphs can further be divided into two orbits: (1) one containing the star subgraphs and the fully connected subgraph on S [see Fig. 5(b)] and (2) the other containing the rest 33 connected subgraphs. Since the members of individual orbits are connected to each other via local complementation (see Appendix A for definition) and graph isomorphism, they have identical entanglement properties, and it is therefore

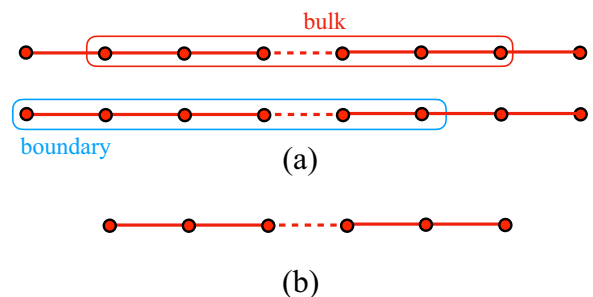


FIG. 4. (a) Connected subsystem of qubits situated at the boundary or bulk of a linear graph. (b) The only connected graph G_S^α that may occur on such a subsystem S in a linear graph as a result of the application of the PMSs, denoted by α , on the graph is a linear graph on S .

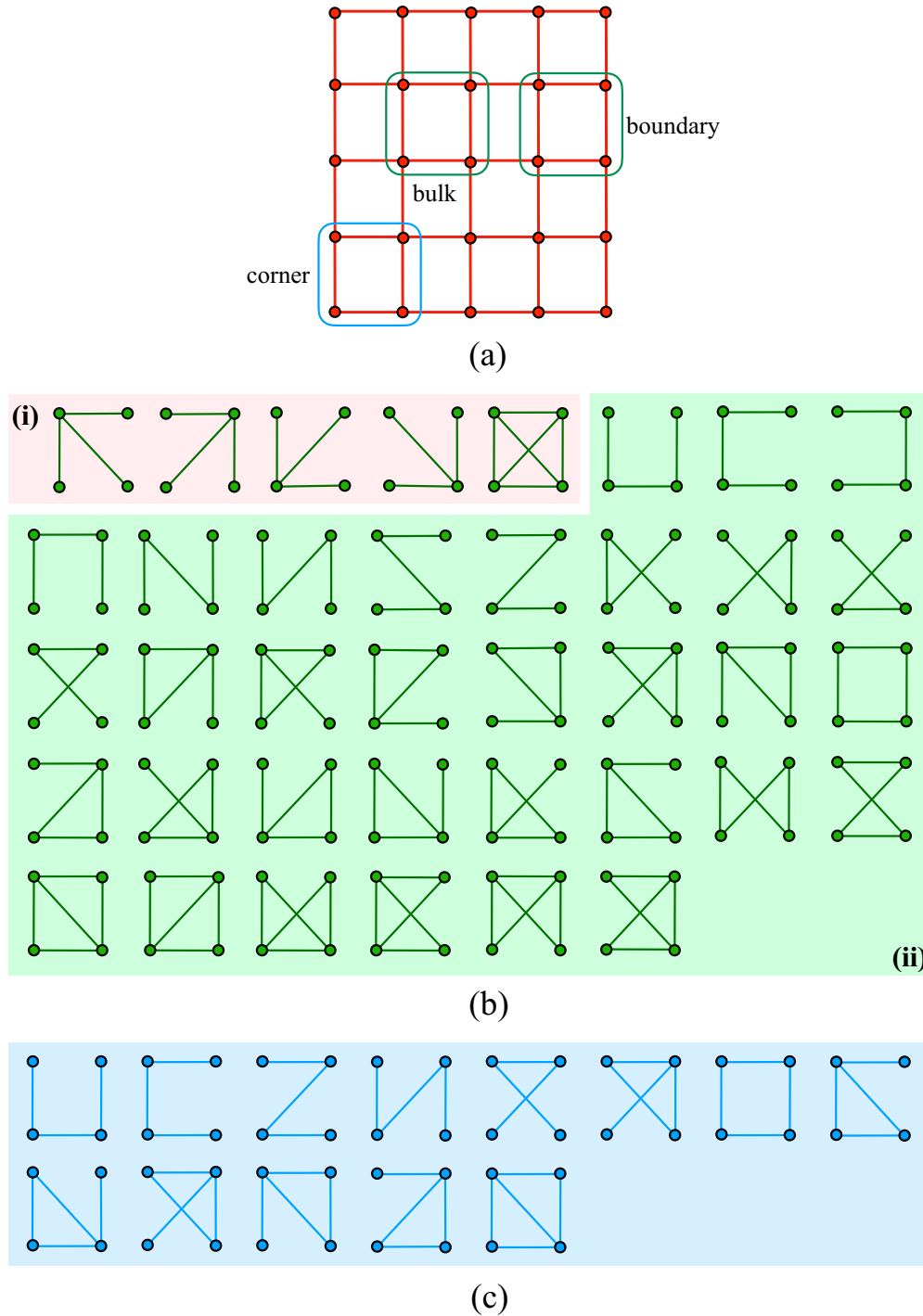


FIG. 5. (a) A plaquette of four qubits as the chosen subsystem S on a square graph, situated at the corner, bulk, or boundary of the graph. (b) If the plaquette S is located at the bulk or the boundary, there are 38 possibilities for the four-qubit connected subgraph G_S^α in the reduced graphs $\{G_\alpha\}$. These 38 four-qubit graphs can be further divided into two orbits, shown as two separate shaded blocks (i) and (ii), containing 5 and 33 subgraphs, respectively. (c) If the four-qubit plaquette is located at one corner of the graph, then the number of possibilities for G_S^α is reduced to 13, all of which belong to the same orbit.

sufficient to consider a representative from each of the orbits to perform the optimization in Eq. (28). The lower and the upper bounds of the Schmidt measure for G_S^α in (1) are found to be equal to 1, while for G_S^α in (2) it is 2. This implies that the values of the Schmidt measure in these two cases are 1 and 2, respectively, leading to $E_S^P = 1$ and $E_S^P = 2$, respectively.

On the other hand, if the chosen four-qubit plaquette is located at one of the corners of the square graph, the number of connected subgraphs G_S^α reduces to 13 [see Fig. 5(c)], all of which belong to the same orbit. Therefore, it is sufficient to compute the Schmidt measure of any one of these 13 subgraphs. Similar to the former case, here also the upper and

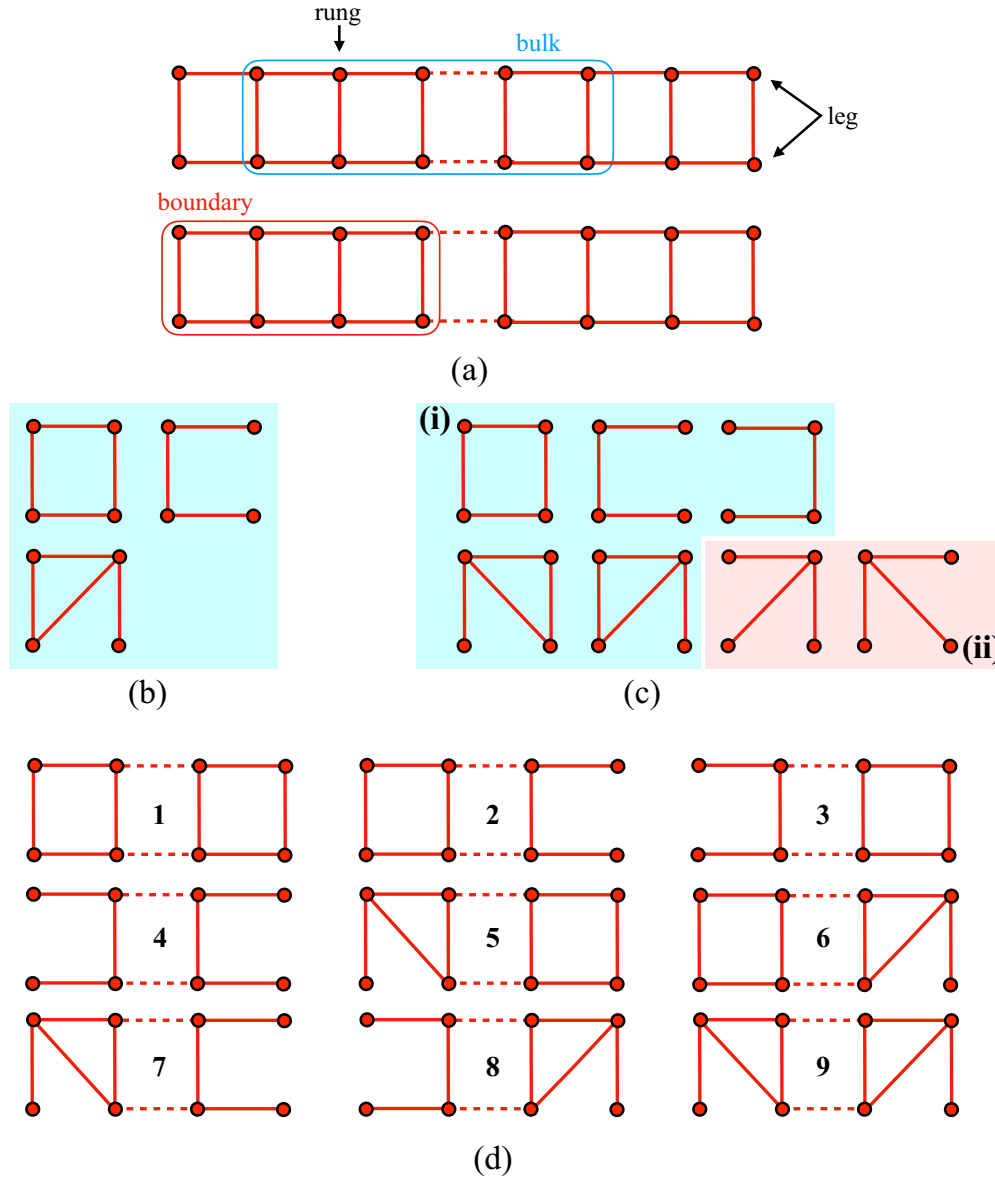


FIG. 6. (a) A set of $2R$ connected qubits, where $R (< N/2)$ is the number of rungs, as the chosen subsystem S on a graph with a ladder structure with two *legs* and $N/2$ *rungs*, N being the total number of qubits. The subsystem S can be situated at the bulk, or the boundary of the graph. (b) For $R = 2$ and S is connected and is located at the boundary, only three distinct connected subgraphs G_S^α are possible on S , all of which belong to a single orbit. (c) However, if the connected subsystem S with $R = 2$ is in the bulk of the system, there are seven possibilities for the four-qubit connected subgraph G_S^α , including the four-qubit star graph, which can be divided into two orbits, (i) and (ii), shown in two different shaded blocks. (d) If the subsystem S is connected and is constituted of $R > 2$ rungs, then a total of nine possibilities for the connected subgraphs G_S^α arise.

lower bounds of the Schmidt measure are found to be equal, having a value 2, which leads to $E_S^P = 2$.

4. Connected subsystems in ladders

We now consider a graph having a ladder structure [see Fig. 6(a)] where two legs are connected by rungs and the nodes of the graph are the points where the rungs meet the legs. We choose a connected subsystem consisted of a number, say, R , of rungs of the ladder as S and apply the protocol described in Sec. III B 1 and Appendix A. For $R = 2$, and S situated at the boundary, the set of connected subgraphs $\{G_S^\alpha\}$

consists of only three four-qubit graphs, given in Fig. 6(b), and $E_S^P = 2$ as in the cases described earlier. On the other hand, if the two-rung subsystem is situated in the bulk of the ladder, then the four-qubit star graphs also appear in the set of connected subgraphs $\{G_S^\alpha\}$, containing a total of seven distinct graph structures that can be divided into two orbits [see Fig. 6(c), with two orbits marked by (i) and (ii)]. Here we have reduced the number of graphs in an orbit by discarding the four-qubit graphs that are connected directly by local complementations with any one of the members of the orbit. In this case also, the RLGME, as quantified by the Schmidt measure, is obtained as $E_S^P = 2$.

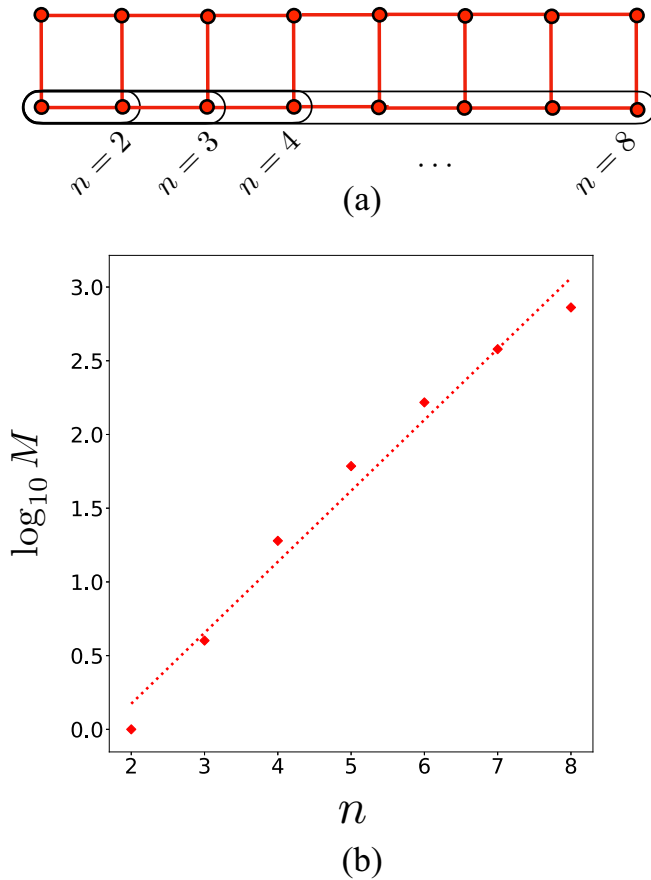


FIG. 7. (a) Connected subsystem of qubits of size n ($2 \leq n \leq 8$) in the form of a linear subgraph on one of the legs of the two-leg ladder graph. (b) Variation of $\log_{10} M$ with n for $N = 16$, where M is the total number of connected subgraphs $\{G_S^\alpha\}$ resulting from the reduced graphs $\{G'_\alpha\}$, obtained by the application of all PMSs on S' . The data are fitted to a straight line of slope 0.481 and intercept -0.788 . See Eq. (29).

We now consider the scenario of a connected subsystem S with $R > 2$ rungs. We find that the set of connected G_S^α on S in G'_α , obtained from the PMSs denoted by α , contains only nine distinct connected graph structures, shown in Fig. 6(d), labeled as 1–9, where graphs that are connected to structures 5–9 via local complementation are discarded. Moreover, each of these nine connected graphs on G_S^α has the same value for the lower and upper bounds of the Schmidt measure, implying that the value of the measure is equal to either of the bounds. In the case of $R = 3$ ($n = 6$), the value of the Schmidt measure for the structure 4 is 2, while all of the other graphs in Fig. 6(d) have the value of the Schmidt measure equal to 3, implying that $E_S^{\mathcal{P}} = 3$. On the other hand, for all cases with $R > 3$ ($n > 6$), for each of structures 1–9, the Schmidt measure is given by $n/2$, implying that the RLGME, as quantified by the Schmidt measure, is $n/2$.

We further consider a connected subsystem S in the form of a linear graph on one of the legs of the ladder [see Fig. 7(a)], where the size, n , of S is increasing. In this situation, with increasing n , the number, M , of connected subgraphs $\{G_S^\alpha\}$ increases exponentially [see Fig. 7(b)] with n as

$$M = 10^{\alpha + \beta n}, \quad (29)$$

where α and β depends on N , and can be determined from fitting the data to Eq. (29).⁵ However, the RLGME, as quantified by the Schmidt measure, has the value $\lfloor n/2 \rfloor$.

Note that we also compute the RLGME in terms of the GGM, which is a measure for the GME present in a quantum state, for each of the above cases, and find it to be $1/2$ for all the examples. This implies that genuine multipartite entanglement is localized on all the chosen subsystems S in all the examples. We comment on the loss of LGME with introduction of noise in Sec. IV.

D. Localizable bipartite entanglement

It is worthwhile to point out here that one can also compute localizable bipartite entanglement over a chosen bipartition of the subsystem S using the same methodology. However, the optimization in Eq. (28), in this case, has to be performed over all possible subgraphs G_S^α , connected or otherwise, obtained from all possible reduced graphs G'_α , resulting from the PMSs. Therefore, for an arbitrary graph G , the optimization can be more demanding compared to the calculation of RLGME. However, a few conclusions can be drawn without performing the optimization. For example,

(a) If at least one connected G_S^α is obtained for the subsystem S and

(b) If the chosen bipartition $A:B$ of S is such that A is made of only 1 qubit, and B consists of the rest of the qubits in S ,

then maximum bipartite entanglement will be localized between A and B since all qubits in a connected graph has maximally mixed marginals [43,99] (see Appendix C 1). Note that this is the case for all the examples discussed above. Further, if $n = 2, 3$ in addition to the conditions (a) and (b), where $|S| = n$, then maximum bipartite entanglement can be localized over all bipartitions in S . For $n > 3$, relaxing condition (b) and assuming A to be the smaller subsystem constituted of at least two qubits $\{i, j\} \in G_S^\alpha$, $\rho_A = \text{Tr}_B(|G_S^\alpha\rangle\langle G_S^\alpha|)$ is either maximally mixed or a rank-2 mixed state [43]. In the case of the former, $|G_S^\alpha\rangle$ is maximally entangled in the bipartition $A:B$, whereas in the case of the latter it is not. Similar conclusions on the localizable bipartite entanglement over the partition $A:B$ in S hold.

IV. LGME IN NOISY GRAPH STATES

We now provide a brief description of the noise models considered in this paper and discuss the calculation of $E_S^{\mathcal{P}}$ and one of its lower bounds corresponding to a specific PMS in graph states under Markovian and non-Markovian noisy channels.

A. Single-qubit Pauli noise on graph states

To describe the effect of single-qubit Pauli noise on the graph states, we use the Kraus operator formalism as

$$\rho = \Lambda(\rho_0) = \sum_s K_s \rho_0 K_s^\dagger, \quad (30)$$

⁵For example, with $N = 16$, $\alpha = -0.788$, and $\beta = 0.481$.

where $\{K_s\}$ are the Kraus operators satisfying

$$\sum_s K_s^\dagger K_s = I, \quad (31)$$

with I being the identity operator in the Hilbert space of the N -qubit graph. The states $\rho_0 = |G\rangle\langle G|$, and ρ denote, respectively, the pure graph state, and the mixed state of the system under noise. In the case of Pauli noise, individual Kraus operators are $K_s = \sqrt{q_s} J_s$, where

$$J_s = \otimes_{i=1}^N \sigma_i^{s_i}, \quad (32)$$

$$q_s = \prod_{i=1}^N q_{s_i}, \quad (33)$$

with $s_i \in \{0, 1, 2, 3\} \forall i \in G$, and $\sum_{s_i=0}^3 q_{s_i} = 1$. Note here that the index s on the left-hand side can be interpreted as the multiindex $s \equiv s_1 s_2 \dots s_N$. The factorized form of q_s implies that no spatial correlation exists between the qubits in the graph. In this paper we focus on nondissipative Pauli channels. More specifically, we consider Markovian bit-flip (BF), bit-phase-flip (BPF), phase-damping (PD), and depolarizing (DP) noise channels. In terms of the probabilities associated to different Pauli operators in the maps, the BF, BPF, PD, and DP channels are given by

$$q_0 = 1 - \frac{q}{2}, \quad q_1 = \frac{q}{2}, \quad q_2, q_3 = 0, \quad (34)$$

$$q_0 = 1 - \frac{q}{2}, \quad q_2 = \frac{q}{2}, \quad q_1, q_3 = 0, \quad (35)$$

$$q_0 = 1 - \frac{q}{2}, \quad q_3 = \frac{q}{2}, \quad q_1, q_2 = 0, \quad (36)$$

and

$$q_0 = 1 - \frac{3q}{4}, \quad q_1 = q_2 = q_3 = \frac{q}{4}, \quad (37)$$

respectively, where $0 \leq q \leq 1$, and we assume q to be identical for all qubits.

There exists non-Markovian versions of the single-qubit Pauli noise, such as the non-Markovian PD⁶ and DP channels [88–90], given by

$$\begin{aligned} q_0 &= \left(1 - \frac{q}{2}\right) \left[1 - \epsilon \frac{q}{2}\right], \\ q_3 &= \frac{q}{2} \left[1 + \epsilon \left(1 - \frac{q}{2}\right)\right], \\ q_1 &= q_2 = 0, \end{aligned} \quad (38)$$

and

$$\begin{aligned} q_0 &= \left(1 - \frac{3q}{4}\right) \left[1 - \frac{9\epsilon q}{4}\right], \\ q_1 &= q_2 = q_3 = \frac{q}{4} \left[1 + 3\epsilon \left(1 - \frac{3q}{4}\right)\right], \end{aligned} \quad (39)$$

respectively, with $0 \leq q \leq 1$, and $0 \leq \epsilon \leq 1$. The Markovian PD and the DP channels are recovered from their non-Markovian counterparts for $\epsilon = 0$.

⁶The non-Markovian version of the BF and the BPF channels can also be defined in a similar fashion.

Note here that the stabilizer description of graph states implies that application of $\sigma_i^{s_i}$, $s_i = 1, 2$, on the qubit i in the graph state leads to

$$\begin{aligned} \sigma_i^1 |G\rangle &= \otimes_{j \in \mathcal{N}_i} \sigma_i^3 |G\rangle, \\ \sigma_i^2 |G\rangle &= \sigma_i^3 \otimes_{j \in \mathcal{N}_i} \sigma_i^3 |G\rangle. \end{aligned} \quad (40)$$

Therefore, all Pauli noise described in Eqs. (34), (37), and (39) are equivalent to PD noise [Eq. (36)], with a modified probability distribution $\{\tilde{q}_s\}$, which is not necessarily factorized [i.e., can not be written in a form similar to Eq. (33)]. Note also that a PD noise on a connected graph state results in a GD state [Eq. (6)], where all the diagonal elements of the density matrix are not necessarily nonzero.

B. Localizable entanglement via Pauli measurements

We now discuss the calculation of $E_S^{\mathcal{P}}$. For a chosen α representing a specific PMS, we proceed in a fashion similar to the pure graph states (see Sec. III B 1) and transform $\alpha_j \rightarrow 3 \forall j \in S'$ via the application of the local Clifford operation \mathbf{U}_α . Explicitly, we write

$$\begin{aligned} \varrho_k &= M_k^\alpha \left[\sum_s q_s J_s \rho_0 J_s^\dagger \right] M_k^{\alpha\dagger}, \\ &= \mathbf{U}_\alpha \left[\sum_s q_s M_k^\alpha J_{s'}^\alpha \rho_\alpha J_{s'}^{\alpha\dagger} M_k^{\alpha\dagger} \right] \mathbf{U}_\alpha^\dagger, \end{aligned} \quad (41)$$

where definitions of M_k^α and ρ_α are as in Sec. III B 1, respectively, and

$$J_{s'} = \mathbf{U}_\alpha^\dagger J_s \mathbf{U}_\alpha. \quad (42)$$

Further transformation of $\rho_\alpha \rightarrow \rho'_\alpha$ modifies Eq. (41) as

$$\varrho_k = \mathbf{U}_\alpha \mathbf{V}_\alpha \tilde{\varrho}_k \mathbf{V}_\alpha^\dagger \mathbf{U}_\alpha^\dagger, \quad (43)$$

with

$$\tilde{\varrho}_k = \sum_s q_s M_{l'_m}^\alpha J_{s'}^\alpha |G'_\alpha\rangle \langle G'_\alpha| J_{s'}^{\alpha\dagger} M_{l'_m}^{\alpha\dagger}, \quad (44)$$

where we have followed the notations introduced in Sec. III B 1, and

$$J_{s'} = \mathbf{V}_\alpha^\dagger J_s \mathbf{V}_\alpha. \quad (45)$$

Note here that since both \mathbf{U} and \mathbf{V} are Clifford unitaries, Pauli noise is mapped to Pauli noise (see Table I), and the transformation $s \rightarrow s' \rightarrow s''$ leads to the multi-index $s'' \equiv s'_1 s'_2 \dots s'_{N-n}$ with $s'_j = 1, 2, 3$ for $j \in S'$. Note further that

$$\sigma_j^{\alpha'_j} P_{l'_j, m'_j}^{\alpha_j} \sigma_j^{\alpha'_j} \rightarrow P_{l'_j, m'_j}^{\alpha_j}, \quad (46)$$

where $l'_j = l_j$ and $m'_j = m_j$ ($l'_j \neq l_j$ and $m'_j \neq m_j$) if $\alpha_j = \alpha'_j$ ($\alpha_j \neq \alpha'_j$), $\alpha_j, \alpha'_j = 1, 2, 3$, leading to

$$\tilde{\varrho}_k = \sum_s q_s J_{s''}^\alpha M_{l'_m}^\alpha |G'_\alpha\rangle \langle G'_\alpha| M_{l'_m}^{\alpha\dagger} J_{s''}^{\alpha\dagger}. \quad (47)$$

We now separately consider the two types of PMSs, constituting the sets Γ and $\bar{\Gamma}$, where $\Gamma \cup \bar{\Gamma}$ is the full set of all possible PMSs, and $\Gamma \cap \bar{\Gamma} = \emptyset$. The set Γ is defined such that for a specific PMS $\alpha \in \Gamma$, all outcomes k are equally

TABLE I. Transformation of Pauli matrices up to a phase factor under the Clifford operation U , where U represents the unitary operations U_i and V_i corresponding to the transformation of the graph state $\rho \rightarrow \rho_\alpha \rightarrow \rho'_\alpha$ (see Sec. III B 1). The transformation of the Pauli noise, as described in Sec. IV A, can also be determined using these transformations.

U	σ^s	$\sigma^{s'} = U^\dagger \sigma^s U$
H	σ^1	σ^3
H	σ^2	σ^2
H	σ^3	σ^1
R	σ^1	σ^2
R	σ^2	σ^1
R	σ^3	σ^3
RH	σ^1	σ^2
RH	σ^2	σ^3
RH	σ^3	σ^1

probable with probability $2^{-(N-n)}$, which is not true for a PMS belonging to $\bar{\Gamma}$. Under this consideration, the optimization of RLGME can be considered as $E_S^{\mathcal{P}} = \max\{E_S^\Gamma, E_S^{\bar{\Gamma}}\}$, where [see Eq. (14)]

$$E_S^\Gamma = \max_{\alpha \in \Gamma} \sum_{k_\alpha=0}^{2^{N-n}-1} p_{k_\alpha} E(\rho_S^{k_\alpha}),$$

$$E_S^{\bar{\Gamma}} = \max_{\alpha \in \bar{\Gamma}} \sum_{k_\alpha=0}^{2^{N-n}-1} p_{k_\alpha} E(\rho_S^{k_\alpha}), \quad (48)$$

where we have reinstated the index α in k to make the equations comprehensive. Starting with the set Γ , the following proposition can be written (see Appendix D for the proof).

Proposition 2. For a subsystem S of an arbitrary graph state subjected to single-qubit Pauli noise on all qubits, if the chosen Pauli measurement setup on S' with $S \cup S'$ constituting the entire system is such that $\alpha \in \Gamma$, then the average entanglement postmeasurement on the subsystem S is independent of the measurement outcomes and depends only on α . ■

Using Proposition 2 in Eq. (48), Corollary 2.1 is straightforward.

Corollary 2.1. The value of E_S^Γ on the subsystem S is given by

$$E_S^\Gamma = \max_{\alpha \in \Gamma} [E(\rho_S^k)]. \quad (49)$$

See Eq. (D3) for the definition of ρ_S^k . Note that Eq. (49) reduces to Eq. (28) in the absence of noise and in a situation when $\bar{\Gamma}$ is a null set. ■

Similar to the proof of Proposition 1 and Corollary 1.1 (see Appendix B), the proof of Proposition 2 and Corollary 2.1 is also established on the fact that for $\alpha \in \Gamma$, the postmeasured states ρ_S^k on S corresponding to different k are local unitarily connected to each other, where the unitary operators are constructed by single-qubit unitary operators. Therefore ρ_S^k for different k have the same entanglement content (see Appendix D). In contrast, in the situation where $\bar{\Gamma}$ has a nonzero cardinality, and for a PMS $\alpha \in \bar{\Gamma}$, ρ_S^k corresponding to different k are, in general, not connected by local unitary operators.

In this case, explicit calculation depends on the fact that the change $lm \rightarrow l'm'$ may result in a transition between allowed and forbidden sets of outcomes, making the computation for the postmeasured states ρ_S^k difficult. For interested readers, we demonstrate the calculation step by step in Appendix E in both the cases of $\alpha \in \Gamma$ and $\alpha \in \bar{\Gamma}$, using the example of the graph in Fig. 2. However, in all the specific examples considered in this paper, we restrict ourselves to specific PMSs belonging to Γ , as discussed in Sec. IV C and V, where Proposition 2 and Corollary 2.1 are applicable.

C. Examples

We now revisit the examples considered in Sec. III C but in the presence of single-qubit Pauli noise of different types, which adds obstacles in quantifying the LGME. On one hand, understanding how to characterize mixed states in terms of GME is far from complete, and computable measures of multipartite entanglement in mixed states are scarce [1]. On the other hand, in the case of the mixed states, the manifestation of the effect of the measurement outcomes is different compared to the pure graph states, indicating the necessity of rigorous optimization over all 3^{N-n} PMSs. To overcome these challenges, we focus on a lower bound of the RLGME (and in consequence, of LGME), which can be obtained by judiciously choosing a PMS, labeled by α_c . Since the definition of RLGME involves a maximization over all possible α , the average entanglement $E_S^{\alpha_c}$ obtained for the chosen PMS α_c provides a lower bound of $E_S^{\mathcal{P}}$ and therefore of E_S i.e., $E_S^{\alpha_c} \leq E_S^{\mathcal{P}} \leq E_S$. The existence of LGME on S is guaranteed by an α_c such that $E_S^{\alpha_c} > 0$. We refer to $E_S^{\alpha_c}$ as the *floor* of LGME (FLGME).

A word on the choice of the PMS labeled by α_c is in order here. We choose α_c such that

- $\alpha_c \in \Gamma$, i.e., all measurement outcomes corresponding to the PMS α_c are equally probable with probability $1/2^{N-n}$
- The subgraph $G_S^{\alpha_c}$ on S in the reduced graph G_{α_c}' is a connected graph and
- The pattern of the PMS can be generalized to any system size.

We find that such a PMS α_c can be constructed in terms of only σ^1 and σ^3 measurements for all the examples discussed in Sec. III C. See Fig. 8 for a demonstration.

In this section we particularly focus on the evolution of a quantum state from having GME localized on a chosen subsystem to a state where the postmeasured states on S are biseparable. Noticing that the postmeasured states on S after Pauli measurements are GD states in the case of Pauli noise (see Sec. IV B), we choose four-qubit subsystems as S , for which the criteria for the GD state being genuine multipartite entangled are known [100] (see Appendix G 2 for details). Using these criteria, for each PMS labeled by α , a *critical* value of q , denoted by q_c , can be determined such that for $q_c \leq q \leq 1$, all postmeasured states corresponding to the PMS α are biseparable. For the choice of $\alpha = \alpha_c$, the values of q_c are plotted (see Figs. 9 and 10) against the non-Markovianity parameter ϵ corresponding to the different types of Pauli noise (see Sec. IV A) for the different cases discussed in Sec. III C, where the subsystem S is a four-qubit one. From the figures,

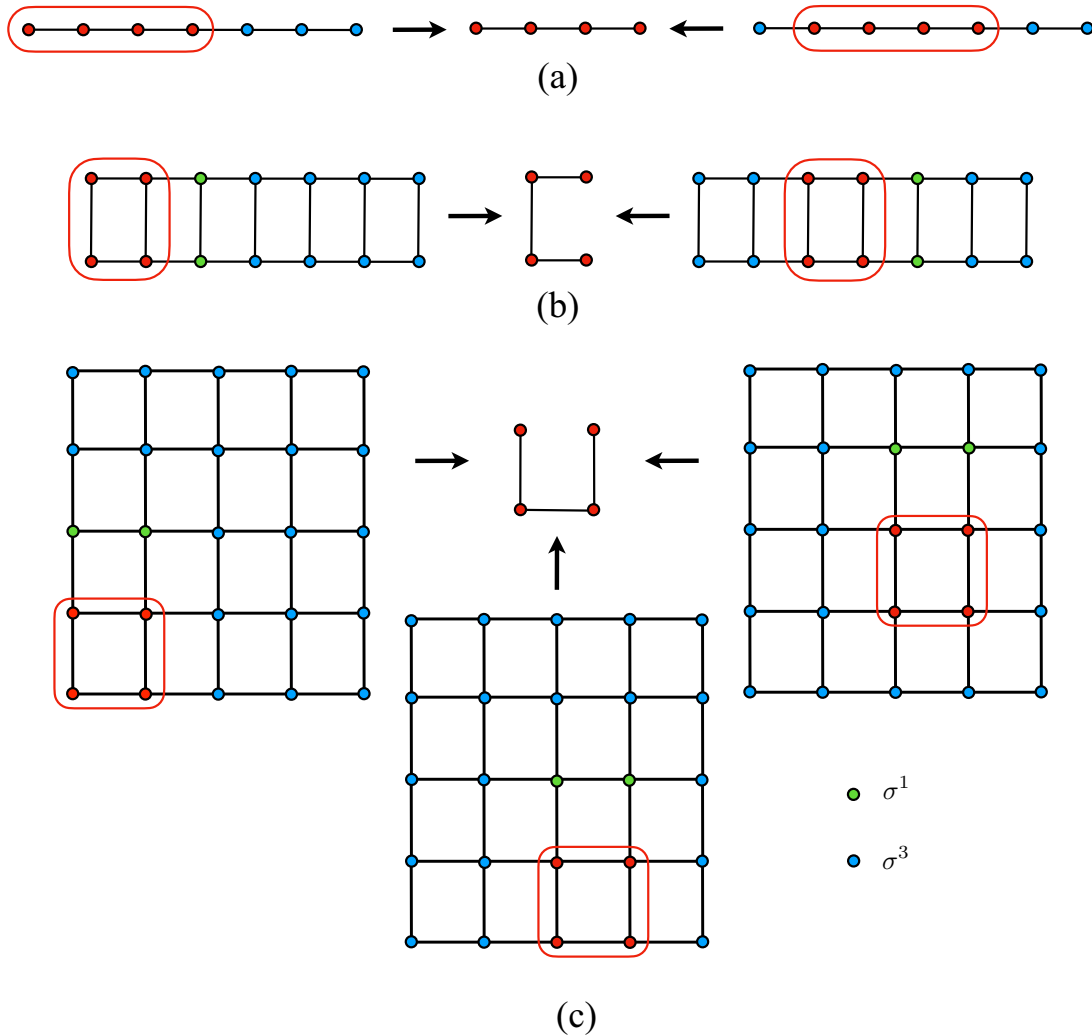


FIG. 8. The PMS used for the lower bound calculation in noisy (a) linear (boundary, bulk), (b) ladder (boundary, bulk), and (c) square (corner, boundary, bulk) graph structures. The red nodes indicates the unmeasured four nodes on which a GD state of linear graph will be localized. The blue(green) nodes indicates σ^3 (σ^1) measurements. Translation to any higher system size requires only additional σ^3 measurements on the additional nodes maintaining the σ^1 measurement pattern w.r.t. localizing four nodes.

the following observations can be made:

(a) For the PMS denoted by α_c and for a specific type of Pauli noise, the values of q_c depend on the effective neighbourhood S'_1 of S (see the discussion in Appendix F for the definition of S'_1). As one moves from the periphery (corner or boundary) to the bulk of the graph, $|S'_1|$ increases, and q_c decreases.

(b) Note, however, that in the case of PD noise [Figs. 9(c) and 10(c)], $|S'_1|$ remains the same in the case of the bulk, the boundary, and the corner, which manifests in q_c remaining the same for all these cases.

(c) Moreover, for all types of Pauli noise and for a specific category of subsystem S (bulk, boundary, or corner), the value of q_c decreases with increasing ϵ , implying a quicker loss of FLGME with increasing non-Markovianity in the noise.

(d) In the case of the BF, BPF, and PD noise, q_c has a quadratic dependence on ϵ ($q_c \sim a_2\epsilon^2 + a_1\epsilon + a_0$), while in the case of the DP noise, a cubic dependence ($q_c \sim a_3\epsilon^3 + a_2\epsilon^2 + a_1\epsilon + a_0$) is observed. The values of the parameters

a_i s ($i = 1, 2, 3$) depends on the type of noise, the choice of the graph, and the location of the subsystem S in the graph, while a_0 is the value of q_c for $\epsilon = 0$.

We point out here that for a specific type of Pauli noise, the values of q_c are independent of system size, N , for the chosen PMS α_c (cf. [101]). The values of q_c in the Markovian cases can be extracted from the data for $\epsilon = 0$ (see Sec. IV A). Due to the maximization involved in the definition of LGME, the actual critical noise strength beyond which the LGME perishes is greater than, or equal to, q_c . Note further that in the case of noisy systems with even noise models as simple as Pauli noise, it is not guaranteed whether $E_S = E_S^P$. While the equality can occur for specific noise types and for specific values of the noise strength, in general, $E_S^P < E_S$. This calls for a comment on the performance of $E_S^{\alpha_c}$ and E_S^P as lower bounds of E_S . We revisit this in Sec. V, with an example of a stabilizer state from Kitaev's toric code [92,93].

Note that in the above examples, (q_i, ϵ_i) s on different qubits are assumed to be identical. One can also consider a scenario where different noise of different strengths and

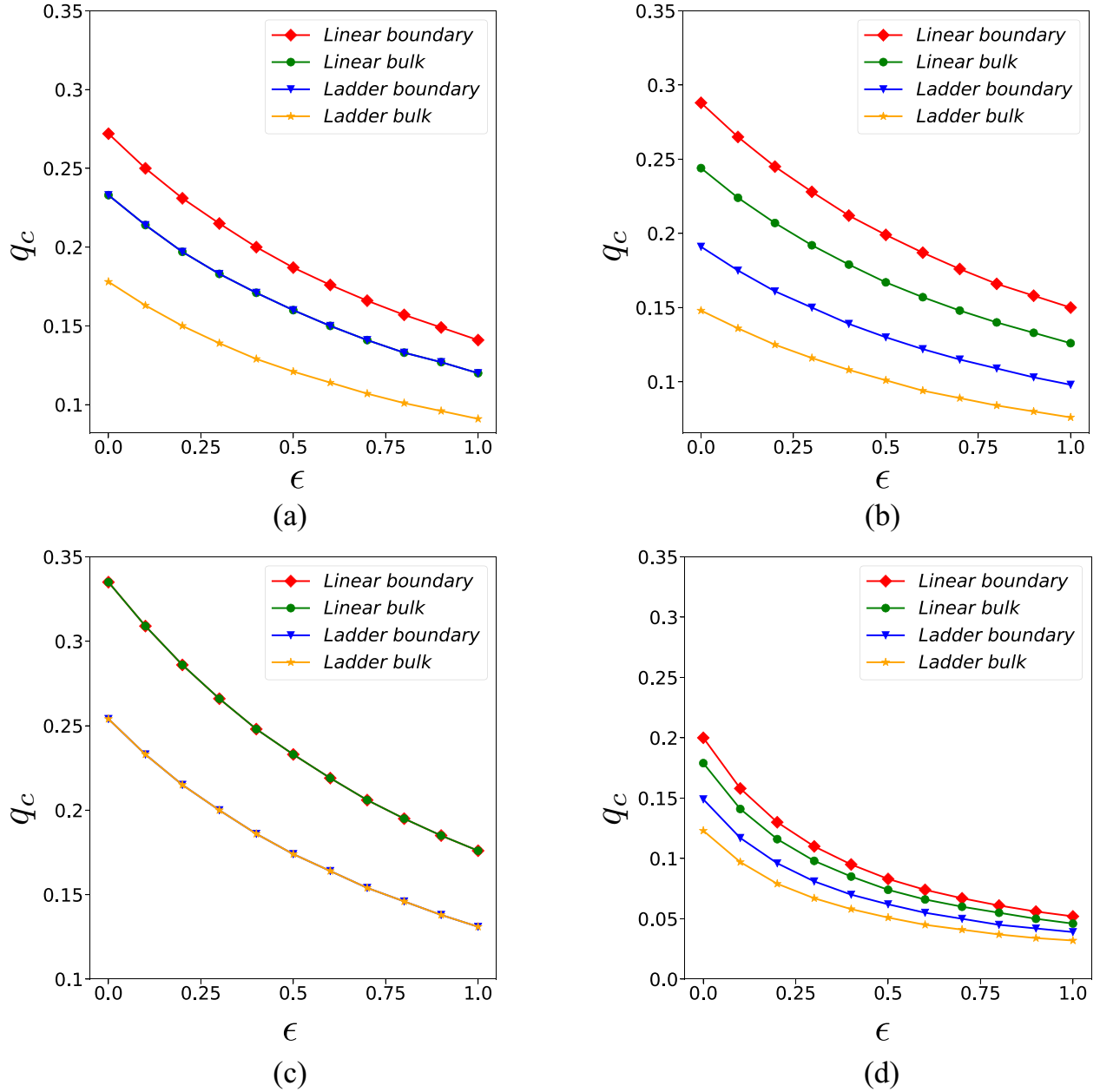


FIG. 9. Variations of q_c as a function of ϵ in the case of the (a) BF, (b) BPF, (c) PD, and (d) DP noise, for a connected subsystem S of four qubits [see Figs. 8(a) and 8(b)] located at the boundary, or bulk of a linear graph, and a graph in the shape of a ladder. All the axes in all figures are dimensionless.

different non-Markovianity parameters apply to the qubits (see Appendixes D and F), and similar methodologies apply. For a demonstration, consider the example of the eight-qubit graph shown in Fig. 11(a), where different types of noises with different strengths q as well as different values of the non-Markovianity parameter ϵ are applied on different qubits. For the graph shown in Fig. 11(a), Eq. (F8) of Appendix F representing the probability associated with the subclass $(r, m) = (2, 1)$ constituted of qubits 2, 3, and 4 takes the form

$$\begin{aligned}
 P_1(2, 1) &= p_2 + p_3 + p_4 - 2(p_2p_3 + p_3p_4 + p_2p_4) \\
 &\quad + p_2p_3p_4, \\
 P_0(2, 1) &= 1 - P_1(2, 1).
 \end{aligned}
 \tag{50}$$

where $p_i = \frac{q_i}{2}[1 + \epsilon_i(1 - \frac{q_i}{2})]$ for $i = 2, 3, 4$ are the probability for occurrence of noise on i th qubit. In Fig. 11(b) we plot the FLGME as a function of the noise parameters q_b and q_3 . We point out here that this example deals with different types of Pauli noise and different noise strengths, as well as different non-Markovianity parameters for different qubits, and thereby is a typical case of the most general scenario covered by the noise model and the methodology considered in this paper.

V. APPLICATION IN TOPOLOGICAL QUANTUM CODES

Since any stabilizer state can be mapped to a graph state via local unitary transformations belonging to the Clifford group

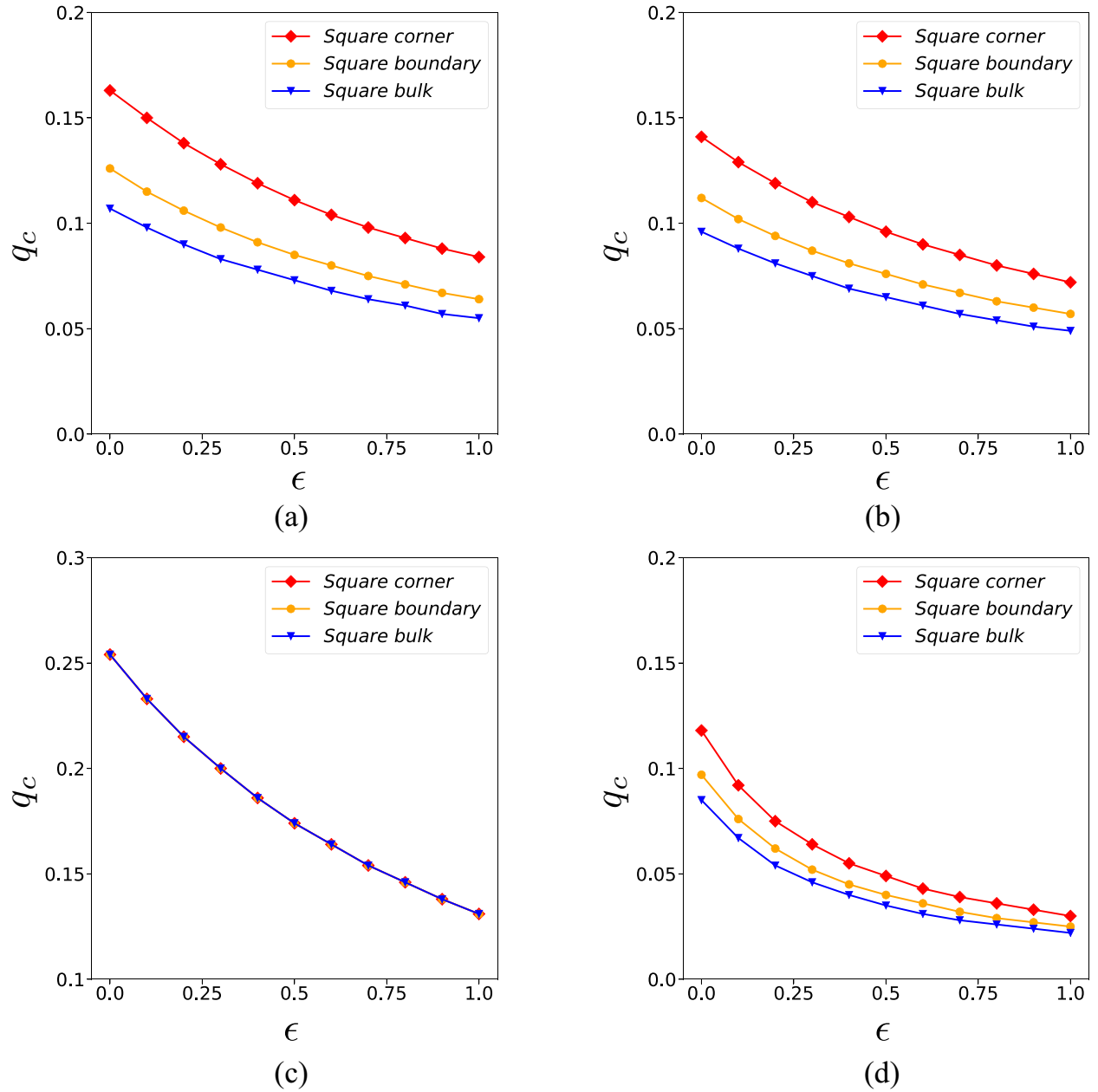


FIG. 10. Variations of q_c as a function of ϵ in the case of the (a) BF, (b) BPF, (c) PD, and (d) DP noise, for a connected subsystem S of four qubits [see Fig. 8(c)] located at the boundary, corner, or bulk of a square graph. All the axes in all figures are dimensionless.

[61], the methodology discussed in Secs. III–IV can also be applied to any stabilizer state, as long as the structure of the graph underlying the local unitarily connected graph state is known. In this section we demonstrate this by applying the protocol to the toric code [92,93] defined on a square lattice, where each qubit in the system is placed on one of the edges of the lattice (see Fig. 12). Two types of stabilizer operators, namely, the plaquette operators $\mathcal{S}_p = \otimes_{i \in p} \sigma_i^3$ and the vertex operators $\mathcal{S}_v = \otimes_{i \in v} \sigma_i^1$ are defined on the toric code, where p and v are, respectively, the plaquette and the vertex index. The stabilizer state $|\mathcal{S}\rangle$ on the toric code is given by the common eigenstate of all the stabilizer operators corresponding to the (+1) eigenvalue:

$$\mathcal{S}_p |\mathcal{S}\rangle = (+1) |\mathcal{S}\rangle, \quad \mathcal{S}_v |\mathcal{S}\rangle = (+1) |\mathcal{S}\rangle. \quad (51)$$

Under the periodic boundary condition assumed along both the horizontal and the vertical directions, the square lattice can be embedded on a *genus-1* torus, hosting two nontrivial loops. We denote the sets of nodes, in the horizontal and vertical directions, on which these nontrivial loops are defined by H and V , respectively (see Fig. 12), and represent four nontrivial loop operators as

$$\mathcal{L}_\alpha^1 = \otimes_{i \in \alpha} \sigma_i^1, \quad \mathcal{L}_\alpha^3 = \otimes_{i \in \alpha} \sigma_i^3, \quad (52)$$

with $\alpha = H, V$.

In this section, we apply the methodology discussed in Secs. III and IV on the stabilizer states $|\mathcal{S}\rangle$ and localize GME on the nontrivial loops in the horizontal or the vertical direction. Note that in the case of a square lattice of $N_p \times N_p$ architecture hosting a Kitaev model, where N_p is the number

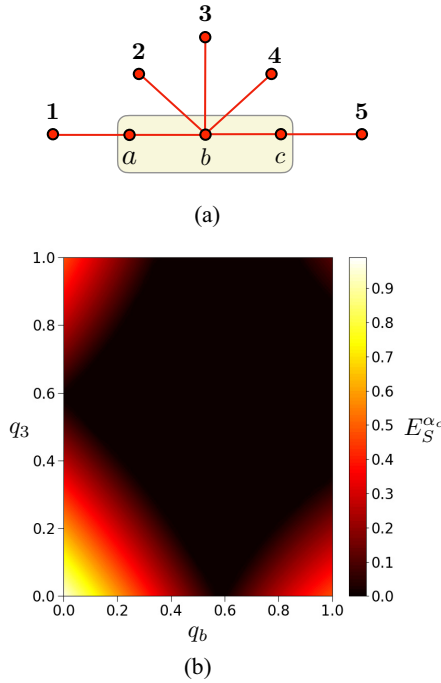


FIG. 11. (a) Example of an eight-qubit graph, where the noise applied on different qubits is as follows: 1: BF (5×10^{-3} , 10^{-1}), 2: BPF (10^{-3} , 1.0), 3: BF (q_3 , 1.0), 4: BF (10^{-3} , 7×10^{-1}), 5: BPF (3×10^{-3} , 9×10^{-2}), a : BF (4×10^{-3} , 8×10^{-1}), b : BPF (q_b , 1.0), c : PD (8×10^{-3} , 9×10^{-1}), where the numbers in parentheses are the values of (q, ϵ) . The FLGME is computed over the subsystem S constituted of the three qubits labeled by a , b , and c . (b) Variation of FLGME (quantified by genuine multiparty concurrence; see Appendix G) as a function of q_b and q_3 , where the PMS α corresponds to σ^3 measurements on qubits 1–5. All quantities plotted are dimensionless.

of plaquettes in the horizontal or vertical direction, the number of qubits in the system grows as $N = 2N_p^2$, while the size of a nontrivial loop is N_p . Therefore, the protocol discussed in Secs. III and IV requires an optimization over all the reduced graphs having a connected subgraph G_S^α on S , which are obtained from $3^{N_p(2N_p-1)}$ PMSs. While computation for pure states is still possible for moderately large system size, in the case of noisy toric codes, this is practically impossible

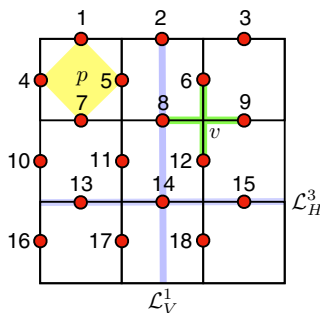


FIG. 12. A toric code of 18 qubits on a square lattice, where each of the plaquettes p and the vertices v are constituted of four qubits. Periodic boundary condition is assumed along both the horizontal and the vertical directions on the lattice.

to compute when N_p (and subsequently N) is large. However, following the same approach as in the case of the noisy graph states, one may compute FLGME, as we discuss below.

The stabilizer state $|S\rangle$ can be mapped to a graph state via Hadamard operations on judiciously chosen qubits [91], referred to as the *control qubits*, such that a star subgraph can be obtained on S . In Fig. 13 an example of the mapping is presented for a toric code defined on an $N_p = 3$ square lattice, where S is chosen to be a nontrivial loop of $\mathcal{L}_{H,V}^3$ type. We choose a PMS α_c that, throughout the protocol discussed in Sec. III B 1 and Appendix A, keeps the star structure of the graph $G_S^{\alpha_c}$ unchanged. This can be achieved by

- (a) Measuring σ^1 on the control qubits and
- (b) Measuring σ^3 on the rest of the qubits,

which we refer to as the *star measurement setup* (SMS). Note that for a star subgraph $G_S^{\alpha_c}$ is local unitary equivalent to an n -qubit GHZ state, which is a genuinely multiparty entangled state, leading us to the following proposition.

Proposition 3. It is always possible to localize GME on a nontrivial loop of a toric code via single-qubit Pauli measurements on the rest of the system. ■

Computation of FLGME reveals that on the nontrivial loop of the toric code, LGME is bounded from below by $E_S^{\alpha_c} = 1$, as long as the Schmidt measure is used for quantifying GME over S . If GGM is used, $E_S^{\alpha_c} = 1/2$.

In order to determine FLGME under noise, we follow the methodology described in Sec. E 1. We consider the toric code to be subjected to the Markovian and non-Markovian single-qubit Pauli noise discussed in Sec. IV A and investigate the evolution of the FLGME, which we now discuss. We first consider the case of BF noise applied to all qubits in the toric code. Our choice of α_c ensures that $|S_1''| = 0$, further implying that the corresponding FLGME $E_S^{\alpha_c}$ is given by $E_S^{\alpha_c} = E(\varrho_S)$, where ϱ_S is a GD state obtained when the hub of the star subgraph on S in G_{α_c}' is subjected to PD noise, and the rest of the qubits in S are subjected to BF noise.⁷ We also note that the star subgraph on S is equivalent to the N_p -qubit GHZ state via Hadamard operations on the qubits with BF noise, implying that $E(\varrho_S) = E(\varrho_S^{\text{GHZ}})$, ϱ_S^{GHZ} is the mixed state obtained when PD noise is applied to all qubits on the GHZ state. In the case of non-Markovian phase damping noise [82],

$$\varrho_S^{\text{GHZ}} = \frac{1}{2} [(|0\rangle\langle 0|)^{\otimes N_p} + (|1\rangle\langle 1|)^{\otimes N_p} + (1-f)^{N_p} ((|0\rangle\langle 1|)^{\otimes N_p} + (|1\rangle\langle 0|)^{\otimes N_p})], \quad (53)$$

with

$$f = q \left[1 + \epsilon \left(1 - \frac{q}{2} \right) \right]. \quad (54)$$

Using this, the FLGME, as quantified by the genuine multiparty concurrence [102] (see Appendix G) as the GME measure, E , is given by $2 \max[0, \lambda]$ with

$$\lambda = \left| \frac{(1-f)^{N_p}}{2} \right|. \quad (55)$$

⁷This can be seen easily by following the modification of the noise through the protocol described in Sec. III B 1 and Appendix A.

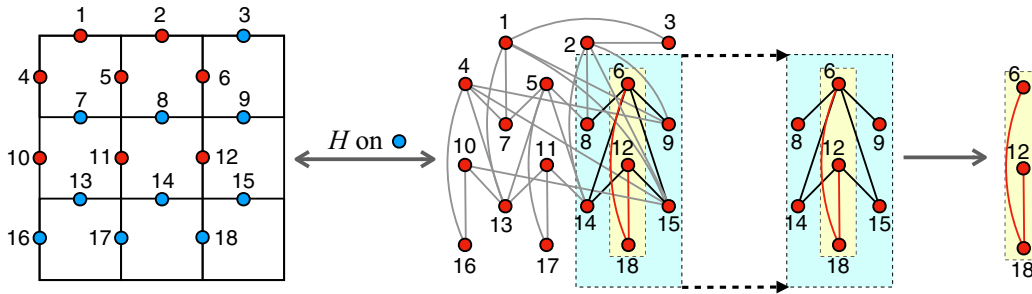


FIG. 13. Transformation of a stabilizer state $|S\rangle$ corresponding to a toric code defined on a $N_p = 3$ square lattice via application of Hadamard operators on the control qubits. The control qubits are denoted by the blue nodes. The chosen subsystem S is a nontrivial vertical loop of size $n = N_p$, on which a star graph can be obtained via a careful choice of the set of control qubits.

It is now straightforward to see that $E(\rho_S^{\text{GHZ}}) = 0$ at a *critical* value of q given by

$$q_c = \frac{1 + \epsilon - \sqrt{1 + \epsilon^2}}{\epsilon}, \quad (56)$$

while for all other values of $0 \leq q < q_c$ and $q_c < q < 1$, $E(\rho_S^{\text{GHZ}}) > 0$ (see Fig. 14). Note also that q_c is independent of the system size N_p . We also perform similar investigations in the case of the PD, BPF, and DP noise. For each of these noise, using the results discussed in Appendix G, we determine the values of q_c beyond which all postmeasured states corresponding to the SMS α_c become biseparable.⁸ In contrast to the BF noise, q_c is found to decrease monotonically with increasing N_p , implying a faster loss of FLGME for larger system. The variations of q_c as a function of the system size N_p , for different values of ϵ , are given in Fig. 15. Note also that for a fixed system size N_p , q_c decreases monotonically with increasing non-Markovianity parameter ϵ .

We now estimate the performance of $E_S^{\alpha_c}$ and $E_S^{\mathcal{P}}$ as lower bounds of E_S . For demonstration, we consider Kitaev's toric code on a square lattice of dimension 2×2 , subjected to single-qubit Pauli noise on all qubits, where E_S and $E_S^{\mathcal{P}}$ as a function of the noise strength q are computed, taking S to be the two-qubit nontrivial loop on the code. In all cases of bit-flip, bit-phase-flip, phase-damping, and depolarizing channels, we find $E_S = E_S^{\mathcal{P}}$ for all noise strengths $0 \leq q \leq 1$ and for all non-Markovianity parameters $0 \leq \epsilon \leq 1$, with examples corresponding to $\epsilon = 1.0$ for different types of noise depicted in Fig. 16. The performance of the bound $E_S^{\alpha_c}$, on the other hand, depends on the judicious choice of α_c , and $E_S^{\mathcal{P}} = E_S^{\alpha_c}$ iff an optimal Pauli measurement setup is chosen as α_c . For the choice of the SMS as α_c , in Fig. 16, we plot $E_S^{\alpha_c}$ as functions of q for $\epsilon = 1.0$. It is clear from the figures that along with the choice of α_c , the performance of $E_S^{\alpha_c}$ as a lower bound of $E_S^{\mathcal{P}}$ depends also on the type of noise as well as noise strength. For example, in the case of the bit-flip noise, $E_S^{\mathcal{P}} = E_S^{\alpha_c}$ for all values of q , while for the bit-phase-flip noise, there exists a range of q over which $E_S^{\mathcal{P}} (= E_S)$ is nonzero, while $E_S^{\alpha_c}$ is not.

⁸For $\epsilon \neq 0$, there may be revival of the FLGME after it decays to zero. In such cases, we consider q_c to be the first instance at which FLGME vanishes. For example, see 2×2 toric code under non-Markovian PD noise [Fig. 16(c)].

We point out here that the protocol discussed in Sec. III B 1 and Appendix A and the methodology for obtaining a lower bound of localizable entanglement in the presence of noise works as long as a suitable α_c can be constructed. For example, one may also aim to compute the lower bound for the localizable bipartite entanglement over a specific bipartition AB of the subsystem S . We demonstrate this by computing a lower bound $E_{A:B}^{\alpha_c}$ of the localizable bipartite entanglement between two nontrivial loops in the toric code, where the two loops combined form the subsystem S . The appropriate PMS α_c used for this calculation is discussed in Appendix H, while negativity [103–108] (see Appendix G) is used as the bipartite entanglement measure E . Variations of $E_{A:B}^{\alpha_c}$ as a function of q are depicted for an $N_p = 6$ square lattice, and for increasing distances between the two chosen nontrivial loops of the $\mathcal{L}_{H,V}^3$ type in Fig. 17. Note that with increasing distance, $E_{A:B}^{\alpha_c}$ between two nontrivial loops decreases when q is fixed.

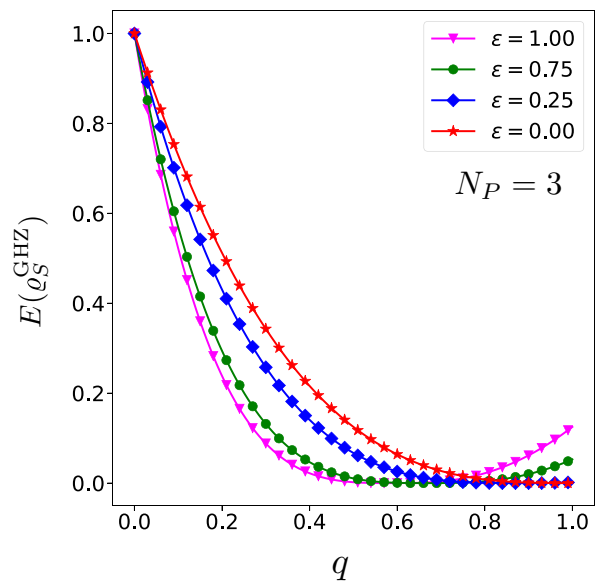


FIG. 14. Variations of $E(\rho_S^{\text{GHZ}})$ as a function of q in the case of the BF noise applied to all qubits in a toric code defined on a $N_p = 3$ square lattice, where S is a nontrivial loop representing $\mathcal{L}_{H,V}^3$, and the non-Markovianity parameter ϵ takes values $\epsilon = 0, 0.25, 0.75$, and 1. Genuine multiparty concurrence is chosen as the entanglement measure. All the axes in all figures are dimensionless.

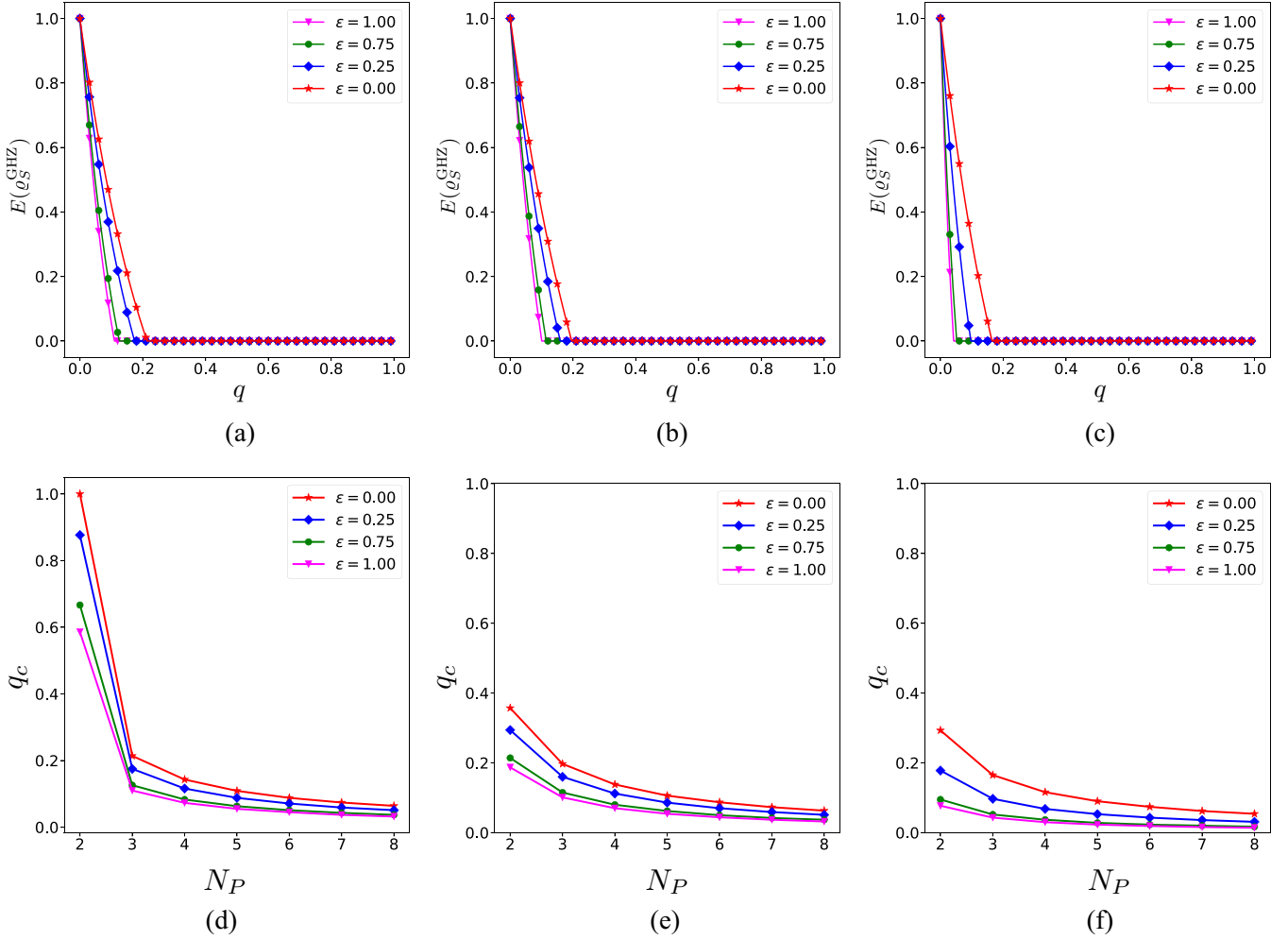


FIG. 15. In (a)–(c) we depict variations of $E(\rho_S^{\text{GHZ}})$ as a function of q in the case of (a) PD, (b) BPF, and (c) DP noise, applied to all qubits in a toric code defined on a $N_P = 3$ square lattice, where S is a nontrivial loop representing $\mathcal{L}_{H,V}^3$, and the non-Markovianity parameter ϵ takes values $\epsilon = 0, 0.25, 0.75$, and 1 . Genuine multiparty concurrence is chosen as the entanglement measure. In (d)–(f) we show variations of q_c as a function of N_P in the case of the (d) PD, (e) BPF, and (f) DP noise, for a nontrivial loop of a toric code defined on a $N_P \times N_P$ square lattice, for $\epsilon = 0, 0.25, 0.75$, and 1 . In all figures, $\epsilon = 0$ stands for the case of Markovian noise. All the axes in all figures are dimensionless.

VI. CONCLUSION AND OUTLOOK

In this paper we investigate LGME on subsystems of arbitrary large stabilizer states in noiseless and noisy scenarios. We demonstrate the calculation of lower bounds of LGME for pure stabilizer states using multiqubit graph states as their representatives, and adopting a graph-based technique for performing single-qubit Pauli measurements on graphs. We also show that the calculation of a lower bound of LGME using the graphical technique has a polynomial scaling with the system size. We calculate LGME over subsystems of linear, ladder, and square graphs of arbitrary sizes. We further expand the calculation in the case of arbitrary graph states in the presence of single-qubit Pauli noise of Markovian and non-Markovian types. Using the linear, ladder, and square graphs of arbitrary sizes as examples, we demonstrate the existence of a critical noise strength corresponding to a lower bound of LGME for a specific Pauli measurement setup, beyond which all postmeasured states corresponding to the chosen measurement setup become biseparable. The results for the

graph states can be translated directly to arbitrary stabilizer states due to their local unitary connection with graph states. We demonstrate this by considering the stabilizer state corresponding to a toric code defined on a square lattice. We also provide a specific Pauli measurement setup to determine a lower bound of the localizable bipartite entanglement between two nontrivial loops situated a distance apart in the code.

We conclude with a brief overview of the future research directions arising out of this paper. The graph-based methodology for computing appropriate lower bounds of LGME over chosen subsystems of arbitrary stabilizer states opens up the possibility of thoroughly studying and characterizing LGME on subsystems of topological quantum codes, including the toric code [92,93] and the color code [109,110] in the absence and presence of naturally occurring local Pauli noise in experiments [111,112]. It also provides avenues to explore localizable bipartite entanglement between two nontrivial loops representing different logical operators in the codes and provides the motivation to look for appropriate witness operators

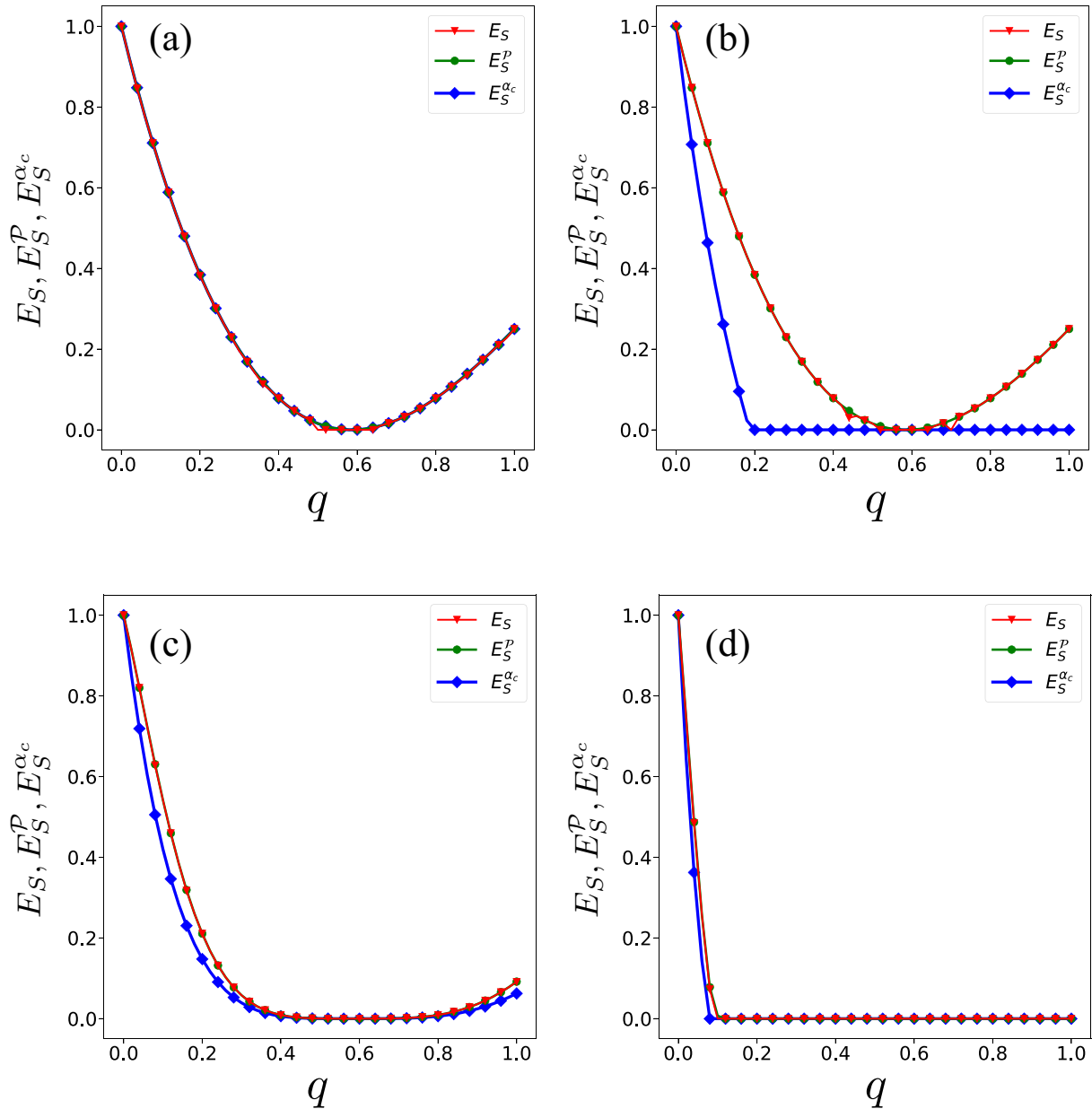


FIG. 16. Variations of E_S , E_S^P , and $E_S^{\alpha c}$ as a function of q in the case of the stabilizer state corresponding to a 2×2 ($N_P = 2$) toric code subjected to (a) BF, (b) BPF, (c) PD, and (d) DP channels on all qubits with $\epsilon = 1.0$. All quantities plotted are dimensionless.

to construct witness-based lower bounds of LGME, in the same vein as in [70,71]. Moreover, our paper provides a way of characterizing parts of a large quantum network built out of stabilizer states [113].

In view of the importance of devising methodologies that are applicable in noisy intermediate-scale quantum (NISQ) devices [114], which are ideal test beds for dynamics of open quantum systems, we point out that determination of LGME using our proposed methodology requires (1) Pauli measurements on subsets of qubits in a multiqubit system and (2) determination of entanglement of a quantum state postmeasurement. Regarding the former, measuring Pauli operators in NISQ devices is possible and is studied extensively (see [114] and the references therein). With respect to the latter, we point out that while we focus on genuine multipartite

entanglement measures, one can also perform a similar study with other types of entanglement, e.g., bipartite entanglement. This requires detecting and quantifying entanglement of arbitrary states in NISQ devices, which has been an active area of research in recent times. Specific algorithms towards this goal already exist using the positive map criterion [115], for computing a tangle [116] for three-qubit systems, and for computing the entanglement spectrum [117,118]. Moreover, we point out here that the localizable entanglement can be connected to entanglement witness operators [70,71,77], the expectation value of which, computed in the postmeasured states, can provide a lower bound of localizable entanglement: bipartite or multipartite. In the case of stabilizer states, these witness operators are typically designed with stabilizer operators, which are constituted of Pauli matrices, and whose

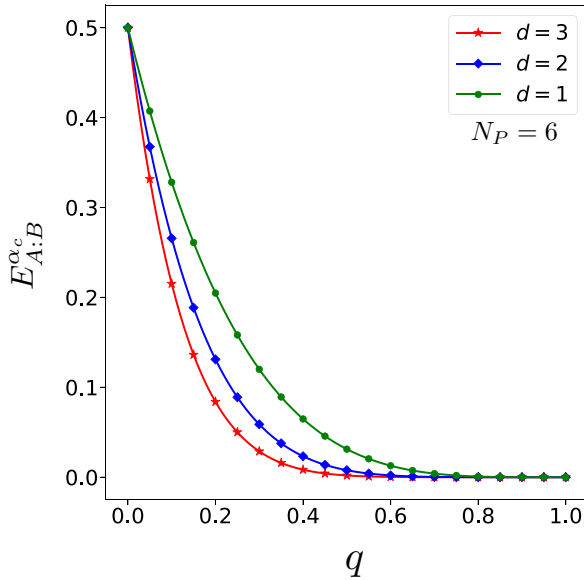


FIG. 17. Variations of $E_{A:B}^{\alpha_c}$ as a function of q in the case of the BF noise applied to all qubits in a toric code defined on a $N_P = 6$ square lattice for various distances, d , between the nontrivial loops. Both axes in the figure are dimensionless. See Appendix H for the description of α_c .

expectation values can be accessed in NISQ devices ([119]; see also [114] and references therein). Therefore, our methodology can potentially be applied to NISQ devices also, while the specific algorithm remains to be worked out.

ACKNOWLEDGMENTS

We acknowledge the support from the Science and Engineering Research Board (SERB), India, through the Start-Up Research Grant (SRG) (File No. SRG/2020/000468, 11 November 2020), and the use of QIClib [120], a modern C++ library for general purpose quantum information processing and quantum computing.

APPENDIX A: OPERATIONS ON GRAPH

In this Appendix we discuss a number of graph operations and the related local unitary operations on the corresponding graph states. In order to distinguish between different unitary operations on a specific node of a graph, we provide different attributes, a , to each node. We particularly focus on the unitary operations $\{\sigma^3, H, R = \sqrt{\sigma^3}\}$, where the node attributes corresponding to different combinations of these unitary operations are shown in Fig. 18. The importance of these unitaries is discussed in Sec. III B 1. Note that the attributes depicted in Fig. 18 can be considered to be different combinations of three basic binary attributes: (a) shape (s) [circle (c), or diamond (d)], (b) fill (f) [red (r), or white (w)], and (c) sign (sg) [plus (+) or minus (-), where we represent the plus sign by the absence of the sign to keep the figures uncluttered]. At the graph level, we often describe the operations in terms of changing one or more of these attributes, while each such operation corresponds to a local unitary operation on the corresponding graph state.

Attributes								
Numbers	1	2	3	4	5	6	7	8

FIG. 18. Attributes for the nodes of a graph according to the application of (1) I_i , (2) σ_i^3 , (3) H_i , (4) $H_i\sigma_i^3$, (5) R_i , (6) $R_i\sigma_i^3$, (7) H_iR_i , and (8) $H_iR_i\sigma_i^3$ on a node in the graph. We denote the different attributes by the corresponding numbers in the text.

a. Local complementation. Local complementation [43,61,121–123] of a connected graph G w.r.t. a node $i \in G$ is a simple local graph operation, performed by deleting (creating) all the links (j, k) between the nodes j and $k \in \mathcal{N}_i$, if (j, k) is present (absent) in the graph. Here \mathcal{N}_i is the neighborhood of the node i , constituted of all the nodes in the graph that are connected to the node i via a link. An example of the local complementation operation is demonstrated in Fig. 19(a) for a graph with five nodes. Let $G' = \mathcal{O}_i(G)$ represents the graph resulting from the local complementation on the node i in G . The corresponding graph states, $|G'\rangle$ and

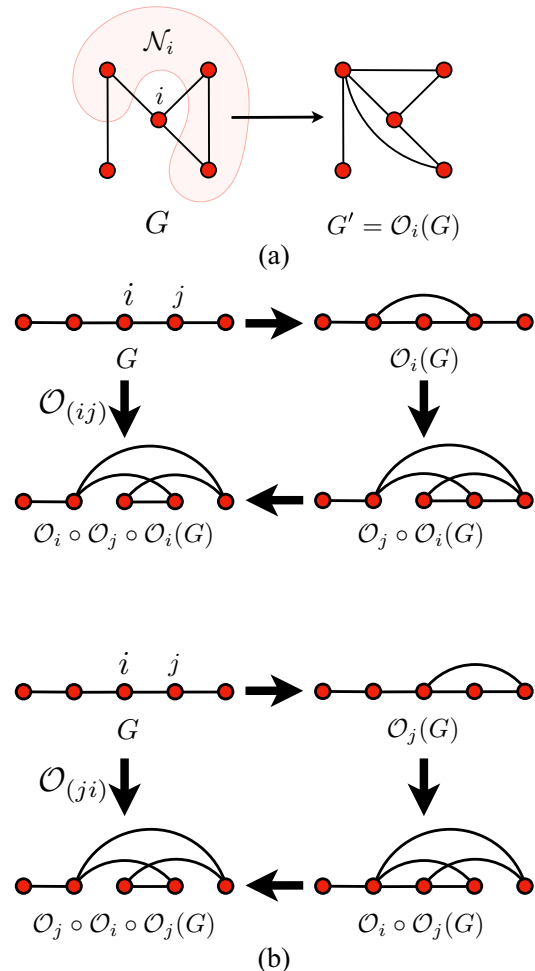


FIG. 19. (a) Local complementation operation on the graph G w.r.t. the node i . The shaded region contains the nodes that constitute the neighborhood \mathcal{N}_i of the node i . (b) Equivalence of \mathcal{O}_{ij} and \mathcal{O}_{ji} demonstrated on a linear graph of five nodes.

$$\mathcal{F}_i^c(\bullet) = \blacklozenge, \mathcal{F}_i^d(\blacklozenge) = \bullet, \mathcal{F}_i^c(\circ) = \blacklozenge, \mathcal{F}_i^d(\blacklozenge) = \circ,$$

$$\mathcal{F}_i^c(\bullet) = \blacklozenge, \mathcal{F}_i^d(\blacklozenge) = \bullet, \mathcal{F}_i^c(\ominus) = \blacklozenge, \mathcal{F}_i^d(\blacklozenge) = \ominus.$$

Flipping the shape

$$\mathcal{F}_i^r(\bullet) = \circ, \mathcal{F}_i^w(\circ) = \bullet, \mathcal{F}_i^r(\blacklozenge) = \blacklozenge, \mathcal{F}_i^w(\blacklozenge) = \bullet,$$

$$\mathcal{F}_i^r(\bullet) = \ominus, \mathcal{F}_i^r(\blacklozenge) = \blacklozenge, \mathcal{F}_i^w(\ominus) = \bullet, \mathcal{F}_i^w(\blacklozenge) = \blacklozenge.$$

Flipping the fill

$$\mathcal{F}_i^+(\bullet) = \bullet, \mathcal{F}_i^+(\blacklozenge) = \blacklozenge, \mathcal{F}_i^+(\blacklozenge) = \blacklozenge, \mathcal{F}_i^+(\circ) = \ominus,$$

$$\mathcal{F}_i^-(\bullet) = \bullet, \mathcal{F}_i^-(\blacklozenge) = \blacklozenge, \mathcal{F}_i^-(\ominus) = \circ, \mathcal{F}_i^-(\blacklozenge) = \blacklozenge.$$

Flipping the sign

$$\mathcal{R}_i^c(\bullet) = \blacklozenge, \mathcal{R}_i^c(\bullet) = \blacklozenge, \mathcal{R}_i^c(\circ) = \blacklozenge, \mathcal{R}_i^c(\ominus) = \blacklozenge.$$

Reshaping a circular node

$$\mathcal{R}_i^d(\blacklozenge) = \bullet, \mathcal{R}_i^d(\blacklozenge) = \ominus, \mathcal{R}_i^d(\blacklozenge) = \circ, \mathcal{R}_i^d(\blacklozenge) = \bullet.$$

Reshaping a diamond node

FIG. 20. Flip and reshape operations on the node attributes.

$|G\rangle$, are connected by an LC operation on the node i and its neighboring nodes, as [61] $|G'\rangle = U_{LC}^i |G\rangle$, with

$$U_{LC}^i = e^{-i\frac{\pi}{4}\sigma_i^1} \otimes_{j \in \mathcal{N}_i} e^{i\frac{\pi}{4}\sigma_j^3}. \quad (\text{A1})$$

b. Local complementation along an edge. Local complementation along an edge $(i, j) \in G$ is a sequence of three local complementations on G w.r.t the nodes i and j , given by $\mathcal{O}_{(ij)} = \mathcal{O}_i \circ \mathcal{O}_j \circ \mathcal{O}_i$, where $\mathcal{O}_j \circ \mathcal{O}_i(G) = \mathcal{O}_j(\mathcal{O}_i(G))$. Local complementation along an edge is symmetric with an interchange of i with j , i.e., $\mathcal{O}_{(ij)} \equiv \mathcal{O}_{(ji)}$. This is demonstrated in Fig. 19(b) in the case of a linear graph with five nodes. Evidently, local complementation along an edge represents a local unitary operation on the corresponding graph state, which is constituted by the unitaries of the form U_{LC}^i , as given in Eq. (A1).

c. Flip. The flip operation \mathcal{F}_i^a on the node i in G reverses one of the binary attributes, shape, fill, and sign of the node, where the superscript a in \mathcal{F}_i^a represents the value of the flipped binary attribute, with $a = s, f, sg$. The flip operations are consolidated in Fig. 20.

d. Reshape. Reshaping is an operation that is specific to the shape attribute of a node. We denote this operation by \mathcal{R}_i^s , where the superscript s is the shape attribute of the node prior to applying \mathcal{R}_i^s , on which the action of \mathcal{R}_i^s depends. If the shape of a node is a circle, then \mathcal{R}_i^c results in only a *flip of the shape* that changes the shape attribute from circle to diamond, i.e., $\mathcal{R}_i^c \equiv \mathcal{F}_i^c$. On the other hand, if the shape of a node is a diamond, then \mathcal{R}_i^d is equivalent to (a) a *flip of the shape* that changes the shape attribute from diamond to circle, and (b) a *flip of the sign* from $+$ ($-$) to $-$ ($+$). These rules are also consolidated in Fig. 20.

1. Obtaining the reduced graph

We now discuss the graph transformation $G \rightarrow G'_\alpha$ for a specific choice of the PMS α , which is a key ingredient of the protocol for computing E_S^P over an arbitrary S in an arbitrary G , as discussed in Sec. III B 1. Starting from ρ corresponding to an arbitrary graph G , we achieve this in two steps, Step A and Step B. In Step A we graphically represent the state $\rho_\alpha = \mathbf{U}_\alpha^\dagger \rho \mathbf{U}_\alpha$ [see Eq. (22)]. Next, we perform Step B to obtain the graphical representation of the state $\rho'_\alpha = \mathbf{V}_\alpha |G'_\alpha\rangle \langle G'_\alpha| \mathbf{V}_\alpha^\dagger$, from which the graph G'_α can be straightforwardly extracted.

Step A. As stated in Sec. III B 1, we are specifically interested in the single-qubit unitary operations $\{\sigma_i^3, H_i, R_i\}$ on the qubit i . Based on the graph operations described above, these unitaries can be represented as follows [84,85].

A.1 H_i on any node: \mathcal{F}_i^f ($\mathcal{F}_i^r(G)$ or $\mathcal{F}_i^w(G)$, depending on whether $f = r$ or w for the node i).

A.2 R_i on a node with $f = r$: \mathcal{R}_i^s [$\mathcal{R}_i^c(G)$ or $\mathcal{R}_i^d(G)$, depending on whether $s = c$ or d for the node i].

A.3 R_i on a node with $f = w, s = c, sg = +$: $\mathcal{R}_{\mathcal{N}_i}^s \circ \mathcal{O}_i$, where $\mathcal{R}_{\mathcal{N}_i}^s$ represents \mathcal{R}_j^s operations on all nodes $j \in \mathcal{N}_i$.

A.4 R_i on a node with $f = w, s = c, sg = -$: $\mathcal{F}_{\mathcal{N}_i}^{sg} \circ \mathcal{R}_{\mathcal{N}_i}^s \circ \mathcal{O}_i$, where $\mathcal{R}_{\mathcal{N}_i}^s$ represents \mathcal{R}_j^s operations on all nodes $j \in \mathcal{N}_i$, and $\mathcal{F}_{\mathcal{N}_i}^{sg}$ stands for $\mathcal{F}_j^{sg} \forall j \in \mathcal{N}_i$.

A.5 R_i on a node with $f = w, s = d, sg = +$: $\mathcal{F}_{\mathcal{N}_i}^{sg} \circ \mathcal{R}_{\mathcal{N}_i}^s \circ \mathcal{O}_i \circ \mathcal{F}_i^d \circ \mathcal{F}_i^w$ where $\mathcal{F}_{\mathcal{N}_i}^{sg}, \mathcal{R}_{\mathcal{N}_i}^s$ denotes flip and reshape operations, respectively, on the entire neighborhood of the node.

A.6 R_i on a node with $f = w, s = d, sg = -$: $\mathcal{R}_{\mathcal{N}_i}^s \circ \mathcal{O}_i \circ \mathcal{F}_i^d \circ \mathcal{F}_i^w$

A.7 σ_i^3 on a node with $f = r$: \mathcal{F}_i^{sg} [$\mathcal{R}_i^+(G)$ or $\mathcal{R}_i^-(G)$, depending on whether $sg = \pm$ for the node i]

A.8 σ_i^3 on a node with $f = w, s = c$: $\mathcal{F}_{\mathcal{N}_i}^{sg}$. Where $\mathcal{F}_{\mathcal{N}_i}^{sg}$ denotes flip of sign on all neighborhood nodes.

A.9 σ_i^3 on a node with $f = w, s = d$: $\mathcal{F}_i^{sg} \circ \mathcal{F}_{\mathcal{N}_i}^{sg}$

For ease of representation, we denote the graph operations corresponding to the rules A.1, ..., A.9 as $\mathcal{A}_1, \dots, \mathcal{A}_9$, where, for example, $\mathcal{A}_3 \equiv \mathcal{R}_{\mathcal{N}_i}^s \circ \mathcal{O}_i$. Note that a subset of the transformations $\{\mathcal{A}_1, \dots, \mathcal{A}_9\}$ according to a specific unitary operator \mathbf{U}_α corresponding to a specific PMS α provides a graphical representation of the state ρ_α [see Eq. (22) and the corresponding discussion].

Step B. To achieve this step, we additionally use two graph transformations, referred to as the *equivalence transformations*, that correspond to Eq. (23) in Sec. III B 1. These graph transformations, denoted by \mathcal{B}_1 and \mathcal{B}_2 , are described below:

B.1 The graph operations constituting \mathcal{B}_1 on a node i with $s = d$ are as follows, in the specified order: (1) flip the fill of the node i , (2) perform local complementation on the node i , (3) reshape the neighbors of the node i in the transformed graph, (4) flip the sign of the node i , and (5) if $sg = -$ for the node i in the resulting graph, then flip the signs of the neighbors of the node i in the transformed graph also.

B.2 The graph operations constituting \mathcal{B}_2 on a link $(i, j) \in G$, such that both i and j have $s = c$, are as follows, in the specified order: (1) flip the fills of the nodes i and j , (2) perform a local complementation along the edge (i, j) , (3) flip the signs of the nodes that are connected to both of i and j in the transformed graph, and (4) if either of the nodes i and j in

the transformed graph has $sg = -$, flip the sign of that node as well as the signs of its neighbors in the transformed graph.

We now present the algorithm for obtaining G'_α in the form of a pseudocode, using the above equivalence transformations.

input (1) The graphical representation of ρ_α , as obtained from Step A, with nodes of eight different attributes and the links, and (2) sets S' and S of measured and unmeasured nodes:

1. Obtain the set \mathcal{D}_{dw} of all nodes with $s = d$, $f = w$ (i.e., type 7 and type 8 nodes; see Fig. 18), and the set \mathcal{L}_{cw} of all pairs (i, j) of nodes with $s = c$, $f = w$ [i.e., (type 3, type 3), (type 3, type 4), (type 4, type 3), and (type 4, type 4) links], such that the link (i, j) exists. The sizes of these sets are given by $|\mathcal{D}_{dw}|$ and $|\mathcal{L}_{cw}|$, respectively.
 - (a) **while** $|\mathcal{L}_{cw}| > 0$ or $|\mathcal{D}_{dw}| > 0$, **do**
 - (I) operate \mathcal{B}_1 on all nodes $i \in \mathcal{D}_{dw}$
 - (II) operate \mathcal{B}_2 on all $(i, j) \in \mathcal{L}_{cw}$
 - (b) determine $|\mathcal{L}_{cw}|$, $|\mathcal{D}_{dw}|$.
 - (c) **if** $|\mathcal{L}_{cw}| > 0$ or $|\mathcal{D}_{dw}| > 0$, **repeat** (a)–(c).

else exit
2. Obtain the set \mathcal{E}_B of all boundary links (i, j) having node $i \in S'$, and node $j \in S$, such that i is either of type 3, type 4 nodes (see Fig. 18). Let us denote the set of these nodes $i \in S'$ as \mathcal{N}_S .
 - (a) **for** all $(i, j) \in \mathcal{E}_B$ such that $i \in \mathcal{N}_S$, **do**
 - (I) **if** j has $s = c$, apply \mathcal{B}_2 on (i, j)

else first apply \mathcal{B}_1 to node j , and then to node i
3. Extract the unitary operation \mathbf{V} from the node attributes
4. Replace all nodes by type 1 nodes (see Fig. 18) converting it to a normal graph, and extract the connectivity of G'_α .

output (1) The reduced graph G'_α and (2) the unitary \mathbf{V} in terms of the set of unitaries $\{V_i, i \in G'_\alpha\}$.

Implementation of the algorithm presented in the pseudocode up to step 2 ensures the following for ρ'_α .

(a) The neighborhood S'_1 of S has at least one node, and the nodes in S'_1 can be only of the types 1, 2, 5, or 6 (see Fig. 18), so that σ^3 measurement on these nodes remain unchanged.

(b) The nodes in S'_2 , in addition to being of the types 1, 2, 5, or 6, can also be of the types 3 or 4 (see Fig. 18). This ensures that only σ^3 and σ^1 measurements are allowed in S'_2 .

(c) If a type 3 node, or a type 4 node occurs in S'_2 , then its neighborhood will be constituted of types 1, 2, 5, and 6 nodes only.

Because of these characteristics of ρ'_α , it is always possible to fully disconnect types 3 and 4 nodes of S'_2 by measuring σ^3 only on the nodes of types 1, 2, 5, and 6. Note that when σ^3 is measured on a node $i \in \{\text{type 1, type 2, type 5, type 6}\}$, the outcomes ± 1 are equiprobable, and the graph postmeasurement can be obtained by

- (1) Deleting all the edges between the node i and its neighbors \mathcal{N}_i
- (2) Replacing the node i with type 3 (type 4) node if the outcome is $+1$ (-1) and
- (3) Performing $\mathcal{F}_{\mathcal{N}_i}^{sg}$ if the outcome is -1 .

If one now measures σ^3 on a node $i \in \{\text{type 3, type 4}\}$ belonging to S'_2 , due to the absence of a connection between the node and the rest of the graph, the measurement leaves the graph unaltered, and the measurement outcome is $+1$ (-1) for the node of type 3 (type 4) with certainty. See Fig. 21 for an example of the construction of reduced graph using above prescription.

2. Scaling with system size

We now explore how the protocol discussed in Sec. III B 1 and Appendix A scales with the number of measured nodes $|S'| = N - n = m$ in a graph G , which is given by the dependence of the total number of graph operations, C , performed during the protocol on m . Since the graph G changes during each step of the protocol, it is in general difficult to obtain the exact dependence of C on m . However, to estimate an upper bound, C' , of C , consider a fully connected graph of size N , where σ^2 measurement⁹ on m nodes is performed so that a maximum number of graph operations in terms of flipping of the node attributes and creation or deletion of the links in local complementations have to be performed. The measurement transformation $\sigma^2 \rightarrow \sigma^3$ in Step A on m nodes corresponds to $2m$ graph operations. On the other hand, the number of graph operations during the reduction in Step B is upper bounded by m iteration of \mathcal{B}_1 , each of which requires at most $N^2 - N + 4$ graph operations. Therefore, the dependence of C on m is overall upper bounded by

$$C' = m(N^2 - N + 6). \quad (\text{A2})$$

In the limit $N \approx m^{10}$

$$C' = m^3 - m^2 + 6m, \quad (\text{A3})$$

which is a polynomial dependence on m .

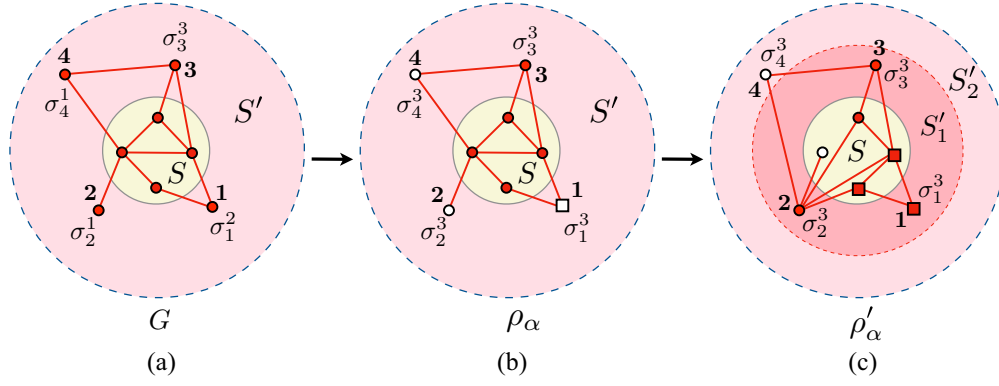
In order to test this estimate, in Fig. 22, we present the numerical data for the variation of C with m , for cubic, square, and linear graphs states on $N = 8^3 = 343$, $N = 18^2 = 324$, and $N = 325$ nodes, respectively. We randomly choose n nodes from the graph and perform σ^2 measurement on $m = N - n$ nodes, followed by a calculation of C . We see that the numerical data are always upper bounded by C' , as per our estimation. Note here that the actual values of the total graph operations depend on the structure of the chosen graph, as expected.

APPENDIX B: PROOF OF PROPOSITION 1

Proof. For reasons that will be clear shortly, we relabel the measurement outcomes corresponding to qubits in S'_1 (S'_2) by l (m), such that $l_j = k_j$ ($m_j = k_j$) if $j \in S'_1$ (S'_2). We can therefore regroup the outcome index k as $k \equiv lm$ with $l \equiv l_1 l_2 \dots l_L$, and $m \equiv m_{L+1} m_{L+2} \dots m_N$, where we have assumed, without any loss in generality, that L is the size of S'_1 such that S'_2 has $N - n - L$ qubits. In this notation $M_k^\alpha \equiv M_{lm}^\alpha$,

⁹This is the costliest Pauli measurement in terms of graph operations. See Appendix A.

¹⁰This is typically the case when the actual system is large enough compared to the subsystem on which entanglement is localized.


 FIG. 21. Transformation of the graph $G \rightarrow G_R$ shown in Fig. 1 in the graphical representation described in Appendix A.

and using Eq. (23) in Eq. (21), we obtain

$$\begin{aligned} \varrho_k &= \mathbf{U}_\alpha M_{lm}^\alpha \rho_\alpha M_{lm}^{\alpha\dagger} \mathbf{U}_\alpha^\dagger \\ &= \mathbf{U}_\alpha \mathbf{V}_\alpha M_{lm}^\alpha |G'_\alpha\rangle \langle G'_\alpha| M_{lm}^{\alpha\dagger} \mathbf{V}_\alpha^\dagger \mathbf{U}_\alpha^\dagger, \end{aligned} \quad (\text{B1})$$

with $M_{lm}^\alpha \leftarrow \mathbf{V}_\alpha^\dagger M_{lm}^\alpha \mathbf{V}_\alpha$, such that after this transformation, $\alpha_j = 3$ only $\forall j \in S'_1$. Note that \mathbf{V}_α can change only the measurement basis, not the measurement outcome. The graph transformation algorithm discussed in Appendix A ensures that the measurement on any of the qubits in S'_2 can be either a σ^3 , or a σ^1 , i.e., $\alpha_j = 1, 3$ if $j \in S'_2$. Now, application of M_{lm}^α on the graph state $|G'_\alpha\rangle$ results in the normalized state of the form

$$\begin{aligned} M_{lm}^\alpha |G'_\alpha\rangle \langle G'_\alpha| M_{lm}^{\alpha\dagger} &= \mathbf{W}_{lm} [(\otimes_{j \in S'_1} |l_j\rangle \langle l_j|) \otimes (\otimes_{j \in S'_2} |m_j\rangle \langle m_j|) \\ &\quad \otimes (|G_S^\alpha\rangle \langle G_S^\alpha|)] \mathbf{W}_{lm}^\dagger, \end{aligned} \quad (\text{B2})$$

where G_S^α is the subgraph on S in G''_α , which is obtained by performing the graph transformations corresponding to the

single-qubit Pauli measurements on the graph G'_α for all qubits in S' . These transformations, for a measurement on a single qubit, are given by [43,48]

$$\sigma_j^1 : G'_\alpha \rightarrow \mathcal{O}_a(\mathcal{O}_j(\mathcal{O}_a(G'_\alpha)) \setminus j), \quad (\text{B3})$$

$$\sigma_j^3 : G'_\alpha \rightarrow G'_\alpha \setminus j, \quad (\text{B4})$$

with a being any node in the neighborhood \mathcal{N}_j of the node $j \in G'_\alpha$, and $G'_\alpha \setminus j$ is obtained from G'_α by deleting all links connected to the node j . The graph operation $\mathcal{O}_j(G)$ w.r.t. a node j represents a *local complementation* [43,61,121–123] operation (see also Appendix A for the definition). These single-qubit Pauli measurements on all $j \in S'$ also result in Clifford unitary operators operating postmeasurement on the qubits constituting the graph, leading to the unitary operations \mathbf{W}_{lm} , given by [43,48]

$$\mathbf{W}_{lm} = (\otimes_{j \in S'_1} W_{l_j}^3) (\otimes_{j \in S'_2} W_{m_j}^{1,3}), \quad (\text{B5})$$

where for each j ,

$$W_{+1}^1 = e^{i\frac{\pi}{4}\sigma_a^2} \otimes_{b \in \mathcal{N}_j \setminus (\mathcal{N}_a \cup a)} \sigma_b^3, \quad (\text{B6})$$

$$W_{-1}^1 = e^{-i\frac{\pi}{4}\sigma_a^2} \otimes_{b \in \mathcal{N}_a \setminus (\mathcal{N}_j \cup j)} \sigma_b^3, \quad (\text{B7})$$

$$W_{+1}^3 = I_j, \quad (\text{B8})$$

$$W_{-1}^3 = \otimes_{b \in \mathcal{N}_j} \sigma_b^3, \quad (\text{B9})$$

with a being chosen as in Eq. (B3).

It is worthwhile to point out here that Eqs. (B3)–(B4) indicate that G''_α and consequently G_S^α is independent of the measurement outcomes l and m . Using (B2) in Eq. (B1), and tracing out the subsystem S' , we obtain

$$\varrho_S^k = \mathbf{V}_{S,\alpha} \mathbf{W}_{S,l} |G_S^\alpha\rangle \langle G_S^\alpha| \mathbf{W}_{S,l}^\dagger \mathbf{V}_{S,\alpha}^\dagger, \quad (\text{B10})$$

where the subscript S is introduced in the unitary operators to signify the components of the unitaries that have support only on S , and we have dropped the index m from \mathbf{W}_S as the components of \mathbf{W} on S are governed only by l . Therefore,

$$E(\varrho_S^k) = E(|G_S^\alpha\rangle \langle G_S^\alpha|), \quad (\text{B11})$$

which is independent of the measurement outcomes l and m . This proves Proposition 1. \blacksquare

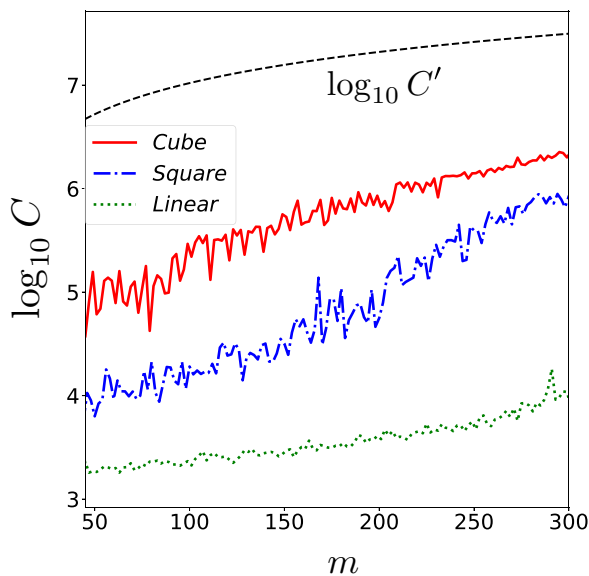


FIG. 22. Variation of the total number of graph operations with the number of measured nodes, m , in cubic, square, and linear graphs on respectively $N = 343$, 324 , and 325 nodes. To draw the variation of the analytically estimated upper bound, C' , we use $N = 324$.

APPENDIX C: ENTANGLEMENT IN PURE GRAPH STATES

Here we discuss quantification and characterization of bipartite and multipartite entanglement in graph states.

1. Bipartite entanglement

Let us consider a system of qubits $V \equiv \{1, 2, \dots, N\}$ forming a *connected graph* G . Let us now consider a bipartition of the system V as $A \cup B = V$ and $A \cap B = \emptyset$, where $d_A = \dim(\mathcal{H}_A)$ ($d_B = \mathcal{H}_B$), \mathcal{H}_A (\mathcal{H}_B) are the Hilbert space associated with A (B). For each pure state $|G\rangle$ in $\mathcal{H}_A \otimes \mathcal{H}_B$, orthonormal basis $\{b_A^i\} \in \mathcal{H}_A$ and $\{b_B^j\} \in \mathcal{H}_B$ exist such that in Schmidt decomposed form,

$$|G\rangle = \sum_{i=1}^d \sqrt{\lambda_i} |b_A^i b_B^i\rangle, \quad (\text{C1})$$

with $d = \min\{d_A, d_B\}$, and nonnegative Schmidt coefficients $\sqrt{\lambda_i}$ with $\lambda_i \geq 0$ and $\sum_{i=1}^d \lambda_i = 1$. The marginals of $|G\rangle$, given by

$$\begin{aligned} \rho_{A(B)} &= \text{Tr}_{B(A)}[|G\rangle\langle G|] \\ &= \sum_{i=1}^d \lambda_i |b_{A(B)}^i\rangle\langle b_{A(B)}^i|, \end{aligned} \quad (\text{C2})$$

have the spectrum $\{\lambda_i; i = 1, \dots, d\}$. The state $|G\rangle$ is *maximally entangled* (ME) [1,2] in the bipartition $A : B$ if $\lambda_i = 1/d \forall i$, which corresponds to the marginal of the subsystem of dimension d to be maximally mixed, i.e., I/d , where I is the identity matrix on the Hilbert space of dimension d . Otherwise, $|G\rangle$ is *nonmaximally entangled* (NME) in the partition $A : B$. In situations where $|G\rangle$ is maximally entangled across any bipartition (see also [124,125]), they are referred to as the *absolutely maximally entangled* (AME) states [126–130]. To compute the bipartite entanglement $E_{A:B}(G)$ between the partitions A and B of G , one needs to compute the marginals $\rho_{A(B)}$ for $|G\rangle$, which can be obtained in terms of the generators $\tilde{g}_i^{A(B)}$ as [43,48]

$$\rho_{A(B)} = \frac{1}{d_{A(B)}} \sum_{\{\tilde{g}_i^{A(B)}\}} \tilde{g}_i^{A(B)}, \quad (\text{C3})$$

where

$$\{\tilde{g}_i^{A(B)}\} = \{g_i | \text{supp}(g_i) \in A(B)\}, \quad (\text{C4})$$

i.e., $\{\tilde{g}_i^{A(B)}\}$ is the subset of $\{g_i\}$ with support on $i \in A(B)$. For an arbitrary connected graph G , the single-qubit marginals corresponding to all qubits are maximally mixed [43,99], implying $|G\rangle$ is ME in all bipartitions of a qubit and the rest. Also, note that for $N = 2, 3$, $d = 2$ [see Eq. (C1)], and $|G\rangle$ is AME. On the other hand, in case of G with arbitrary $N > 3$, and assuming A to be the smaller subsystem constituted of two qubits $\{i, j\} \in G$ (i.e., $d = 4$), $\rho_A = \rho_{ij}$ is either maximally mixed, or a rank-2 mixed state [43]. In the case of the former, $|G\rangle$ is ME in the bipartition $A : B$, whereas in the case of the latter, it is not.

Note that it is sufficient to investigate connected graphs. In the case of graphs that are not connected, the bipartite entanglement present in the graph will be decided by the bipartite

entanglement present in the graph states corresponding to the connected segments of the full graph.

2. Multipartite entanglement

We now discuss the multipartite entanglement in graph states. A multiqubit quantum state is genuinely multipartite entangled if it is not separable in any possible bipartition. Connected pure graph states are known to be genuinely multipartite entangled [48], where the degree of entanglement can be quantified using the *Schmidt measure* [43,48] and the generalized geometric measure [83,97].

a. Schmidt measure

A pure state of N qubits can be written as

$$|\psi\rangle = \sum_{i=1}^R c_i |\psi_i^{(1)}\rangle \otimes \dots \otimes |\psi_i^{(N)}\rangle, \quad (\text{C5})$$

where c_i s are complex numbers subject to normalization $\sum_i |c_i|^2 = 1$, $|\psi_i^{(l)}\rangle$ belongs to the Hilbert space of the qubit l , $l = 1, 2, \dots, N$, and R is an integer $< 2^N$. The Schmidt measure of $|\psi\rangle$ is given by [48,131]

$$E(|\psi\rangle\langle\psi|) = \log_2(r), \quad (\text{C6})$$

where r is the minimum possible value of R over all possible linear decompositions of $|\psi\rangle$ into product states. In general, the Schmidt measure is a difficult one to compute for an arbitrary pure multiqubit state. However, there exist computable lower and upper bounds of the measure for certain multiqubit states, including the graph states. A lower bound to the Schmidt measure in the case of graph states can be obtained as follows [48]. For a given graph G and a bipartition $A:B$ such that $G = A \cup B$, the adjacency matrix Γ_G can be written, without any loss in generality, as

$$\Gamma_G = \begin{pmatrix} \Gamma_A & \Gamma_{AB}^T \\ \Gamma_{AB} & \Gamma_B \end{pmatrix} \quad (\text{C7})$$

by rearranging the nodes, where T denotes the transposition operation. The Schmidt measure of the graph state w.r.t. the partition $A:B$ is given by the rank of the matrix Γ_{AB} :

$$E(|G\rangle\langle G|) = \text{rank}[\Gamma_{AB}]. \quad (\text{C8})$$

The lower bound to the Schmidt measure w.r.t. the partitioning of the system into smallest possible subsystems¹¹ is given by maximizing $E(|G\rangle\langle G|)$ over all possible bipartitions [48], as

$$E_L(|G\rangle\langle G|) = \max_{\forall(A:B)} E(|G\rangle\langle G|). \quad (\text{C9})$$

On the other hand, an upper bound to the Schmidt measure in the case of graph states is given by the *Pauli persistency*, defined as the minimum number of local Pauli measurements required to completely disentangle the state [48]. We exploit the measurement protocol for the evaluation of this upper bound as follows. For a graph state $|G\rangle$ on N qubits, and for a chosen Pauli measurement setup \mathcal{P} on these N qubits, let us denote the reduced graph, obtained according to Eq. (23),

¹¹In the present case, each partition would hold one qubit.

by G' . The minimal vertex cover of this reduced graph G' is defined as the minimum cardinality of the subset of nodes in G' such that upon deletion of edges on them is left behind a completely disconnected graph on N vertices which we denote by $M(G')$. An upper bound to the Schmidt measure of $|G\rangle$ is given by minimizing $M(G')$ over all possible Pauli measurements:

$$E_U(|G\rangle\langle G|) = \min_{\mathcal{P}} M(G'). \quad (\text{C10})$$

b. Generalized geometric measure

Let us consider a K -separable N -qubit quantum state $|\phi_K\rangle$, which can be divided into K product state partitions, where $2 \leq K \leq N$. The GME in an N -qubit state $|\psi\rangle$ is quantified by the K -geometric measure (K-GM) of entanglement, defined as the minimum distance of the state $|\psi\rangle$ from the set \mathcal{S}_K of all possible K -separable states:

$$E(|\psi\rangle) = 1 - \max_{\mathcal{S}_K} |\langle \phi_K | \psi \rangle|^2. \quad (\text{C11})$$

The original definition of the geometric measure is recovered for $K = N$, while at the other extremum $K = 2$, the measure is called the generalized geometric measure (GGM). The optimization in the definition of the GGM can be achieved via a maximization of the Schmidt coefficients across all possible bipartitions of $|\psi\rangle$ [98], leading to

$$E = 1 - \max_{S:A:B} \{\lambda_{A:B}^2\}, \quad (\text{C12})$$

where $\lambda_{A:B}$ is the maximum Schmidt coefficient of $|\psi\rangle$ in the bipartition $A : B$, and the maximization in Eq. (C12) is over the set $S_{A:B}$ of all possible bipartitions $A : B$ of the N -qubit system. The GGM of a pure state of arbitrary number of qubits, N , can be computed using Eq. (C12).

APPENDIX D: PROOF OF PROPOSITION 2

Proof. Using

$$J_{S''} = J_{S,S''} \otimes J_{S',S''} \quad (\text{D1})$$

and

$$q_s = q_{S,S} \times q_{S',S} \quad (\text{D2})$$

with $q_{S(S'),S} = \prod_{j \in S(S')} q_{s_j}$, and $\sum_{(S',S)} q_{S',S} = \sum_{(S,S)} q_{S,S} = 1$, one can trace out S' from ϱ_k to obtain

$$\varrho_S^k = \mathbf{V}_{S,\alpha} \tilde{\varrho}_S^k \mathbf{V}_{S,\alpha}^\dagger \quad (\text{D3})$$

with

$$\tilde{\varrho}_S^k = \sum_{(S,S)} q_{S,S} J_{S,S''} \tilde{\rho}_S J_{S,S''}^\dagger, \quad (\text{D4})$$

where $\tilde{\rho}_S$ is a GD state in the graph-state basis corresponding to the graph G_S^α on the subsystem S , obtained from G_α' [see Eq. (B10)]. We write $\tilde{\rho}_S$ as

$$\tilde{\rho}_S = \sum_{\psi} \lambda_{\psi}(\alpha, s) |\psi\rangle\langle\psi|, \quad (\text{D5})$$

$\{|\psi\rangle\}$ being the graph basis in the Hilbert space of S where $\psi \in [0, 2^n - 1]$, and ψ can be identified as $\psi \equiv \psi_1 \psi_2 \dots \psi_n$, where $\psi_i \in \{0, 1\} \forall i \in S$. In this notation $|0\rangle\langle 0| \equiv |G_S^\alpha\rangle\langle G_S^\alpha|$, and (see Sec. III A)

$$|\psi\rangle = \otimes_{i \in S} (\sigma_i^3)^{\psi_i} |G_S^\alpha\rangle. \quad (\text{D6})$$

Note that the *mixing probabilities* $\lambda_{\psi}(\alpha, s)$ are in general functions of the PMS, α , and the type of the noise, s . These probabilities and subsequently the state $\tilde{\rho}_S$ can be calculated from the knowledge of the connectivity between the sets of qubits S and S''_1 , where $S''_1 \subseteq S'_1$ such that $s_j = 1, 2 \forall j \in S''_1$, i.e., the noise on S''_1 does not commute with the measurement, which is σ^3 for all qubits in S''_1 . A technical account of the prescription for calculating $\tilde{\rho}_S$ is given in Appendix F for interested readers.

Note further that an application of Eq. (D4) on $\tilde{\rho}_S$ leads to another GD state on S . To determine this, we first obtain the GD state resulting from the application of Eq. (D4) on $|\psi\rangle\langle\psi| \equiv |0\rangle\langle 0| = |G_S^\alpha\rangle\langle G_S^\alpha|$ [using Eq. (40)] as

$$\sum_{(S,S)} q_{S,S} J_{S,S''} |0\rangle\langle 0| J_{S,S''}^\dagger = \sum_{\psi'} \lambda_{\psi'}(\alpha, s) |\psi'\rangle\langle\psi'|, \quad (\text{D7})$$

and then use Eqs. (D5) and (D7) in Eq. (D4), with the aid of Eq. (D6), to obtain

$$\tilde{\varrho}_S^k = \sum_{(S,S)} q_{S,S} J_{S,S''} \left[\sum_{\psi} \lambda_{\psi} |\psi\rangle\langle\psi| \right] J_{S,S''}^\dagger \quad (\text{D8})$$

$$= \sum_{\psi, \psi'} \lambda_{\psi} \lambda_{\psi'} |\psi \oplus \psi'\rangle\langle\psi \oplus \psi'|, \quad (\text{D9})$$

where $\psi \oplus \psi'$ represents modular two addition of the binary strings ψ and ψ' . Also to arrive at Eq. (D9), we use $\sigma^3 \sigma^j \sigma^3 = \sigma^j$, $j \in \{1, 2, 3\}$ up to irrelevant multiplicative factors.

From Eq. (D3), it is clear that

$$E(\varrho_S^k) = E(\tilde{\varrho}_S^k). \quad (\text{D10})$$

Moreover, note that for two distinct outcomes k_1 and k_2 having their respective components in S''_1 as l'_1 and l'_2 ¹², $l'_2 = l'_1 \oplus L'$ in binary representation, where L' is another binary string of the same length as l'_1, l'_2 . Therefore, a sum over l'_1 [see Eq. (47)]¹³ is equivalent to a sum over l'_2 for a fixed L' . This results in local unitary connected states for the two outcomes k_1 and k_2 as

$$\tilde{\varrho}_S^{k_1} = \mathbf{W}_S^{L'} \tilde{\varrho}_S^{k_2} \mathbf{W}_S^{L'}, \quad (\text{D11})$$

where $\mathbf{W}_S^{L'}$ is a local unitary operator acting on S , having the form

$$\mathbf{W}_S^{L'} = \prod_{j \in S''_1} \otimes_{i \in \mathcal{N}_j \cap S} (\sigma_i^3)^{L'_j}, \quad (\text{D12})$$

where L'_j is the outcome on the j th qubit, $j \in S''_1$. Therefore, $E(\tilde{\varrho}_S^{k_1}) = E(\tilde{\varrho}_S^{k_2})$ for any two distinct outcomes k_1, k_2 , which, along with Eq. (D10), leads to

$$E_S(\varrho_S^{k_1}) = E_S(\varrho_S^{k_2}). \quad (\text{D13})$$

Hence the proof. \blacksquare

¹²Note that l'_1 and l'_2 can be seen as the parts of corresponding l'_s that belong to S''_1 .

¹³Note that the sum over s in Eq. (47) can be seen as an effective sum over all possible l'_1 .

TABLE II. Change of outcomes due to Pauli noise on a qubit in the case of the example shown in Fig. 2, where BPF noise is applied to all qubits, and (A) σ^3 and (B) σ^1 measurements are performed on qubits 1 and 2. In the case of (B), allowed and forbidden outcomes are labeled by (a) and (f).

A. $\alpha \in \Gamma$ (all outcomes are allowed)				
$k \equiv l_1 m_2$	$k' \equiv l'_1 m'_2$			
	$s_1 = 0, s_2 = 0$	$s_1 = 0, s_2 = 2$	$s_1 = 2, s_2 = 0$	$s_1 = 2, s_2 = 2$
(+1)(+1)	(+1)(+1)	(+1)(-1)	(-1)(+1)	(-1)(-1)
(+1)(-1)	(+1)(-1)	(+1)(+1)	(-1)(-1)	(-1)(+1)
(-1)(+1)	(-1)(+1)	(-1)(-1)	(+1)(+1)	(+1)(-1)
(-1)(-1)	(-1)(-1)	(-1)(+1)	(+1)(-1)	(+1)(+1)
B. $\alpha \in \bar{\Gamma}$ (some outcomes are allowed)				
$k \equiv l_1 m_2$	$k' \equiv l'_1 m'_2$			
	$s_1 = 0, s_2 = 0$	$s_1 = 0, s_2 = 2$	$s_1 = 2, s_2 = 0$	$s_1 = 2, s_2 = 2$
(+1)(+1) (a)	(+1)(+1) (a)	(+1)(-1) (f)	(-1)(+1) (f)	(-1)(-1) (a)
(+1)(-1) (f)	(+1)(-1) (f)	(+1)(+1) (a)	(-1)(-1) (a)	(-1)(+1) (f)
(-1)(+1) (f)	(-1)(+1) (f)	(-1)(-1) (a)	(+1)(+1) (a)	(+1)(-1) (f)
(-1)(-1) (a)	(-1)(-1) (a)	(-1)(+1) (f)	(+1)(-1) (f)	(+1)(+1) (a)

APPENDIX E: CALCULATING LOCALIZABLE ENTANGLEMENT FOR THE GRAPH IN FIG. 2 UNDER NOISE

To demonstrate the calculation of localizable entanglement in the presence of noise, we consider the graph in Fig. 2(a), where each qubit is subjected to BPF noise.

1. When no outcomes are forbidden

Let us consider σ^3 measurements performed on qubits 1 and 2 constituting S' . Since $U_j = V_j = I$ corresponding to qubits $j = 1, 2$ in the case depicted in Fig. 2(a), the reduced graph is equivalent to the original graph, and $s'' = s' = s$ in Eqs. (41)–(47). The change $l_1 \rightarrow l'_1$ and $m_2 \rightarrow m'_2$ in Eq. (47) due to the values of s , according to Eq. (46), is tabulated in Table II(A). Note that in this specific example, all four measurement outcomes $k \equiv l_1 m_2$ are equally probable and remain so even after the change $l_1 \rightarrow l'_1$ and $m_2 \rightarrow m'_2$. Since both qubits in $S'_1 = \{1, 2\}$ are connected to the two qubits in S , the normalized state $\tilde{\rho}_S$ [see Eq. (D5)] corresponding to outcome $k = (+1)(+1) \equiv 00$, occurring with a probability $1/4$, can be written in a row vector notation as

$$\sum_{\psi} \lambda_{\psi} |\psi\rangle\langle\psi| \equiv \left[1 - q + \frac{q^2}{2}, 0, 0, q - \frac{q^2}{2} \right], \quad (\text{E1})$$

where λ_{ψ} is the value in the position ψ of the row. Similarly, equivalent to Eq. (D7), one may write

$$\sum_{\psi'} \lambda_{\psi'} |\psi'\rangle\langle\psi'| \equiv \left[1 - q + \frac{q^2}{2}, 0, 0, q - \frac{q^2}{2} \right]. \quad (\text{E2})$$

Combining the above equations in the case where $S'_2 = \emptyset$ and $k = l = (+1)(+1) \equiv 00$, one obtains, equivalent to Eq. (D9),

$$\tilde{\rho}_S^{(+1)(+1)} = \left[\left(1 - q + \frac{q^2}{2} \right)^2 + \left(q - \frac{q^2}{2} \right)^2, 0, 0, 2 \left(1 - q + \frac{q^2}{2} \right) \left(q - \frac{q^2}{2} \right) \right]. \quad (\text{E3})$$

The states $\tilde{\rho}_S^k$ for $k = (+1)(-1), (-1)(+1), (-1)(-1)$ are also equally probable with probability $1/4$ and can be obtained from $\tilde{\rho}_S^{(+1)(+1)}$ via local unitary transformations, where the local unitary operators can also be seen from Table II(A). For example outcomes $k = (+1)(+1) \equiv 00$ and $k = (-1)(+1) \equiv 10$ are connected by $L = 10$, and the corresponding states by the local unitary operator $\mathbf{W}_S^L = \sigma_1^3 \otimes \sigma_2^3$.

2. When forbidden set of outcomes is present

For $\alpha \in \bar{\Gamma}$, there exists a set of outcomes that are forbidden (see Sec. III B 2). In such cases, results discussed in the previous section hold except for the calculation of $\tilde{\rho}_S$, and the explicit calculation depends on the fact that the change $lm \rightarrow l'm'$ may result in a transition between allowed and forbidden sets of outcomes. We demonstrate this using the graph shown in Fig. 2(a), where each qubit is subjected to BPF noise, and σ^1 measurements are performed on qubits 1 and 2 constituting S' . Since $U_j = H$ corresponding to qubits $j = 1, 2$, and $V_1 = H, V_2 = I$ in this case, one has to work with the reduced graph shown in Fig. 2(b). Also, $s'' = s' = s$ in Eqs. (41)–(47), since BPF does not change under Hadamard operation. The transformations $l_1 \rightarrow l'_1$ and $m_2 \rightarrow m'_2$ in Eq. (47) due to the values of s , according to Eq. (46) are tabulated in Table II(B). Since $S'_2 = \{1\}$ and $S'_1 = S'_1 = \{2\}$ are connected to the two qubits in S , $\tilde{\rho}_S$ corresponding to the outcome $k = lm = (+1)(+1) \equiv 00$ occurring with probability $(1 - q + q^2/2)/2$, can be written as [equivalent to Eq. (D5)]

$$\sum_{\psi} \lambda_{\psi} |\psi\rangle\langle\psi| \equiv \left[\frac{1 - q + \frac{q^2}{4}}{1 - q + \frac{q^2}{2}}, 0, 0, \frac{\frac{q^2}{4}}{1 - q + \frac{q^2}{2}} \right]. \quad (\text{E4})$$

It is worthwhile to point out that in contrast to the case discussed in Sec. E 1, the probabilities are no longer independent of q —an artifact due to the transition between the outcomes belonging to the allowed and forbidden sets. Proceeding as

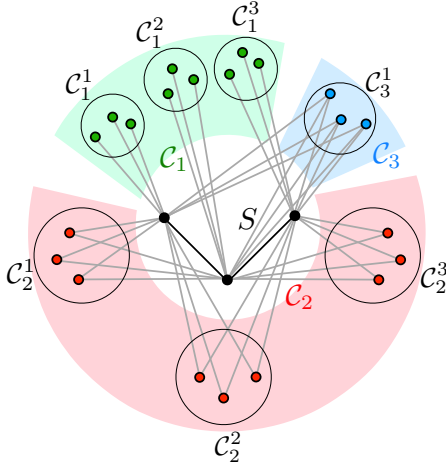


FIG. 23. Schematic representation of the class structure of the subsystem S' of a graph, where entanglement is to be localized over a subsystem S of size 3. To keep the figure uncluttered, only the subsystems S'_1 , S , the links between S'_1 and S , and the links between the nodes in S are drawn.

before, one can write the normalized $\tilde{\rho}_S^{(+1)(+1)}$ as

$$\tilde{\rho}_S^{(+1)(+1)} = \left[1 - q + \frac{q^2}{4} + \frac{(q - \frac{q^2}{2})\frac{q^2}{4}}{1 - q + \frac{q^2}{2}}, 0, 0, \frac{q^2}{4} + \frac{(q - \frac{q^2}{2})(1 - q + \frac{q^2}{4})}{1 - q + \frac{q^2}{2}} \right]. \quad (\text{E5})$$

In a similar fashion, one may also obtain $\tilde{\rho}_S^{(+1)(-1)}$ as

$$\tilde{\rho}_S^{(+1)(-1)} = \left[\frac{1}{2}, 0, 0, \frac{1}{2} \right], \quad (\text{E6})$$

which clearly indicates that $\tilde{\rho}_S^{(+1)(-1)}$ and $\tilde{\rho}_S^{(+1)(+1)}$ are not connected by local unitary operators. Thus, in general, a local unitary connection among states corresponding to all the allowed outcomes does not exist, thereby taking away the advantage in the computation, as opposed to the case described in Sec. E 1, specifically in situations where the system size is large. Note also that the outcomes which are initially forbidden at $q = 0$ need not necessarily remain forbidden for $q > 0$. In the above example, $k = (-1)(+1)$ is forbidden at $q = 0$ but acquires a nonzero probability $q(1 - q/2)/2$ for $q > 0$.

APPENDIX F: DETERMINATION OF $\tilde{\rho}_S$

Here we discuss the calculation of $\tilde{\rho}_S$ (see Sec. D and Sec. E 1). Let us define $S'_1 \subseteq S'_1$ such that S'_1 consists of all nodes in S'_1 that have $s' \in \{1, 2\}$. Let us further divide the nodes in S'_1 into n classes, n being the size of S , such that each of the nodes in the m th class, C_m ($m = 1, 2, \dots, n$), is connected to m nodes in S . Since m nodes from S can be chosen in $\binom{n}{m}$ possible ways, the m th class can be further divided into $\binom{n}{m}$ subclasses, which we denote by C_m^r , where each C_m^r has a size $|C_m^r|$, $1 \leq r \leq \binom{n}{m}$. See Fig. 23 for an example of a possible class structure in the case of $n = 3$.

We once again use the binary representation to work using the graph state basis $\{|\psi\rangle\}$ (see Sec. D), where $|G_S\rangle = |0\rangle$.

The local unitary corrections (either I or σ^3) applied to $|G_S\rangle$ can be represented in binary representation as

$$|\psi\rangle = \mathbf{W}^\psi |0\rangle, \quad \text{with } \mathbf{W}^\psi = \otimes_{j=1}^n (\sigma_j^3)^{\psi_j}. \quad (\text{F1})$$

In this representation, one can determine the *effective correction* of each of the subclasses C_m^r in the m th class on S by a *parity bit*, denoted by $\gamma(r, m)$, such that for $\gamma(r, m) = 0$ ($\gamma(r, m) = 1$), there will be no correction (a σ^3 correction) applied to each node in S that are connected to the nodes in C_m^r [see Eqs. (B8) and (B9)]. The overall correction, denoted by \mathbf{W}^ψ , applied on S will be the product of all corrections due to all subclasses from all of the classes:

$$\mathbf{W}^\psi = \prod_{m=1}^n \prod_{r=1}^{\binom{n}{m}} (\sigma_{\mathcal{N}(r,m)}^3)^{\gamma(r,m)}, \quad (\text{F2})$$

where $\mathcal{N}(r,m)$ denotes the set of all nodes in S connected to the subclass C_m^r .

Note that there may exist different combinations of $\gamma(r, m)$ giving rise to the same correction \mathbf{W}^ψ . For example, in the case of $n = 3$ (Fig. 23) both $\gamma(r, m) = 0 \forall m, r$ and $\gamma(r, m) = 1 \forall m, r$ give rise to the trivial correction $I \otimes I \otimes I$ in S . Defining the total number of possible subclasses with $m \geq 2$ as

$$D = \sum_{m=2}^n \binom{n}{m}, \quad (\text{F3})$$

there will be a total of $n + D$ subclasses for S since $\binom{n}{1} = n$. The purpose of this division into D and n will be evident soon. We now denote a binary string of $n + D$ bits as

$$\gamma = \gamma(1, 1)\gamma(2, 1) \dots \gamma(n, 1)\gamma(1, 2)\gamma(2, 2) \dots \gamma(n, 2) \dots \gamma(1, n)\gamma(2, n) \dots \gamma(1, n). \quad (\text{F4})$$

The first n of the parity bits in γ are reserved for $m = 1$ class, and the other D bits are assigned to the remaining D subclasses of the classes $m = 2, \dots, n$. In this notation mixing probabilities, λ_ψ , are given by

$$\lambda_\psi = \sum_{\gamma=0}^{2^D-1} \prod_{m=1}^n \prod_{r=1}^{\binom{n}{m}} P_{\gamma(r,m)}(r, m) \quad (\text{F5})$$

with

$$P_{\gamma(r,m)}(r, m) = \frac{1}{2} [1 + (-1)^{\gamma(r,m)} (1 - 2q_n)^{|C_m^r|}] \quad (\text{F6})$$

and

$$\gamma(i, 1) = \psi_i \oplus \bigoplus_{\substack{(r,m), m>1 \\ i \in \mathcal{N}(r,m)}} \gamma(r, m), \quad (\text{F7})$$

where i denotes a qubit in S , the $i \in \mathcal{N}(r,m)$ condition picks up only those subclasses in which a connection exists between i and C_m^r , \oplus denotes modular 2 addition, and q_n is the total probability of occurrence of change of outcome on a single qubit, $l_j \rightarrow l'_j$ [see Eq. (46)], for various noises considered in this paper. For an example $q_n = q/2$ for Markovian BF and $q_n = 0$ for Markovian PD noises. An explicit calculation with $n = 2$ can be found in [132].

We point out here that the above calculation assumes identical noise strengths and non-Markovianity parameters on

each qubit, irrespective of the type of noise present on the qubit in a specific subclass. However, one can also generalize to a scenario where (q_i, ϵ_i) on different qubits in a subclass are different, which originates from different (q_i, ϵ_i) on different qubits in the original graph. This leads to a form of $P_{\gamma(r,m)}(r, m)$ given by

$$P_1(r, m) = \sum_{\substack{\beta=1, \\ \oplus \beta_i=1}}^{2^{|\mathcal{C}_m^r|}} \prod_{i \in \mathcal{C}_m^r} p_i^{\beta_i} (1 - p_i)^{1 \oplus \beta_i},$$

$$P_0(r, m) = 1 - P_1(r, m), \quad (\text{F8})$$

where $\beta = \beta_1 \beta_2 \cdots \beta_{|\mathcal{C}_m^r|}$ is a multi-index with $\beta_i \in \{0, 1\}$, and p_i is the probability of occurrence of noise on qubit i , given by

$$p_i = \frac{q_i}{2} \left[1 + \epsilon_i \left(1 - \frac{q_i}{2} \right) \right] \quad (\text{F9})$$

for the BF and the BPF noise, and

$$p_i = \frac{q_i}{4} \left[1 + 3\epsilon_i \left(1 - \frac{3q_i}{4} \right) \right] \quad (\text{F10})$$

for the DP noise. An example of this scenario can be found in Sec. IV C.

APPENDIX G: ENTANGLEMENT IN GRAPH STATES UNDER NOISE

In the presence of noise, and for states with more than two qubits, the problem of quantifying entanglement is significantly more complicated. For a given bipartition of a graph state under Pauli noise, the bipartite entanglement can be quantified by negativity [106]. On the other hand, for a certain class of mixed states obtained when graph states are subjected to noise, such as the graph-diagonal states, useful criteria for detecting multipartite entanglement directly from the density matrix of the state exist [100,133]. One can also compute a *genuine multiparty concurrence* [102] for graph states under noise with an X state as the density matrix. We briefly discuss these in this section.

1. Negativity as a bipartite measure for a graph-diagonal state

For a graph-diagonal state ρ representing a graph with two partitions A and B , the negativity between A and B is defined as [106]

$$\mathcal{N}_{AB} = \frac{\|\rho^{T_A}\| - 1}{2}, \quad (\text{G1})$$

where T_A denotes the transposition of ρ w.r.t. the subsystem A , and $\|A\| = \text{Tr}[\sqrt{A^\dagger A}]$ for the matrix A .

2. Genuine multiparty entanglement in graph-diagonal states

Determination of the multipartite entanglement measures is difficult in the case of mixed states. However, in the case of specific types of mixed states, such as the graph diagonal states of certain types or number of parties, criteria for the state to be genuine multiparty entangled, or biseparable, or fully separable can be determined using the density matrix of the state [133]. We first consider the example of a mixed state of N qubits, which is diagonal in the graph state basis [see

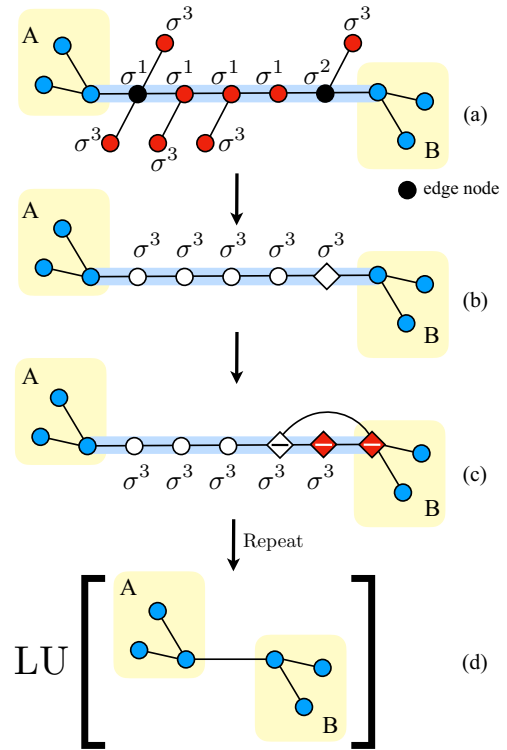


FIG. 24. (a) Pauli measurement setup to create a direct link between two subsystems A, B of a connected graph joined by a path (shaded), where the edge nodes are denoted by black dots. (b) Measurement transformations on each node on the path, including the edge nodes, where qubits outside the path are omitted for brevity. (c) The first of the five consecutive \mathcal{B}_1 operations on the nodes on the path that connects A and B during the graph reduction. (d) After the completion of graph reduction and the σ^3 measurements, A and B are connected by a direct link, and the corresponding graph state is equivalent to the state for this graph, up to local unitary operations (denoted by “LU”).

Eqs. (4)–(6)] corresponding to an N -qubit star graph, where

$$|G\rangle = \frac{1}{\sqrt{2}} [|0_0\rangle \otimes_{i=1}^{N-1} |+_i\rangle + |1_0\rangle \otimes_{i=1}^{N-1} |-_i\rangle], \quad (\text{G2})$$

with the node “0” being the hub to which all other nodes $i = 1, 2, \dots, N - 1$, are attached. We refer to this state as the *star-graph-diagonal* (SGD) state. Since an N -qubit star graph can be converted to the N -qubit GHZ state via single-qubit Hadamard operations on all qubits except the qubit “0” of the star graph, the SGD state can be transformed to a *GHZ-diagonal* (GHZD) state, given by Eqs. (4)–(6), with $|G\rangle$ replaced by the N -qubit GHZ state. Therefore, the biseparability criteria of an N qubit GHZD state [133] is equivalent to that of the N -qubit SGD state. An N -qubit GHZD state ρ is biseparable if the matrix elements $\rho_{(i,j)}$, $1 \leq i, j \leq 2^N$, of ρ in the computational basis satisfy

$$|\rho_{(1,2^N)}| \leq \sum_{i=1}^{2^{N-1}-1} [\rho_{(1+i,1+i)} \rho_{(2^N-i,2^N-i)}]^{1/2}. \quad (\text{G3})$$

Violation of (G3) indicates presence of GME in the state.

Note that the above example includes a full description of separability of all GD states on a three-qubit graph, since all

possible connected graphs on three qubits are local unitary equivalent to a star graph, representing a three-qubit GHZ state. Apart from the above example, the biseparability criteria for the case of four qubit GD states are also known [100]. Consider the four-qubit graph state $|G\rangle_{1234}$, where the qubits are labeled such that 1 and 4 are the edge qubits. For a diagonal state, ρ , in the graph state basis, where the fidelities in the said basis are defined as $F_{ijkl} = \langle ijkl|\rho|ijkl\rangle$ with $|ijkl\rangle = (\sigma^3)^i \otimes (\sigma^3)^j \otimes (\sigma^3)^k \otimes (\sigma^3)^l |G\rangle_{1234}$, $\forall i, j, k, l \in \{0, 1\}$, the biseparability criteria are given by

$$F_{\alpha\beta\gamma\delta} \leq \frac{1}{2} \sum_{i,j} (F_{\alpha ij\delta} + F_{\bar{\alpha} ij\delta} + F_{\alpha i j \bar{\delta}}), \quad (\text{G4})$$

$$F_{\alpha\beta\gamma\delta} + F_{\bar{\alpha}\mu\nu\bar{\delta}} \leq \frac{1}{2} \sum_{i,j} (F_{\alpha ij\delta} + F_{\bar{\alpha} ij\delta} + F_{\alpha i j \bar{\delta}} + F_{\bar{\alpha} i j \bar{\delta}}). \quad (\text{G5})$$

Here $\bar{\alpha} = (1 + \alpha) \bmod 2$. A violation of either of the inequalities (G4) or (G5) indicates existence of GME in the state ρ .

3. Genuine multiparty concurrence

We also point out that the density matrix of a GHZD state has the form of an X state. For such states, one may compute the *genuine multiparty concurrence* [102] (GMC) as a multipartite entanglement measure for X states, which is defined as $C_{GM} = 2 \max_j [0, \lambda]$ with

$$\lambda = \left| \rho_{(j, 2^N - j - 1)} \right| - \sum_{i=1, i \neq j}^{2^N - 1} \left[\rho_{(1+i, 1+i)} \rho_{(2^N - i, 2^N - i)} \right]^{\frac{1}{2}}. \quad (\text{G6})$$

We use this measure specifically in the case of the topological quantum codes under noise (see Sec. V).

APPENDIX H: MEASUREMENT PROTOCOL FOR LOCALIZING CONNECTED SUBSYSTEM

In this section, we introduce a PMS through which any two subsystems A, B of a connected graph G can be directly connected by a link, given that there exists a path in the original graph G connecting the two subsystems A and B . Let us denote the nodes in the path that is connected to a qubit in either A or B as *edge nodes*. The PMS, then, would be such that (see Fig. 24)

(a) σ^2 measurement is performed on one of the edge nodes, while σ^1 measurement is performed on the rest of the nodes in the path and

(b) σ^3 measurement is performed on all other nodes in the graph.

Note that the σ^3 measurements on qubits not in the path leave only A, B and the path connected. Further, starting from the σ^2 measurement on the edge node, a series of \mathcal{B}_1 operations occur during the graph reduction (see Sec. A 1) along the path, so that A and B , at the end, become connected by a direct link. Note also that if both the edge nodes share only one link each with A and B , respectively, then the above PMS results in a direct link between A and B without changing the connectivity within A and B . We use this PMS in the case of Fig. 17, with additional basis transformations according to Table I due to the Hadamard operations on the control nodes connecting the stabilizer state from the toric code, and the local unitarily connected graph.

-
- [1] R. Horodecki, P. Horodecki, M. Horodecki, and K. Horodecki, Quantum entanglement, *Rev. Mod. Phys.* **81**, 865 (2009).
 - [2] O. Gühne and G. Tóth, Entanglement detection, *Phys. Rep.* **474**, 1 (2009).
 - [3] R. Raussendorf and H. J. Briegel, A One-Way Quantum Computer, *Phys. Rev. Lett.* **86**, 5188 (2001).
 - [4] P. Walther, K. J. Resch, T. Rudolph, E. Schenck, H. Weinfurter, V. Vedral, M. Aspelmeyer, and A. Zeilinger, Experimental one-way quantum computing, *Nature (London)* **434**, 169 (2005).
 - [5] H. J. Briegel, D. E. Browne, W. Dür, R. Raussendorf, and M. Van den Nest, Measurement-based quantum computation, *Nat. Phys.* **5**, 19 (2009).
 - [6] A. K. Ekert, Quantum Cryptography Based on Bell's Theorem, *Phys. Rev. Lett.* **67**, 661 (1991).
 - [7] A. Karlsson, M. Koashi, and N. Imoto, Quantum entanglement for secret sharing and secret splitting, *Phys. Rev. A* **59**, 162 (1999).
 - [8] T. Jennewein, C. Simon, G. Weihs, H. Weinfurter, and A. Zeilinger, Quantum Cryptography with Entangled Photons, *Phys. Rev. Lett.* **84**, 4729 (2000).
 - [9] D. S. Naik, C. G. Peterson, A. G. White, A. J. Berglund, and P. G. Kwiat, Entangled State Quantum Cryptography: Eavesdropping on the Ekert Protocol, *Phys. Rev. Lett.* **84**, 4733 (2000).
 - [10] N. Gisin, G. Ribordy, W. Tittel, and H. Zbinden, Quantum cryptography, *Rev. Mod. Phys.* **74**, 145 (2002).
 - [11] C. H. Bennett and S. J. Wiesner, Communication via One- and Two-Particle Operators on Einstein-Podolsky-Rosen States, *Phys. Rev. Lett.* **69**, 2881 (1992).
 - [12] K. Mattle, H. Weinfurter, P. G. Kwiat, and A. Zeilinger, Dense Coding in Experimental Quantum Communication, *Phys. Rev. Lett.* **76**, 4656 (1996).
 - [13] A. Sen(De) and U. Sen, Quantum advantage in communication networks, *Phys. News* **40**, 17 (2011).
 - [14] D. Bruß, G. M. D'Ariano, M. Lewenstein, C. Macchiavello, A. Sen(De), and U. Sen, Distributed Quantum Dense Coding, *Phys. Rev. Lett.* **93**, 210501 (2004).
 - [15] D. Bruß, M. Lewenstein, A. Sen(De), U. Sen, G. M. D'Ariano, and C. Macchiavello, Dense coding with multipartite quantum states, *Int. J. Quantum. Inform.* **04**, 415 (2006).
 - [16] T. Das, R. Prabhu, A. Sen De, and U. Sen, Multipartite dense coding versus quantum correlation: Noise inverts relative capability of information transfer, *Phys. Rev. A* **90**, 022319 (2014).
 - [17] T. Das, R. Prabhu, A. Sen De, and U. Sen, Distributed quantum dense coding with two receivers in noisy environments, *Phys. Rev. A* **92**, 052330 (2015).
 - [18] L. Amico, R. Fazio, A. Osterloh, and V. Vedral, Entanglement in many-body systems, *Rev. Mod. Phys.* **80**, 517 (2008).

- [19] G. De Chiara and A. Sanpera, Genuine quantum correlations in quantum many-body systems: A review of recent progress, *Rep. Prog. Phys.* **81**, 074002 (2018).
- [20] M. Sarovar, A. Ishizaki, G. R. Fleming, and K. B. Whaley, Quantum entanglement in photosynthetic light-harvesting complexes, *Nat. Phys.* **6**, 462 (2010).
- [21] J. Zhu, S. Kais, A. Aspuru-Guzik, S. Rodrigues, B. Brock, and P. J. Love, Multipartite quantum entanglement evolution in photosynthetic complexes, *J. Chem. Phys.* **137**, 074112 (2012).
- [22] N. Lambert, Y.-N. Chen, Y. C. Cheng, C.-M. Li, G. Y. Chen, and F. Nori, Quantum biology, *Nat. Phys.* **9**, 10 (2013).
- [23] V. Balasubramanian, P. Hayden, A. Maloney, D. Marolf, and S. F. Ross, Multiboundary wormholes and holographic entanglement, *Class. Quantum Grav.* **31**, 185015 (2014).
- [24] V. E. Hubeny, The AdS/CFT correspondence, *Class. Quantum Grav.* **32**, 124010 (2015).
- [25] F. Pastawski, B. Yoshida, D. Harlow, and J. Preskill, Holographic quantum error-correcting codes: Toy models for the bulk/boundary correspondence, *J. High Energy Phys.* **06** (2015) 149.
- [26] A. Almheiri, X. Dong, and D. Harlow, Bulk locality and quantum error correction in AdS/CFT, *J. High Energy Phys.* **04** (2015) 163.
- [27] A. Jahn, M. Gluza, F. Pastawski, and J. Eisert, Holography and criticality in matchgate tensor networks, *Sci. Adv.* **5**, eaaw0092 (2019).
- [28] J. Harper, Multipartite entanglement and topology in holography, *J. High Energy Phys.* **03** (2021) 116.
- [29] D. Leibfried, E. Knill, S. Seidelin, J. Britton, R. B. Blakestad, J. Chiaverini, D. B. Hume, W. M. Itano, J. D. Jost, C. Langer *et al.*, Creation of a six-atom ‘Schrödinger cat’ state, *Nature (London)* **438**, 639 (2005).
- [30] T. Monz, P. Schindler, J. T. Barreiro, M. Chwalla, D. Nigg, W. A. Coish, M. Harlander, W. Hänsel, M. Hennrich, and R. Blatt, 14-Qubit Entanglement: Creation and Coherence, *Phys. Rev. Lett.* **106**, 130506 (2011).
- [31] O. Mandel, M. Greiner, A. Widera, T. Rom, T. W. Hansch, and I. Bloch, Controlled collisions for multi-particle entanglement of optically trapped atoms, *Nature (London)* **425**, 937 (2003).
- [32] I. Bloch, Exploring quantum matter with ultracold atoms in optical lattices, *J. Phys. B: At. Mol. Opt. Phys.* **38**, S629 (2005).
- [33] P. Treutlein, T. Steinmetz, Y. Colombe, B. Lev, P. Hommelhoff, J. Reichel, M. Greiner, O. Mandel, A. Widera, T. Rom *et al.*, Quantum information processing in optical lattices and magnetic microtraps, *Fortschr. Phys.* **54**, 702 (2006).
- [34] M. Cramer, A. Bernard, N. Fabbri, L. Fallani, C. Fort, S. Rosi, F. Caruso, M. Inguscio, and M. B. Plenio, Spatial entanglement of bosons in optical lattices, *Nat. Commun.* **4**, 2161 (2013).
- [35] R. Prevedel, G. Cronenberg, M. S. Tame, M. Paternostro, P. Walther, M. S. Kim, and A. Zeilinger, Experimental Realization of Dicke States of Up to Six Qubits for Multipartite Quantum Networking, *Phys. Rev. Lett.* **103**, 020503 (2009).
- [36] W.-B. Gao, C.-Y. Lu, X.-C. Yao, P. Xu, O. Gühne, A. Goebel, Y.-A. Chen, C.-Z. Peng, Z.-B. Chen, and J.-W. Pan, Experimental demonstration of a hyper-entangled ten-qubit Schrödinger cat state, *Nat. Phys.* **6**, 331 (2010).
- [37] X.-C. Yao, T.-X. Wang, P. Xu, H. Lu, G.-S. Pan, X.-H. Bao, C.-Z. Peng, C.-Y. Lu, Y.-A. Chen, and J.-W. Pan, Observation of eight-photon entanglement, *Nat. Photonics* **6**, 225 (2012).
- [38] X.-L. Wang, Y.-H. Luo, H.-L. Huang, M.-C. Chen, Z.-E. Su, C. Liu, C. Chen, W. Li, Y.-Q. Fang, X. Jiang *et al.*, 18-Qubit Entanglement with Six Photons’ Three Degrees of Freedom, *Phys. Rev. Lett.* **120**, 260502 (2018).
- [39] C. Negrevergne, T. S. Mahesh, C. A. Ryan, M. Ditty, F. Cyprien, W. Power, N. Boulant, T. Havel, D. G. Cory, and R. Laflamme, Benchmarking Quantum Control Methods on a 12-Qubit System, *Phys. Rev. Lett.* **96**, 170501 (2006).
- [40] R. Barends, J. Kelly, A. Megrant, A. Veitia, D. Sank, E. Jeffrey, T. C. White, J. Mutus, A. G. Fowler, B. Campbell *et al.*, Superconducting quantum circuits at the surface code threshold for fault tolerance, *Nature (London)* **508**, 500 (2014).
- [41] M. A. Nielsen and I. L. Chuang, *Quantum Computation and Quantum Information* (Cambridge University Press, Cambridge, 2010).
- [42] M. Hayashi, D. Markham, M. Muraio, M. Owari, and S. Virmani, Entanglement of multiparty-stabilizer, symmetric, and antisymmetric states, *Phys. Rev. A* **77**, 012104 (2008).
- [43] M. Hein, W. Dür, J. Eisert, R. Raussendorf, M. Van den Nest, and H. J. Briegel, Entanglement in graph states and its applications, [arXiv:quant-ph/0602096](https://arxiv.org/abs/quant-ph/0602096).
- [44] D. M. Greenberger, M. A. Horne, and A. Zeilinger, *Bell’s Theorem, Quantum Theory and Conceptions of the Universe* (Kluwer, Amsterdam, 1989).
- [45] S. Bose, V. Vedral, and P. L. Knight, Multiparticle generalization of entanglement swapping, *Phys. Rev. A* **57**, 822 (1998).
- [46] M. Hillery, V. Bužek, and A. Berthiaume, Quantum secret sharing, *Phys. Rev. A* **59**, 1829 (1999).
- [47] V. Giovannetti, S. Lloyd, and L. Maccone, Quantum-enhanced measurements: Beating the standard quantum limit, *Science* **306**, 1330 (2004).
- [48] M. Hein, J. Eisert, and H. J. Briegel, Multipartite entanglement in graph states, *Phys. Rev. A* **69**, 062311 (2004).
- [49] J. Wallnöfer, A. Pirker, M. Zwerger, and W. Dür, Multipartite state generation in quantum networks with optimal scaling, *Sci. Rep.* **9**, 314 (2019).
- [50] D. Gottesman, Stabilizer codes and quantum error correction, Ph.D. thesis, California Institute of Technology, 1997.
- [51] D. Gottesman, An introduction to quantum error correction and fault-tolerant quantum computation, in *Quantum Information Science and Its Contributions to Mathematics, Proc. Symposia in Applied Mathematics*, Vol. 68, edited by S. J. Lomonaco (American Mathematical Society, Providence, Rhode Island, 2010), pp. 13–58.
- [52] W. Dür, J. Calsamiglia, and H.-J. Briegel, Multipartite secure state distribution, *Phys. Rev. A* **71**, 042336 (2005).
- [53] K. Chen and H.-K. Lo, Multi-partite quantum cryptographic protocols with noisy GHz states, *Quantum Info. Comput.* **7**, 689 (2007).
- [54] H. Wunderlich and M. B. Plenio, Estimating purity and entropy in stabilizer state experiments, *Int. J. Quantum. Inform.* **08**, 325 (2010).
- [55] D. Nigg, M. Müller, E. A. Martinez, P. Schindler, M. Hennrich, T. Monz, M. A. Martin-Delgado, and R. Blatt, Quantum computations on a topologically encoded qubit, *Science* **345**, 302 (2014).

- [56] B. A. Bell, D. A. Herrera-Martí, M. S. Tame, D. Markham, W. J. Wadsworth, and J. G. Rarity, Experimental demonstration of a graph state quantum error-correction code, *Nat. Commun.* **5**, 3658 (2014).
- [57] J. Kelly, R. Barends, A. G. Fowler, A. Megrant, E. Jeffrey, T. C. White, D. Sank, J. Y. Mutus, B. Campbell, Y. Chen *et al.*, State preservation by repetitive error detection in a superconducting quantum circuit, *Nature (London)* **519**, 66 (2015).
- [58] C. Greganti, M.-C. Roehsner, S. Barz, M. Waegell, and P. Walther, Practical and efficient experimental characterization of multiqubit stabilizer states, *Phys. Rev. A* **91**, 022325 (2015).
- [59] N. M. Linke, M. Gutierrez, K. A. Landsman, C. Figgatt, S. Debnath, K. R. Brown, and C. Monroe, Fault-tolerant quantum error detection, *Sci. Adv.* **3**, e1701074 (2017).
- [60] K. Wright, K. M. Beck, S. Debnath, J. M. Amini, Y. Nam, N. Grzesiak, J.-S. Chen, N. C. Pimenti, M. Chmielewski, C. Collins *et al.*, Benchmarking an 11-qubit quantum computer, *Nat. Commun.* **10**, 5464 (2019).
- [61] M. Van den Nest, J. Dehaene, and B. De Moor, Graphical description of the action of local clifford transformations on graph states, *Phys. Rev. A* **69**, 022316 (2004).
- [62] D. Cavalcanti, R. Chaves, L. Aolita, L. Davidovich, and A. Acín, Open-System Dynamics of Graph-State Entanglement, *Phys. Rev. Lett.* **103**, 030502 (2009).
- [63] L. Aolita, D. Cavalcanti, R. Chaves, C. Dhara, L. Davidovich, and A. Acín, Noisy evolution of graph-state entanglement, *Phys. Rev. A* **82**, 032317 (2010).
- [64] M. Hein, W. Dür, and H.-J. Briegel, Entanglement properties of multipartite entangled states under the influence of decoherence, *Phys. Rev. A* **71**, 032350 (2005).
- [65] M. Ali, Dynamics of genuine multipartite entanglement under local non-Markovian dephasing, *Phys. Lett. A* **378**, 2048 (2014).
- [66] M. Ali and O. Gühne, Robustness of multiparticle entanglement: Specific entanglement classes and random states, *J. Phys. B: At. Mol. Opt. Phys.* **47**, 055503 (2014).
- [67] D. P. DiVincenzo, C. A. Fuchs, H. Mabuchi, J. A. Smolin, A. Thapliyal, and A. Uhlmann, Entanglement of assistance, in *Quantum Computing and Quantum Communications, QCQC 1998*, Lecture Notes in Computer Science, Vol. 1509, edited by C. P. Williams (Springer, Berlin, Heidelberg, 1999), pp. 247–257.
- [68] F. Verstraete, M. Popp, and J. I. Cirac, Entanglement versus Correlations in Spin Systems, *Phys. Rev. Lett.* **92**, 027901 (2004).
- [69] M. Popp, F. Verstraete, M. A. Martín-Delgado, and J. I. Cirac, Localizable entanglement, *Phys. Rev. A* **71**, 042306 (2005).
- [70] D. Amaro, M. Müller, and A. K. Pal, Estimating localizable entanglement from witnesses, *New J. Phys.* **20**, 063017 (2018).
- [71] D. Amaro, M. Müller, and A. K. Pal, Scalable characterization of localizable entanglement in noisy topological quantum codes, *New J. Phys.* **22**, 053038 (2020).
- [72] F. Verstraete, M. A. Martín-Delgado, and J. I. Cirac, Diverging Entanglement Length in Gapped Quantum Spin Systems, *Phys. Rev. Lett.* **92**, 087201 (2004).
- [73] B.-Q. Jin and V. E. Korepin, Localizable entanglement in antiferromagnetic spin chains, *Phys. Rev. A* **69**, 062314 (2004).
- [74] S. O. Skrøvseth and S. D. Bartlett, Phase transitions and localizable entanglement in cluster-state spin chains with Ising couplings and local fields, *Phys. Rev. A* **80**, 022316 (2009).
- [75] P. Smacchia, L. Amico, P. Facchi, R. Fazio, G. Florio, S. Pascazio, and V. Vedral, Statistical mechanics of the cluster Ising model, *Phys. Rev. A* **84**, 022304 (2011).
- [76] S. Montes and A. Hamma, Phase diagram and quench dynamics of the cluster-xy spin chain, *Phys. Rev. E* **86**, 021101 (2012).
- [77] Harikrishnan K. J. and A. K. Pal, Distinguishing phases via non-Markovian dynamics of entanglement in topological quantum codes under parallel magnetic field, *Phys. Rev. A* **105**, 052421 (2022).
- [78] A. Acín, J. I. Cirac, and M. Lewenstein, Entanglement percolation in quantum networks, *Nat. Phys.* **3**, 256 (2007).
- [79] X.-W. Wang, S.-Q. Tang, J.-B. Yuan, and L.-M. Kuang, Manipulation of tripartite-to-bipartite entanglement localization under quantum noises and its application to entanglement distribution, *J. Phys. B: At. Mol. Opt. Phys.* **48**, 025502 (2015).
- [80] R. Banerjee, A. K. Pal, and A. Sen De, Uniform decoherence effect on localizable entanglement in random multiqubit pure states, *Phys. Rev. A* **101**, 042339 (2020).
- [81] R. Banerjee, A. K. Pal, and A. Sen De, Hierarchies of localizable entanglement due to spatial distribution of local noise, *Phys. Rev. Res.* **4**, 023035 (2022).
- [82] J. G. Krishnan, Harikrishnan K. J., and A. K. Pal, Controlling gain with loss: Bounds on localizable entanglement in multiqubit systems, *Phys. Rev. A* **107**, 042411 (2023).
- [83] D. Sadhukhan, S. S. Roy, A. K. Pal, D. Rakshit, A. Sen De, and U. Sen, Multipartite entanglement accumulation in quantum states: Localizable generalized geometric measure, *Phys. Rev. A* **95**, 022301 (2017).
- [84] M. B. Elliott, B. Eastin, and C. M. Caves, Graphical description of the action of Clifford operators on stabilizer states, *Phys. Rev. A* **77**, 042307 (2008).
- [85] M. B. Elliott, B. Eastin, and C. M. Caves, Graphical description of Pauli measurements on stabilizer states, *J. Phys. A: Math. Theor.* **43**, 025301 (2010).
- [86] A. S. Holevo and V. Giovannetti, Quantum channels and their entropic characteristics, *Rep. Prog. Phys.* **75**, 046001 (2012).
- [87] T. Yu and J. H. Eberly, Quantum Open System Theory: Bipartite Aspects, *Phys. Rev. Lett.* **97**, 140403 (2006).
- [88] S. Daffer, K. Wódkiewicz, J. D. Cresser, and J. K. McIver, Depolarizing channel as a completely positive map with memory, *Phys. Rev. A* **70**, 010304(R) (2004).
- [89] U. Shrikant, R. Srikanth, and S. Banerjee, Non-Markovian dephasing and depolarizing channels, *Phys. Rev. A* **98**, 032328 (2018).
- [90] R. Gupta, S. Gupta, S. Mal, and A. Sen De, Constructive feedback of non-Markovianity on resources in random quantum states, *Phys. Rev. A* **105**, 012424 (2022).
- [91] N. Lang and H. P. Büchler, Minimal instances for toric code ground states, *Phys. Rev. A* **86**, 022336 (2012).
- [92] E. Dennis, A. Kitaev, A. Landahl, and J. Preskill, Topological quantum memory, *J. Math. Phys.* **43**, 4452 (2002).
- [93] A. Kitaev, Anyons in an exactly solved model and beyond, *Ann. Phys.* **321**, 2 (2006).
- [94] R. Diestel, *Graph Theory* (Springer, Heidelberg, 2000).
- [95] D. B. West, *Introduction to Graph Theory* (Prentice Hall, Upper Saddle River, NJ, 2001).

- [96] H. J. Briegel and R. Raussendorf, Persistent Entanglement in Arrays of Interacting Particles, *Phys. Rev. Lett.* **86**, 910 (2001).
- [97] A. Sen De and U. Sen, Channel capacities versus entanglement measures in multipartite quantum states, *Phys. Rev. A* **81**, 012308 (2010).
- [98] A. Biswas, R. Prabhu, A. Sen De, and U. Sen, Genuine-multipartite-entanglement trends in gapless-to-gapped transitions of quantum spin systems, *Phys. Rev. A* **90**, 032301 (2014).
- [99] F. Verstraete, J. Dehaene, and B. De Moor, Normal forms and entanglement measures for multipartite quantum states, *Phys. Rev. A* **68**, 012103 (2003).
- [100] O. Gühne, B. Jungnitsch, T. Moroder, and Y. S. Weinstein, Multipartite entanglement in graph-diagonal states: Necessary and sufficient conditions for four qubits, *Phys. Rev. A* **84**, 052319 (2011).
- [101] W. Dür and H.-J. Briegel, Stability of Macroscopic Entanglement under Decoherence, *Phys. Rev. Lett.* **92**, 180403 (2004).
- [102] S. M. Hashemi Rafsanjani, M. Huber, C. J. Broadbent, and J. H. Eberly, Genuinely multipartite concurrence of n -qubit x matrices, *Phys. Rev. A* **86**, 062303 (2012).
- [103] A. Peres, Separability Criterion for Density Matrices, *Phys. Rev. Lett.* **77**, 1413 (1996).
- [104] M. Horodecki, P. Horodecki, and R. Horodecki, Separability of mixed states: Necessary and sufficient conditions, *Phys. Lett. A* **223**, 1 (1996).
- [105] K. Życzkowski, P. Horodecki, A. Sanpera, and M. Lewenstein, Volume of the set of separable states, *Phys. Rev. A* **58**, 883 (1998).
- [106] G. Vidal and R. F. Werner, Computable measure of entanglement, *Phys. Rev. A* **65**, 032314 (2002).
- [107] M. B. Plenio, Logarithmic Negativity: A Full Entanglement Monotone That Is Not Convex, *Phys. Rev. Lett.* **95**, 090503 (2005).
- [108] M. B. Plenio, Publisher's Note: Logarithmic Negativity: A Full Entanglement Monotone That Is Not Convex [Phys. Rev. Lett. **95**, 090503 (2005)], *Phys. Rev. Lett.* **95**, 119902(E) (2005).
- [109] H. Bombin and M. A. Martin-Delgado, Topological Quantum Distillation, *Phys. Rev. Lett.* **97**, 180501 (2006).
- [110] H. Bombin and M. A. Martin-Delgado, Topological Computation without Braiding, *Phys. Rev. Lett.* **98**, 160502 (2007).
- [111] P. Schindler, D. Nigg, T. Monz, J. T. Barreiro, E. Martinez, S. X. Wang, S. Quint, M. F. Brandl, V. Nebendahl, C. F. Roos *et al.*, A quantum information processor with trapped ions, *New J. Phys.* **15**, 123012 (2013).
- [112] A. Bermudez, X. Xu, R. Nigmatullin, J. O'Gorman, V. Negnevitsky, P. Schindler, T. Monz, U. G. Poschinger, C. Hempel, J. Home *et al.*, Assessing the Progress of Trapped-Ion Processors Towards Fault-Tolerant Quantum Computation, *Phys. Rev. X* **7**, 041061 (2017).
- [113] M. Englbrecht, T. Kraft, and B. Kraus, Transformations of stabilizer states in quantum networks, *Quantum* **6**, 846 (2022).
- [114] K. Bharti, A. Cervera-Lierta, T. H. Kyaw, T. Haug, S. Alperin-Lea, A. Anand, M. Degroote, H. Heimonen, J. S. Kottmann, T. Menke *et al.*, Noisy intermediate-scale quantum algorithms, *Rev. Mod. Phys.* **94**, 015004 (2022).
- [115] K. Wang, Z. Song, X. Zhao, Z. Wang, and X. Wang, Detecting and quantifying entanglement on near-term quantum devices, *npj Quantum Inf.* **8**, 52 (2022).
- [116] A. Pérez-Salinas, D. García-Martín, C. Bravo-Prieto, and J. I. Latorre, Measuring the tangle of three-qubit states, *Entropy* **22**, 436 (2020).
- [117] R. LaRose, A. Tikku, É. O'Neel-Judy, L. Cincio, and P. J. Coles, Variational quantum state diagonalization, *npj Quantum Inf.* **5**, 57 (2019).
- [118] M. Cerezo, K. Sharma, A. Arrasmith, and P. J. Coles, Variational quantum state eigensolver, *npj Quantum Inf.* **8**, 113 (2022).
- [119] K. E. Hamilton, N. Laanait, A. Francis, S. E. Economou, G. S. Barron, K. Yeter-Aydeniz, T. Morris, H. Cooley, M. Kang, A. F. Kemper, and R. Pooser, An entanglement-based volumetric benchmark for near-term quantum hardware, [arXiv:2209.00678](https://arxiv.org/abs/2209.00678).
- [120] <https://github.com/titaschanda/QIClib>.
- [121] M. Van den Nest, J. Dehaene, and B. De Moor, Efficient algorithm to recognize the local clifford equivalence of graph states, *Phys. Rev. A* **70**, 034302 (2004).
- [122] A. Bouchet, An efficient algorithm to recognize locally equivalent graphs, *Combinatorica* **11**, 315 (1991).
- [123] A. Bouchet, Recognizing locally equivalent graphs, *Discrete Math.* **114**, 75 (1993).
- [124] N. Gisin and H. Bechmann-Pasquinucci, Bell inequality, Bell states and maximally entangled states for n qubits, *Phys. Lett. A* **246**, 1 (1998).
- [125] A. Higuchi and A. Sudbery, How entangled can two couples get? *Phys. Lett. A* **273**, 213 (2000).
- [126] P. Facchi, G. Florio, G. Parisi, and S. Pascazio, Maximally multipartite entangled states, *Phys. Rev. A* **77**, 060304(R) (2008).
- [127] G. Gour and N. R. Wallach, All maximally entangled four-qubit states, *J. Math. Phys.* **51**, 112201 (2010).
- [128] L. Arnaud and N. J. Cerf, Exploring pure quantum states with maximally mixed reductions, *Phys. Rev. A* **87**, 012319 (2013).
- [129] D. Goyeneche, D. Alsina, J. I. Latorre, A. Riera, and K. Życzkowski, Absolutely maximally entangled states, combinatorial designs, and multiunitary matrices, *Phys. Rev. A* **92**, 032316 (2015).
- [130] M. Enríquez, I. Wintrowicz, and K. Życzkowski, Maximally entangled multipartite states: A brief survey, *J. Phys.: Conf. Ser.* **698**, 012003 (2016).
- [131] J. Eisert and H. J. Briegel, Schmidt measure as a tool for quantifying multipartite entanglement, *Phys. Rev. A* **64**, 022306 (2001).
- [132] D. Amaro and M. Müller, Design and experimental performance of local entanglement witness operators, *Phys. Rev. A* **101**, 012317 (2020).
- [133] O. Gühne and M. Seevinck, Separability criteria for genuine multipartite entanglement, *New J. Phys.* **12**, 053002 (2010).